Research supported by the Pan American Climate Studies Program of the NOAA Office of Global Programs under project GC98-627

OBSERVATIONS OF CONVECTIVELY COUPLED KELVIN WAVES

by

Katherine H. Straub

George N. Kiladis, P.I
Wayne H. Schubert, Advisor

Colorado State University

DEPARTMENT OF ATMOSPHERIC SCIENCE

PAPER NO. 725

QC 852
C6
725
ATMOS

OBSERVATIONS OF CONVECTIVELY COUPLED KELVIN WAVES

by

Katherine H. Straub

Department of Atmospheric Science
Colorado State University
Fort Collins, CO 80523-1371

LIBRARIES
JUL 25 2002
COLORADO STATE UNIVERSITY

Summer 2002

Atmospheric Science Paper # 725

U18402 2514009

62 379CSU 3622
XL2
10/02 38-000-01 GBC

ABSTRACT

OBSERVATIONS OF CONVECTIVELY COUPLED KELVIN WAVES

Convectively coupled Kelvin waves are large-scale, eastward-propagating tropical convective disturbances with the dispersion characteristics of equatorially trapped shallow water Kelvin modes. Convection in these waves propagates eastward at 15–20 m s^{-1}, with a horizontal scale of approximately 3000 km, and is accompanied by large-scale dynamical perturbations in the troposphere and lower stratosphere that are broadly consistent with linear equatorial wave theory.

Observations of convectively coupled Kelvin waves are presented based on statistical composites of global reanalysis and radiosonde data and a case study from the 1997 Tropical Eastern Pacific Process Study (TEPPS). These observations address several important issues regarding the horizontal and vertical structure of Kelvin waves, the mechanisms for their initiation, and their modulation by intraseasonal variability.

The TEPPS case study provides detailed information about the small-scale structure observed during the passage of a convectively coupled Kelvin wave in the eastern Pacific intertropical convergence zone (ITCZ). Convection is organized within the eastward-propagating envelope into smaller-scale westward-propagating cloud clusters, in which stratiform precipitation represents a significant fraction of the total

precipitating area. The observed temperature, wind, and moisture fields in the TEPPS case study as well as in statistical composites of radiosonde and global reanalysis data suggest that the stratiform component plays an essential role in the dynamics of convectively coupled Kelvin waves. Several idealized theories of coupled wave instability are compared with these observed structures.

A new mechanism for the initiation of convectively coupled Kelvin waves is presented in this study. During austral winter (boreal summer), a baroclinic Rossby wave packet excited in the Southern Hemisphere subtropical jet is associated with the initiation of a convectively coupled Kelvin wave in the central Pacific ITCZ. These results demonstrate that Kelvin waves can be forced from the extratropics even in regions of tropical easterlies.

Finally, convectively coupled Kelvin wave activity is shown to be modulated by the boreal summer intraseasonal oscillation (ISO). ISO convective anomalies force low-frequency oscillations in the strength, location, and wave activity of the Southern Hemisphere subtropical jet, which modulates tropical Kelvin wave activity through changes in the extratropical forcing of these waves.

Katherine H. Straub
Department of Atmospheric Science
Colorado State University
Fort Collins, CO 80523
Summer 2002

ACKNOWLEDGMENTS

I sincerely thank Dr. George Kiladis for providing the motivation and financial support for this research. I also thank Drs. Wayne Schubert, David Randall, Richard Johnson, and Matthew Wheeler, whose comments and advice have significantly improved this work.

The research presented in this paper relies on data gathered from many sources. The OLR, ECMWF reanalysis, NCEP/NCAR reanalysis, and SST data used throughout Chapters 2–5 were obtained from the NOAA–CIRES Climate Diagnostics Center in Boulder, Colorado. Sandra Yuter at the University of Washington provided the TEPPS radiosonde, surface meteorology, and radar data used in Chapter 2. Christopher Williams at the NOAA Aeronomy Laboratory provided the TEPPS vertical profiler data. The TEPPS rain rate measurements were calculated by Martin Grossklaus and Lutz Hasse of the Institut fuer Meereskunde, Kiel, Germany, and were provided by Sandra Yuter. Wesley Berg at the NOAA Environmental Technology Laboratory in Boulder, Colorado provided the *GOES–9* data for the TEPPS period. The TAO buoy data used in Chapter 2 were downloaded from the Pacific Marine Environmental Laboratory's Tropical Atmosphere Ocean (TAO) Project web page (http://www.pmel.noaa.gov/tao/). Xin Lin at Colorado State University provided the code used to calculate CAPE in Chapters 2 and 4, which is based on code originally written by Kerry Emanuel. The tropical cyclone

track data utilized in Chapter 5 were obtained from Colorado State/Tropical Prediction Center.

This work was financially supported by the Pan American Climate Studies Program of the NOAA Office of Global Programs under project GC98-627.

CONTENTS

1 INTRODUCTION 1

2 OBSERVATIONS OF A CONVECTIVELY COUPLED KELVIN WAVE IN THE EASTERN PACIFIC ITCZ 6

2.1 Introduction 6
2.2 Background 9
2.3 Observations of the TEPPS Kelvin wave 11
2.3.1 Outgoing longwave radiation 12
2.3.2 GOES–9 imagery 16
2.3.3 Radar and vertical profiler 19
2.3.3.1 Radar 19
2.3.3.2 Vertical profiler 23
2.3.3.3 Discussion 27
2.3.4 Surface meteorology 28
2.3.5 Radiosondes and ECMWF reanalysis 33
2.3.5.1 Temperature 34
2.3.5.2 Zonal Wind 38
2.3.5.3 Specific Humidity 42
2.3.5.4 CAPE 45
2.4 Large-scale wave structure 46
2.5 Summary and conclusions 52

3 EXTRATROPICAL FORCING OF CONVECTIVELY COUPLED KELVIN WAVES DURING AUSTRAL WINTER 55

3.1 Introduction 55
3.2 Background 57
3.3 Data and methodology 60
3.4 Climatology 62
3.5 Horizontal structure 65
3.5.1 200 hPa 67
3.5.2 850 hPa 71
3.5.3 1000 hPa 72
3.6 Vertical structure 76
3.7 Longer timescale relationships 80
3.8 Case study: July 1986 vs. July 1987 85
3.9 Summary and conclusions 88

4 THE OBSERVED STRUCTURE OF CONVECTIVELY COUPLED KELVIN WAVES: COMPARISON WITH SIMPLE MODELS OF COUPLED WAVE INSTABILITY 92

4.1 Introduction 92
4.2 Theories of coupled wave instability 95
4.2.1 Wave–CISK 95
4.2.2 WISHE 98
4.2.3 Stratiform instability 100
4.3 Data and methodology 102
4.4 Observed Kelvin wave structure 104
4.4.1 Horizontal structure 105
4.4.2 Vertical structure 108
4.4.3 Phase relationships between temperature and vertical motion 112
4.4.4 Radiosonde comparisons 115
4.4.5 Summary 119
4.5 Discussion and conclusions 120
4.5.1 Comparisons of observations with coupled wave instability theories 120
4.5.1.1 Wave–CISK 120
4.5.1.2 WISHE 123
4.5.1.3 Stratiform instability 125
4.5.2 Conclusions 128

5 INTERACTIONS BETWEEN THE BOREAL SUMMER INTRASEASONAL OSCILLATION AND HIGHER-FREQUENCY TROPICAL WAVE ACTIVITY 131

5.1 Introduction 131
5.2 Data and methodology 133
5.3 Statistical results 136
5.3.1 ISO convection and circulation anomalies 136
5.3.2 Mixed Rossby-gravity waves/TD-type disturbances 139
5.3.3 Kelvin waves 144
5.4 Case study: July–September 1987 150
5.4.1 Westward-propagating modes 151
5.4.2 Eastward-propagating modes 158
5.5 Discussion and conclusions 161

6 CONCLUSIONS 164

REFERENCES 168

FIGURES

Figure 2.1: Wavenumber–frequency power spectrum of the symmetric component of OLR for 1979–99, summed from 15°N to 15°S, and plotted as the ratio of the raw OLR power to the power in a smoothed red noise background spectrum (see WK99 for details). Contour interval is 0.1, from 1.1 to 1.4. Shading begins at 1.1, where the signal is significant at greater than the 95% level. Dispersion curves for the Kelvin, n = 1 equatorial Rossby (ER), and n = 1 westward inertio-gravity (WIG) waves are plotted for equivalent depths of 8, 12, 25, 50, and 90 m. Heavy solid box represents region of Kelvin wave filtering. 10

Figure 2.2: Average variance of Kelvin filtered OLR band during Northern Hemisphere summer (JJA) from 1979–99. Contours from 60–180 W^2 m^{-4} by 60 W^2 m^{-4}. Light (dark) shading represents values greater than 120 (180) W^2 m^{-4}. The location of the *Ronald H. Brown* during TEPPS is indicated by an "x." 14

Figure 2.3: Hovmöller diagram of twice-daily total OLR (shading, scale at bottom) and Kelvin wave filtered OLR (contours at –10 and –30 W m^{-2}), averaged from 2.5°–15°N, from 1 July to 31 August 1997. Solid vertical line represents time and location of TEPPS radiosonde data collection aboard the *Ronald H. Brown*. ... 15

Figure 2.4: *GOES–9* IR images for 14–20 August 1997. Gray scale is at right, in K. The location of the *Ronald H. Brown* is indicated by an "x" in each panel. 17

Figure 2.5: Hovmöller diagram of three-hourly *GOES–9* IR data, averaged from 2° to 12°N, for 13–22 August 1997. Contours from 225 K to 255 K by 10 K. Dark shading denotes temperatures less than 245 K, light shading between 245 and 255 K. Missing data were filled in by a linear interpolation in time if only one or two sequential observations were missing..... 18

Figure 2.6: *GOES-9* IR images (left, in K) and MIT C-band Doppler radar reflectivity maps at 0.5-km elevation (right, in dBZ), for (a), (b) 0000 UTC 18 August; (c), (d) 1300 UTC 18 August; (e), (f) 2200 UTC 18 August; and (g), (h) 2300 UTC 19 August. Radar reflectivity maps are superimposed onto *GOES-9* images; red icons represent locations of TAO buoys. Range rings in reflectivity maps are at 30-km intervals. 20

Figure 2.7: (a) Time–height plot of 2835 MHz vertical profiler reflectivity (dBZ), from 1200 UTC 18 August 1997 to 1200 UTC 20 August 1997, for 500-m pulse mode and 315-m range gate spacing. (b) Rain rate (mm hr^{-1}) for same time period, plotted on a logarithmic scale. Graph courtesy of Christopher Williams, NOAA Aeronomy Laboratory. 25

Figure 2.8: Ratio of radar echo classified as stratiform precipitation (Steiner et al. 1995; Yuter and Houze 1997) to total precipitating echo area in the 83-km range region surrounding the *Ronald H. Brown* for the period from 0000 UTC 18 August 1997 to 0600 UTC 20 August 1997. The three curves represent high (dashed), medium (solid), and low (dotted) estimates based on uncertainty in the radar calibration. Graph courtesy of Sandra Yuter, University of Washington. 26

Figure 2.9: Hourly-averaged surface meteorological data from the *Ronald H. Brown*, for 16–22 August 1997. (a) Shortwave radiation (W m^{-2}), (b) air temperature anomaly (dark line, left scale, K) and SST anomaly (light line, right scale, K), (c) specific humidity anomaly (dark line, left scale, g kg^{-1}) and pressure anomaly (light line, right scale, hPa), (d) total wind direction (dark line, left scale, degrees) and total wind speed (light line, right scale, m s^{-1}). 29

Figure 2.10: (a) TEPPS 4-hourly radiosonde temperature anomalies for 16–21 August 1997, from 1000 to 50 hPa. (b) Regressed daily ECMWF temperatures from day –3 to day +3, based on a –125 W m^{-2} anomaly in OLR at the TEPPS basepoint on day 0. Contour interval in both plots is 0.3 K, with zero contour omitted. Dark shading represents positive anomalies. 35

Figure 2.11: As in Fig. 2.10 except for zonal wind. Contour interval is 1.0 m s^{-1} 39

Figure 2.12: Hourly TAO zonal wind anomalies, averaged from 0°–8°N, for 8–23 August 1997. Values have been smoothed with one pass of a 1-2-1 filter in time. Contour interval is 2 m s^{-1}, starting at ±1 m s^{-1}. Dark shading represents positive anomalies. Dark solid lines represent twice-daily Kelvin wave filtered OLR, averaged from 0°–10°N, contoured at –10 and –30 W m^{-2}. 41

Figure 2.13: Hovmöller diagram of regressed ECMWF daily 1000-hPa zonal wind and OLR from day –11 to day +5, averaged from 0°–10°N, based on a –125 W m^{-2} anomaly in OLR at the TEPPS basepoint on day 0. Contour interval for wind is 1 m s^{-1}, with zero contour omitted. Dark shading represents positive anomalies. Heavy contours represent regressed OLR, contoured from –40 to –80 W m^{-2} in 20 W m^{-2} intervals. 42

Figure 2.14: As in Fig. 2.10 except for specific humidity. Contour interval is 0.3 g kg^{-1}. 43

Figure 2.15: CAPE (J kg^{-1}) at the *Ronald H. Brown* from 16 to 23 August 1997, calculated from 4-hourly radiosonde data. 45

Figure 2.16: Regressed OLR (shading, dark negative, ±10 and 30 W m^{-2}) and 150-hPa temperature (contours, solid positive, contour interval 0.1 K, zero contour omitted) and winds (vectors, maximum 10 m s^{-1}, shown only where 95% significant) for (a) day –3, (b) day 0, and (c) day +3, based on a –50 W m^{-2} OLR anomaly at the TEPPS base point on day 0. 47

Figure 2.17: Longitude–height cross-section of regressed temperature along the equator on day 0 (bottom), and regressed OLR along 7.5°N (top), based on a –50 W m^{-2} OLR anomaly at the TEPPS basepoint on day 0. Contour interval is 0.2 K, with zero contour omitted. Regions of 95% or greater statistical significance are shaded, with dark shading denoting positive correlations. 51

Figure 3.1: Austral winter (JJA) climatological values of total OLR (dark shading), Kelvin wave filtered OLR variance (dark contours), 200-hPa zonal wind (light contours), <30 day filtered 200-hPa meridional wind variance (light shading), and <30 day filtered E-vectors, based on the years 1979–1993. OLR is shaded at 200, 220, and 240 W m^{-2}, and is set to zero outside the range 20°S–30°N for plotting purposes. Kelvin OLR variance is contoured from 120 to 210 W^2 m^{-4} by 30 W^2 m^{-4}. Zonal wind is contoured every 10 m s^{-1}. Meridional wind variance is shaded at 160 and 200 m^2 s^{-2}. Longest E-vectors are 150 m^2 s^{-2}; vectors are not plotted below 10 m^2 s^{-2} 63

Figure 3.2: Regressed values of OLR (shading) and 200-hPa streamfunction (contours) and winds (vectors), based on a –40 W m^{-2} anomaly in Kelvin wave filtered OLR at the basepoint on day 0, for (a) day –9, (b) day –5, (c) day 0, and (d) day +3. OLR is shaded at ±6 and 15 W m^{-2}; dark shading represents negative OLR anomalies. Streamfunction contour interval is 7.5 x 10^5 m^2 s^{-1}; the zero contour has been omitted. The longest wind vectors correspond to a 10 m s^{-1} wind, and are plotted only where either the *u* or *v* component is significant at the 95% level or greater. 66

Figure 3.3: As in Fig. 3.2b except that OLR is represented by hatching (cross-hatching negative, single hatching positive), and shading represents 400-hPa vertical motion (dark positive; shading at 0.2 cm s^{-1}). 68

Figure 3.4: As in Fig. 3.2b except at 850 hPa. Streamfunction contour interval is 4.0 x 10^5 m^2 s^{-1}, and longest vectors correspond to a 5 m s^{-1} wind..... 71

Figure 3.5: As in Fig. 3.3 except at 1000 hPa, for (a) geopotential height and (b) temperature on day –5. Geopotential height contour interval is 5 m from 5 to 20 m, then 40 m; temperature contour interval is 0.05 K from 0.05 to 0.1 K, then 0.2 K. Longest vectors correspond to a 5 m s^{-1} wind. 73

Figure 3.6: Longitude–time diagram of regressed OLR (shading) and 1000-hPa convergence (contours), averaged from 5°S–10°N, from day –11 to day 8. OLR is shaded at intervals of ±5 W m^{-2}, with dark shading representing negative anomalies. Contour interval for 1000-hPa convergence is 2.5 x 10^{-7} s^{-1}, with solid contours representing convergence. The zero contour has been omitted..... 75

Figure 3.7: Longitude–height cross-sections of regressed (a) meridional wind (contours) and vertical motion (shading) along 20°S (lower plot), and OLR along equator (upper plot), (b) temperature (contours), vertical motion (shading), and OLR along equator, and (c) temperature (contours), vertical motion (shading), and OLR along 7.5°N. Contour interval in (a) is 0.5 m s^{-1}, and in (b) and (c) is 0.1 K, and all zero contours have been omitted. Regressed vertical motion is shaded at ±0.1 and ±0.3 cm s^{-1} in (a) and (b), and at +0.1, +0.6, –0.1, and –0.3 cm s^{-1} in (c). Zonal–vertical circulation is shown by vectors, where the vertical component has been multiplied by 700 to account for the small aspect ratio of the plot. The longest vectors represent winds of (a) 5.0 m s^{-1}, (b) 3.5 m s^{-1}, and (c) 9.0 m s^{-1} 77

Figure 3.8: Time series of monthly-averaged Kelvin wave variance (in W^2 m^{-4}) at 7.5°N, 172.5°W from January 1979 to December 2000.....81

Figure 3.9: Monthly averaged Kelvin wave filtered OLR variance (contours), 200-hPa Kelvin filtered meridional wind variance anomalies (shading), and total Kelvin filtered 200-hPa E-vectors for (a) high and (b) low variance composites, based on the 11 months during the JJA season with highest or lowest monthly averaged Kelvin filtered OLR variance in a 5° x 5° box centered at 7.5°N, 172.5°W. Kelvin OLR variance is contoured from 25 W^2 m^{-4} by 50 W^2 m^{-4}. Meridional wind variance is shaded at ±3 and 10 m^2 s^{-2}; dark shading represents positive values. Longest E-vectors are 40 m^2 s^{-2}; vectors are not plotted below 2 m^2 s^{-2}. 82

Figure 3.10: Monthly averaged total SST (hatching and light contours), Kelvin wave filtered OLR variance (dark contours), Kelvin wave filtered 200-hPa meridional wind variance anomalies (shading), total zonal wind (light contours), and Kelvin wave filtered 200-hPa total E-vectors, for (a) July 1986 and (b) July 1987. SST is contoured at 28°, 29°, and 29.5°C, with single hatching at 29°C and cross-hatching at 29.5°C. Kelvin OLR variance is contoured from 150 W^2 m^{-4} by 100 W^2 m^{-4}. Meridional wind variance anomalies are shaded at ±5 m^2 s^{-2}; dark shading denotes positive anomalies. Longest E-vectors are 150 m^2 s^{-2}, and are not plotted below 5 m^2 s^{-2}.....86

Figure 4.1: Schematic longitude–height diagrams illustrating the (a) wave–CISK, (b) WISHE, and (c) stratiform instability mechanisms of coupled wave instability. The wave–CISK and WISHE mechanisms in (a) and (b) are illustrated for a first baroclinic mode Kelvin wave. Vectors represent anomalous winds [except for vectors at right in (b), which represent easterly basic state winds], and cloud illustrations represent populations of cloud systems of the indicated type (convective or stratiform). W (C) represents warm (cold) anomalies. Upward arrows crossing the lower boundary represent surface fluxes.....96

Figure 4.2: Regressed OLR (shading) and ECMWF reanalysis 1000-hPa geopotential height (contours) and winds (vectors) for days (a) –2, (b) 0, and (c) +2, based on a –30 W m^{-2} anomaly in Kelvin wave filtered OLR on day 0 at the base point 7.5°N, 187.5°E. Wind vectors are plotted only where significant at the 95% level or greater. 105

Figure 4.3: Time–longitude diagram of regressed OLR (shading at ±5 W m^{-2} intervals, dark negative) and divergence (contours, solid positive, zero contour omitted) at (a) 1000 hPa (contour interval 0.2 x 10^{-6} s^{-1}), and (b) 150 hPa (contour interval 0.4 x 10^{-6} s^{-1}). All fields have been averaged from 0°–10°N.....107

Figure 4.4: (a) Longitude–height cross-section along 7.5°N of regressed temperature (contours, interval 0.075 K), vertical motion (shading, at 0.15 and 0.5 cm s^{-1}), and zonal–vertical circulation (vectors). OLR cross-section at 7.5°N is shown in upper plot. The vertical component of the vectors has been multiplied by 700 to account for the small aspect ratio of the plot. The longest vectors represent winds of 5.0 m s^{-1}. (b) Same as (a) except for specific humidity (contours, interval 0.05 g kg^{-1}) shown only to 300 hPa.....109

Figure 4.5: Time–longitude diagram of vertical motion (shading, dark negative) and temperature (contours, solid positive, contour interval 0.05 K, zero contour omitted), averaged from 0°–10°N, at (a) 300 hPa, and (b) 700 hPa. Shading in (a) is at ±0.15 cm s^{-1} intervals and in (b) is at ±0.05 cm s^{-1} intervals..... 113

Figure 4.6: Regressed (a) OLR, time–height plots of radiosonde (b) temperature (contour interval 0.1 K), (c) specific humidity (contour interval 0.05 g kg^{-1}; shown only to 300 hPa), and (d) zonal wind (contour interval 0.25 m s^{-1}), and time evolution of (e) CAPE at Majuro (7.1°N, 171.4°E), based on a –30 W m^{-2} anomaly in Kelvin filtered OLR at the closest grid point (7.5°N, 172.5°E) on day 0. Time progresses from right to left, so that time–height structures in (b) and (c) can be compared with longitude–height structures in Figs. 4.4a and 4.4b. Twenty-seven levels of data are represented in (b) and (d), and 15 levels in (c). Shading represents regions of statistical significance at the 95% level or greater, with dark shading representing positive correlations. 116

Figure 4.7: Schematic diagram of observed convectively coupled Kelvin wave structure. W (C) represents warm (cold) anomalies. Width of arrows and size of text denotes relative strength of anomalies. Upward arrows crossing the lower boundary represent surface fluxes. 119

Figure 4.8: Structure of unstable Kelvin wave-CISK mode from Matthews and Lander (1999). Longitude–height cross-sections at 2.8°N of (a) divergence (contour interval is 1 x 10^{-6} s^{-1}) and (b) temperature anomaly (contour interval is 0.2 K). Negative contours are dashed and the zero contour is omitted. 121

Figure 4.9: Structure of stratiform instability mode from Mapes (2000): longitude–height cross-section of regressed temperature (contour interval 0.25 K), based on a +1 standard deviation anomaly in convection at 0° longitude. Zero contour heavy, negative contours dashed. 126

Figure 5.1: Regressed OLR (shading, dark negative, at ±7 W m^{-2}) and 850-hPa streamfunction (light contours, solid positive, by 3 x 10^5 m^2 s^{-1}, zero contour omitted) and wind vectors (plotted only where significant at the 95% level or greater; longest vectors 5 m s^{-1}) on (a) day –15, (b) day –5, (c) day +5, and (d) day +15, based on a –1.5 standard deviation anomaly in the ISO index on day 0. 137

Figure 5.2: Regressed OLR (shading, dark negative, at ±6 and 15 W m^{-2}) and 850-hPa streamfunction (light contours, solid positive, by 2.0 x 10^5 m^2 s^{-1}, zero contour omitted) and wind vectors (plotted only where significant at the 95% level or greater; longest vectors 3 m s^{-1}) on day 0, based on a –20 W m^{-2} anomaly in the MRG/TD OLR index at (a) 5°N, 175°W, and (b) 10°N, 135°W. ... 141

Figure 5.3: Regressed OLR (dark contours at ±7 W m^{-2}, hatching for negative anomalies), 850-hPa zonal wind (light contours, solid positive, by 1 m s^{-1}, zero contour omitted), and MRG/TD filtered OLR variance (shading, dark positive, at ±5 and 15 W^2 m^{-4}) on (a) day –15, (b) day –5, (c) day +5, and (d) day +15, based on the ISO OLR index. 142

Figure 5.4: Regressed OLR (as in Fig. 3), 200-hPa streamfunction (light contours, solid positive, by 1.0 x 10^6 m^2 s^{-1}, zero contour omitted) and wind vectors (plotted only where significant at the 95% level or greater; longest vector 7 m s^{-1}), and Kelvin filtered OLR variance (shading, dark positive, at ±15 and 30 W^2 m^{-4}) on (a) day –15, (b) day –5, (c) day +5, and (d) day +15, based on the ISO OLR index. 146

Figure 5.5: Regressed OLR, 200-hPa streamfunction, and wind vectors as in Fig. 5.4, and <30 day filtered meridional wind variance (shading, dark positive, at ±5 and 15 m^2 s^{-2}), on (a) day –15 and (b) day +5, based on the ISO OLR index. 148

Figure 5.6: Time–longitude plot of total OLR (shading, as indicated), filtered ISO and MRG/TD OLR (contours, solid negative, contour interval 10 W m^{-2}, zero contour omitted), and filtered Kelvin wave OLR (contoured at –12 W m^{-2} only), averaged from 2.5°N–15°N, from 1 July to 15 September 1987. 151

Figure 5.7: Total OLR (shading for values <160, 190, 220, and 240 W m^{-2}), ISO filtered OLR (dark contour at –10 W m^{-2}), 850-hPa 30–96 day filtered zonal wind (light contours, solid positive, by 1 m s^{-1}), and 850-hPa 30–96 day filtered wind vectors (longest vectors 4 m s^{-1}) for (a) 13 August, (b) 18 August, (c) 23 August, (d) 28 August, (e) 2 September, and (f) 7 September 1987. Locations of tropical storms provided by Colorado State University/Tropical Prediction Center. 152

Figure 5.8: Total OLR (shading as in Fig. 7) and <10 day filtered 850-hPa winds (streamfunction contours, interval is 7.5 x 10^5 m^2 s^{-1}; longest wind vectors are 10 m s^{-1}) for 18 August 1987. 154

Figure 5.9: Time–longitude diagram of (a) OLR anomalies (shading, at ±20, 45, and 70 W m^{-2}) and <10 day filtered 850-hPa meridional wind (contours, by 2 m s^{-1}, solid positive, zero contour omitted), for 8–28 August 1987, and (b) regressed OLR (shading, by 5 W m^{-2}) and 850-hPa meridional wind (contours, by 0.25 m s^{-1}) from day –10 to day +10, based on a +20 W m^{-2} anomaly in MRG/TD filtered OLR at 10°N, 95°E on day 0. All fields are averaged from 5°–20°N. 155

Figure 5.10: Averaged ISO filtered OLR (single hatching positive, cross-hatching negative, at ±10 W m^{-2}), Kelvin wave variance (dark contours, from 125 W m^{-2} by 50 W m^{-2}), 30–96 day filtered 200-hPa winds (streamfunction contours, interval 1.0 x 10^6 m^2 s^{-1}; vector winds, longest vectors are 10 m s^{-1}), and <30 day filtered 200-hPa meridional wind variance anomalies (shading, at ±10 and 50 m^2 s^{-2}) for (a) suppressed ISO, 20 July–8 August 1987, and (b) active ISO, 11–30 August 1987. 159

1 INTRODUCTION

This paper consists of four separate manuscripts, presented in Chapters 2–5. Chapter 2 was published in the *Journal of the Atmospheric Sciences* in January 2002, and Chapter 3 was submitted for publication in March 2002.[1] The material in Chapters 4 and 5 is planned for submission in the near future. Each chapter therefore reads as a stand-alone paper, with its own introduction and conclusions. The material in the present chapter provides a short background and introduction to the four papers. A discussion of overall conclusions and additional research suggestions is presented in Chapter 6.

The subject of convectively coupled equatorial waves has gained renewed interest and recognition in the field of tropical meteorology through the recent studies of Takayabu (1994) and Wheeler and Kiladis (1999). These two studies conclusively demonstrate the existence of tropical convective disturbances whose space–time spectral characteristics match the equatorially trapped wave modes predicted by Matsuno (1966), including Kelvin, mixed Rossby-gravity, n = 1 Rossby, and several classes of inertio-gravity waves. Further analysis of these modes by Wheeler et al. (2000) shows that the dynamical structures associated with each of these wave types are broadly consistent with linear equatorial wave theory, thus providing evidence of the convective–dynamical

[1] Therefore, when referenced in Chapters 4 and 5, the material in Chapters 2 and 3 is cited as Straub and Kiladis (2002b) and Straub and Kiladis (2002a), respectively, as indicated in the bibliography.

coupling of these modes. The implied equivalent depths of the coupled modes are much shallower than those associated with dry equatorial waves, however, such that the coupled modes propagate at much slower phase speeds than their dry counterparts. The mechanism for the reduction in phase speed from dry to moist equatorial waves remains one of the fundamental issues yet to be resolved in the field of tropical meteorology.

Observations of convectively coupled equatorial waves are at present limited in scope, and are often based upon global reanalysis and general circulation model data that are highly influenced by convective parameterizations. The present study seeks to provide a detailed set of observations of one particular type of convectively coupled equatorial wave, the Kelvin wave, based on both in situ and model-derived data. These observations will assist future theoretical and modeling efforts by providing information on the convective organization, phase relationships, and forcing mechanisms specific to convectively coupled Kelvin waves.

The four papers presented in Chapters 2–5 address several important issues involving observations of convectively coupled Kelvin waves that have not been investigated in previous studies. These issues are listed below, each followed by a short discussion that includes the motivation for examining the particular topic addressed.

1) How accurate are the horizontal and vertical structures of convectively coupled Kelvin waves as represented in global reanalysis data?

Previous studies such as Takayabu and Murakami (1991) and Wheeler et al. (2000) illustrated the horizontal and vertical structures of convectively coupled Kelvin waves in global reanalysis datasets, as determined through linear regression or composite

analyses based on many years of data. Since model reanalysis data are highly constrained by convective parameterizations in the tropics, where in situ observations are scarce, it is possible that the model-derived fields may not accurately reflect the true wave structures. In order to assess the accuracy of reanalysis-based convectively coupled Kelvin wave structures, high resolution measurements of a single convectively coupled Kelvin wave are presented in Chapter 2, as observed in the eastern Pacific Intertropical Convergence Zone (ITCZ) during the Tropical Eastern Pacific Process Study (TEPPS), which took place during August 1997. These observations not only provide real-time data with which to compare reanalysis-based wave structures, but also represent much higher resolution data than have previously been available. The wide variety of data collected during TEPPS allows a detailed look into numerous small-scale processes operating within the larger-scale Kelvin wave envelope. In addition, radiosonde data from fixed tropical stations are also analyzed in Chapter 4.

2) How are convectively coupled Kelvin waves initiated?

The initiation of convectively coupled Kelvin waves was suggested by Wheeler et al. (2000) to result from the transitioning of a preexisting dry Kelvin wave, propagating eastward at approximately 45 m s^{-1}, into a moist Kelvin wave, which slows to 15 m s^{-1}. Results from coupled wave modeling studies such as Mapes (2000) and Majda and Shefter (2001) suggest that convectively coupled Kelvin waves are inherently unstable modes of the moist atmosphere, and thus may spontaneously self-organize at the correct spatial and temporal scales to promote wave growth. In Chapter 3, a new initiation mechanism for convectively coupled Kelvin waves is presented. Regression analysis

demonstrates that equatorward-propagating extratropical Rossby waves excited in the Southern Hemisphere subtropical jet during austral winter may also force the initiation of convectively coupled Kelvin waves in the central Pacific.

3) What are the phase relationships between temperature and heating in observed convectively coupled Kelvin waves, and do these relationships support previously formulated theories of coupled wave instability?

Atmospheric waves may grow in amplitude if there exists a positive correlation between temperature and heating, through the production of eddy available potential energy (EAPE). Previous theories of coupled wave growth have identified several mechanisms by which this positive correlation between temperature and heating may arise, including wave–CISK (Conditional Instability of the Second Kind), WISHE (Wind-Induced Surface Heat Exchange), and stratiform instability. In Chapter 4, the observed horizontal and vertical structures of convectively coupled Kelvin waves in the central Pacific during boreal summer are examined, based on both reanalysis and radiosonde data. The phase relationships between temperature, vertical motion, and deep convection in observed waves are discussed in the context of the above theories of coupled equatorial wave instability.

4) Is convectively coupled Kelvin wave activity or other short timescale convective activity modulated by the 30–60 day intraseasonal oscillation?

Nakazawa (1988) suggests that 30–60 day intraseasonal oscillations (ISO) are primarily composed of eastward-propagating "super clusters," which are similar if not

identical to convectively coupled Kelvin waves. Hendon and Liebmann (1994), on the other hand, suggest that intraseasonal oscillations consist of an enhancement of westward-propagating, shorter timescale variability. In Chapter 5, the statistical relationships between two types of higher-frequency convectively coupled waves, Kelvin and mixed Rossby-gravity/tropical depression-type (MRG/TD) waves, and the boreal summer ISO are discussed. The results indicate an enhancement of MRG/TD activity within the convectively active ISO envelope, and an enhancement of Kelvin wave activity to the east of the envelope.

The observations of convectively coupled Kelvin waves presented in this study provide a target for future modeling studies of convectively coupled equatorial waves and their interactions with the large-scale environment. The following observational diagnosis of the phase relationships and small-scale structure internal to these waves, as well as their initiation mechanisms and longer timescale modulation, are intended to stimulate future observational and modeling studies by raising additional questions regarding the dynamics of convectively coupled equatorial waves.

2 OBSERVATIONS OF A CONVECTIVELY COUPLED KELVIN WAVE IN THE EASTERN PACIFIC ITCZ

2.1 Introduction

Zonally propagating convective activity represents a significant component of the total variability in the eastern Pacific intertropical convergence zone (ITCZ). Although this region is generally dominated by westward-propagating convective disturbances, observations often reveal the presence of eastward-propagating convective activity, especially during Northern Hemisphere summer and fall. The most frequently observed eastward-propagating disturbances in this region have phase speeds of approximately 17 m s^{-1}, and propagate along the mean convective axis of the ITCZ. The spatial and temporal scales of these disturbances suggest that they can be classified as convectively coupled Kelvin waves (Takayabu 1994; Wheeler and Kiladis 1999, hereafter WK99). In this paper, we present a case study of a particular convectively coupled Kelvin wave in the eastern Pacific ITCZ, and then document the more general statistical structure of convectively coupled Kelvin waves in this region.

Convectively coupled Kelvin waves are eastward-propagating tropical convective disturbances with the dispersion characteristics of equatorially trapped shallow water Kelvin modes (Takayabu 1994; WK99). The convection in these waves is coherently coupled to significant dynamical perturbations in the upper troposphere and lower

stratosphere, which are consistent with linear Kelvin wave theory (Takayabu and Murakami 1991; Wheeler et al. 2000, hereafter WKW00).

Previous studies of convectively coupled Kelvin waves have focused on disturbances in the Indian Ocean and western Pacific regions (Takayabu and Murakami 1991; Dunkerton and Crum 1995; WKW00). In these regions, both the convective and dynamical fields comprising convectively coupled Kelvin waves are fairly symmetric with respect to the equator, as would be expected from linear theory (WKW00). In the eastern Pacific, on the other hand, we will show that the observed eastward-propagating convective signals with Kelvin-like phase speeds and spatial scales exist primarily within the Northern Hemisphere, such that the convection is asymmetric with respect to the equator. Nevertheless, these eastern Pacific disturbances possess similar dynamical structures and dynamical symmetry with respect to the equator as the convectively coupled Kelvin waves in the Indian Ocean and western Pacific, especially in the upper troposphere and lower stratosphere. Since the convection in these eastern Pacific waves exists exclusively to the north of the equator, though, a somewhat different relationship between convection and dynamics is involved.

In order to more completely understand the detailed structure of a convectively coupled Kelvin wave in the eastern Pacific ITCZ, we present a case study of a single Kelvin wave passage based on data collected during the 1997 Pan American Climate Studies (PACS) Tropical Eastern Pacific Process Study (TEPPS; Yuter and Houze 2000). During TEPPS, an eastward-propagating Kelvin wave convective envelope passed directly over the program's observational platform, the National Oceanic and Atmospheric Administration (NOAA) R/V *Ronald H. Brown*, which was stationed in the

eastern Pacific ITCZ at 7.8°N, 125°W. Instrumentation aboard the *Ronald H. Brown* included a C-band Doppler radar, two vertical wind profilers, an upper-air sounding system, an optical disdrometer and rain gauge, and surface meteorological sensors. NOAA polar-orbiting and *GOES–9* geostationary satellites also collected outgoing longwave radiation (OLR) and infrared (IR) measurements over the region. The extensive dataset collected during TEPPS thus provides an unprecedented view of the multiscale convective and dynamical fields comprising a convectively coupled Kelvin wave in the eastern Pacific ITCZ.

Prior to this study, observations of the dynamical fields of convectively coupled Kelvin waves had been based on model analysis or reanalysis data of rather coarse horizontal resolution (Takayabu and Murakami 1991; WKW00). The case study presented here includes data of a much finer temporal and spatial resolution, and is the first analysis based purely on direct field observations. These observations will provide a benchmark for assessing Kelvin wave structures in model datasets, to evaluate the models' utility for further analysis of these waves.

This chapter is organized as follows. Section 2.2 provides a brief background on convectively coupled waves. In Section 2.3, observations of the convectively coupled Kelvin wave observed during TEPPS are presented. The convective and dynamical structure of this wave are analyzed using observations of global OLR, *GOES–9* IR data, and the radar, profiler, rain rate, surface meteorology, and radiosonde data collected aboard the *Ronald H. Brown* during TEPPS. The radiosonde data are compared with the time–height structure of a "composite" Kelvin wave disturbance calculated from European Centre for Medium-Range Weather Forecasts (ECMWF) reanalysis data.

These composite results are then extended in Section 2.4 to include all global reanalysis grid points, and the temporal and spatial evolution of a three-dimensional composite Kelvin wave disturbance in the eastern Pacific is discussed. Finally, a summary and conclusions are presented in Section 2.5.

2.2 Background

The existence of convectively coupled equatorial waves has been known for some time (e.g., Sikdar et al. 1972; Gruber 1974; Zangvil 1975; Zangvil and Yanai 1980, 1981; Takayabu 1994; WK99). Kelvin and mixed Rossby-gravity waves are the most well-documented of all the wave types affecting the equatorial region (Nakazawa 1988; Hayashi and Nakazawa 1989; Liebmann and Hendon 1990; Hendon and Liebmann 1991; Lau et al. 1991; Takayabu and Murakami 1991; Dunkerton and Baldwin 1995; Dunkerton and Crum 1995; WKW00). Inertio-gravity and equatorial Rossby waves have also been studied (Kiladis and Wheeler 1995; Takayabu et al. 1996; Haertel and Johnson 1998; WKW00).

Convectively coupled equatorial waves can be identified in a power spectrum of many years of tropical cloudiness data (Takayabu 1994; WK99). Presented in Fig. 2.1 is an updated version of the symmetric outgoing longwave radiation (OLR) power spectrum shown in WK99 (see their Fig. 3b), for the years 1979–99. A smoothed red background spectrum has been removed from the raw power spectrum such that the contours in Fig. 2.1 represent statistically significant spectral peaks at greater than the 95% level (see WK99 for more details). These peaks fall along the dispersion curves for several of the equatorially trapped shallow water waves discussed by Matsuno (1966), including

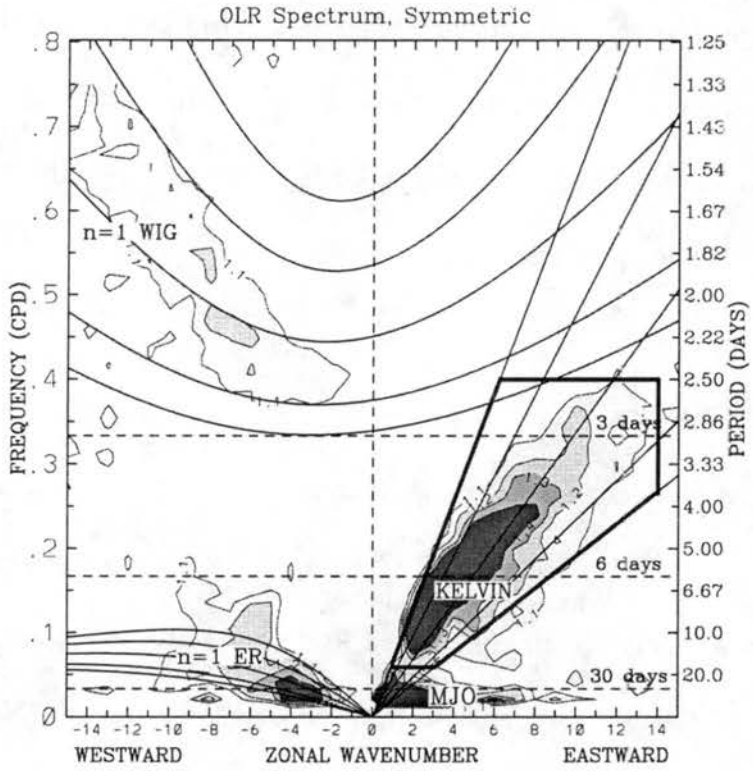


Figure 2.1: Wavenumber–frequency power spectrum of the symmetric component of OLR for 1979–99, summed from 15°N to 15°S, and plotted as the ratio of the raw OLR power to the power in a smoothed red noise background spectrum (see WK99 for details). Contour interval is 0.1, from 1.1 to 1.4. Shading begins at 1.1, where the signal is significant at greater than the 95% level. Dispersion curves for the Kelvin, n = 1 equatorial Rossby (ER), and n = 1 westward inertio-gravity (WIG) waves are plotted for equivalent depths of 8, 12, 25, 50, and 90 m. Heavy solid box represents region of Kelvin wave filtering.

Kelvin, equatorial Rossby, mixed Rossby-gravity, and inertio-gravity waves. The implied equivalent depth of these waves is within the range of 10–100 m. Note the Kelvin wave spectral peak in the OLR spectrum, and the spectral gap separating it from the Madden-Julian Oscillation (MJO) spectral peak directly beneath it (wavenumbers 0–5, period 30–70 days). This spectral gap suggests that Kelvin waves can be considered to be distinguishable from the MJO.

WKW00 calculated the composite dynamical structures corresponding to each of these OLR modes, based on reanalysis data, and found remarkable similarities to the theoretical shallow water wave structures predicted by Matsuno (1966) and linear Kelvin wave theory (including vertical structure; e.g., Andrews et al. 1987), particularly in the upper troposphere and lower stratosphere, above the heating associated with deep convection. The coherence between convection and circulation in these equatorial waves, together with their resemblance to the linear shallow water modes, suggests a coupling between deep convection and the linear, dry (or "free") dynamical modes of the shallow water system. The shallow equivalent depths implied by the OLR power spectrum in Fig. 2.1 suggest an interplay between tropical convection and dynamics which may be responsible for slowing the phase speed of these waves from that of their dry counterparts (WKW00).

2.3 Observations of the TEPPS Kelvin wave

The majority of this study is devoted to observations of the convectively coupled Kelvin wave that propagated across the eastern Pacific ITCZ during TEPPS. Our analysis begins with observations of the cloudiness field associated with this eastward-propagating wave. In Section 2.3.1, a spectral decomposition of global OLR data demonstrates that this particular disturbance is in fact consistent with a convectively coupled Kelvin wave, as defined by the methodology developed in WK99 and WKW00. In Section 2.3.2, the spatial and temporal evolution of the small-scale cloud structures during this Kelvin wave event are analyzed using *GOES–9* IR data. The radar and vertical profiler data collected aboard the *Ronald H. Brown* during TEPPS are presented

in Section 2.3.3. The surface meteorology data are then used in Section 2.3.4 to assess the local effects of convection on the boundary layer, and also to determine any lower-frequency variability that may be associated with the large-scale wave structure. Finally, in Section 2.3.5, the vertical structure of the dynamical and moisture fields associated with the TEPPS Kelvin wave are illustrated using radiosonde data from the *Ronald H. Brown*. These fields help to confirm that the wave observed during TEPPS is in fact a convectively coupled Kelvin wave.

2.3.1 Outgoing longwave radiation

OLR has been used successfully in many previous studies to identify large-scale convective disturbances with timescales of several days or longer (e.g., Kiladis and Weickmann 1992a, 1997; WK99). In this section, the OLR signature of the eastward-propagating wave observed during TEPPS will be shown to fall into the space-time region of the convectively coupled Kelvin waves (hereafter referred to as simply "Kelvin waves") pictured in Fig. 2.1. Kelvin waves are identified using a filtered version of the interpolated, 2.5° gridded, global NOAA polar-orbiting satellite OLR dataset described by Liebmann and Smith (1996).

The technique used to isolate the OLR variability associated with Kelvin waves is fully detailed in WK99. In summary, the OLR data are filtered in wavenumber–frequency space such that only the variability on space and time scales represented by the Kelvin wave "box" shown in Fig. 2.1 is retained. The resultant filtered OLR dataset is then used to identify specific Kelvin wave episodes in the raw OLR data. In this study, the Kelvin wave box drawn in WK99 is slightly modified by

shifting the lower boundary upward in frequency from 1/30 cycles per day (cpd) to 1/17 cpd, as reflected in Fig. 2.1. This change provides a more distinct separation between Kelvin waves and the MJO, and is based on the pronounced spectral gap at a period of 17 days. It does not affect the phase speed of the filtered waves.

In WK99 and WKW00, this filtering was performed only on the symmetric component of the OLR field, since Kelvin waves are defined in the symmetric portion of the OLR power spectrum. In this study, however, we take a slightly different approach and instead filter the data without first separating into symmetric and antisymmetric components. The motivation for this change is as follows. In the eastern Pacific, where this study is focused, convective disturbances tend to propagate along the latitude of the ITCZ, which for the majority of the year lies between approximately 5°N and 15°N. Fast eastward-propagating convective signals with similar spatial scales and phase speeds to WK99's symmetric Kelvin waves are often observed within this latitude band. These disturbances, with significant amplitudes present only in the Northern Hemisphere, will project onto both the symmetric and antisymmetric components of the OLR field. Thus the total OLR field is necessary to resolve these disturbances accurately. Correlation coefficients between the Kelvin wave filtered OLR and the total OLR are higher in the eastern Pacific with this filtering method than when only the symmetric data are used (not shown).

The average variance of the Kelvin wave filtered OLR for Northern Hemisphere summer (JJA) from 1979–99 is shown in Fig. 2.2. The maximum variance tends to follow the latitude of the climatological ITCZ, with an equatorial maximum in the Indian Ocean region, and a maximum significantly to the north of the equator in the central and

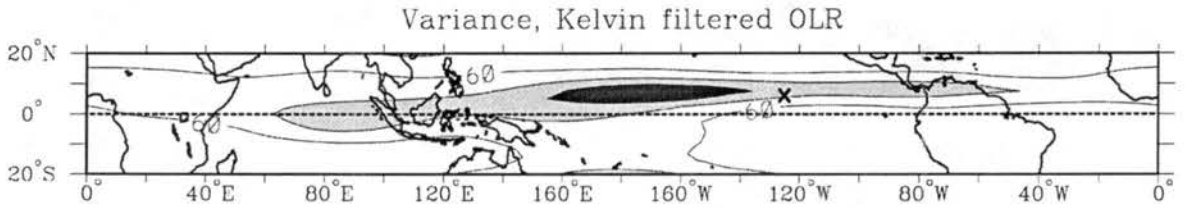


Figure 2.2: Average variance of Kelvin filtered OLR band during Northern Hemisphere summer (JJA) from 1979–99. Contours from 60–180 W^2 m^{-4} by 60 W^2 m^{-4}. Light (dark) shading represents values greater than 120 (180) W^2 m^{-4}. The location of the *Ronald H. Brown* during TEPPS is indicated by an "x."

eastern Pacific and Atlantic regions. Fig. 2.2 also illustrates the concentration of high Kelvin wave variance to the north of the equator in the central Pacific during JJA, with a maximum near 7.5°N, 180°.

The behavior of the tropical OLR field is now examined for the period encompassing the TEPPS cruise, during July and August 1997. Fig. 2.3 is a Hovmöller diagram of the twice-daily total OLR (shading) and the Kelvin wave filtered OLR (contours, only negative values shown, representing enhanced deep convection in the Kelvin filtered band), averaged between 2.5°N and 15°N, from 1 July to 31 August 1997. A number of strong eastward-propagating disturbances are visible in the eastern Pacific during this time period, the most noteworthy crossing 120°W on 13 July, 25 July, and 20 August. The Kelvin wave filtered OLR captures the timing and phase speed of these disturbances remarkably well.

The solid vertical line in Fig. 2.3 represents the time and location of TEPPS data collection while the *Ronald H. Brown* remained stationary in the ITCZ at 7.8°N, 125°W, from 8 to 23 August 1997. The location of the *Ronald H. Brown* is also marked on the Kelvin wave variance map in Fig. 2.2. Based on the Kelvin wave filtered OLR in Fig. 2.3, it can be seen that the eastward-propagating disturbance which passed over the ship

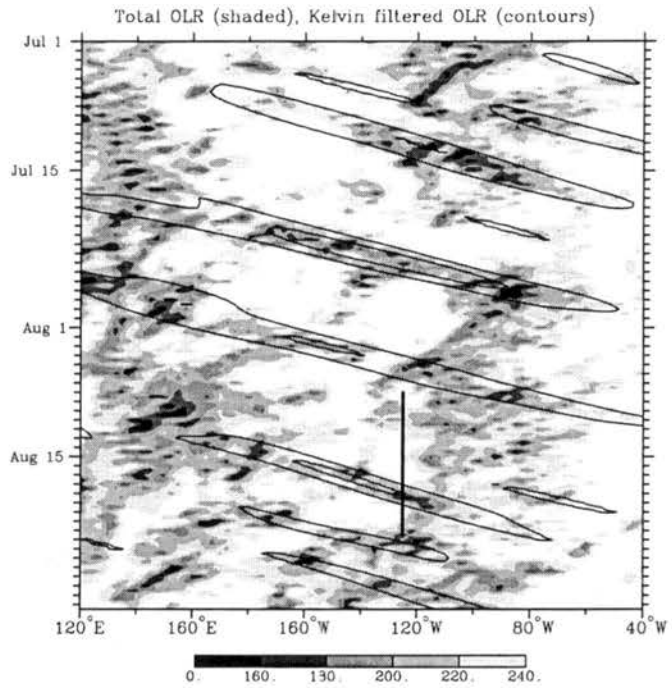


Figure 2.3: Hovmöller diagram of twice-daily total OLR (shading, scale at bottom) and Kelvin wave filtered OLR (contours at –10 and –30 W m^{-2}), averaged from 2.5°–15°N, from 1 July to 31 August 1997. Solid vertical line represents time and location of TEPPS radiosonde data collection aboard the *Ronald H. Brown.*

during this period was in fact a convectively coupled Kelvin wave. The dynamical fields, to be shown in Section 2.3.5, confirm this. This disturbance is traceable in the OLR field from 160°E to 100°W, over a period of 9 days, giving an average phase speed of about 15 m s^{-1}. While the total OLR field suggests that the deepest convection associated with the Kelvin wave occurred as it passed over the *Ronald H. Brown*, the Kelvin wave filtered OLR shows that this component actually peaked to the west of the ship. The minimum OLR over the *Ronald H. Brown* on 18–19 August reflects both Kelvin wave variability and OLR variability unrelated to the Kelvin wave disturbance.

2.3.2 GOES–9 imagery

GOES–9 infrared (IR, 10.7μm) data provide a much higher resolution (3 hourly, 0.1°) view of the cloudiness field associated with the Kelvin wave during TEPPS. An overview of the eastward propagation of the convective disturbance is presented in Fig. 2.4. Six IR images are shown, spanning a roughly 5-day period from 1500 UTC 14 August to 0000 UTC 20 August. The location of the *Ronald H. Brown* is indicated by an "x" in each image.

On 14 August, the deepest convection is located at the western edge of the domain, centered at approximately 10°N, 180°. By 15 August, this convective envelope has shifted eastward and southward to approximately 5°N, 160°W. At this stage, the overall envelope measures roughly 20° in longitude by 10° in latitude, or approximately 2000 km by 1000 km. The envelope continues to shift eastward over the next 4 days, passing almost directly over the ship on 18 August, and is centered around 10°N, 120°W on 20 August. The average phase speed over the period is approximately 15 m s^{-1}, which agrees with the speed determined from the more coarsely gridded OLR data in the previous section.

Within the larger eastward-propagating envelope of convection in Fig. 2.4, many smaller-scale features are evident. Although the large-scale cloudiness field appears to propagate to the east, higher temporal resolution images show distinct convective elements, with spatial scales on the order of 100–500 km, moving westward within this envelope. To illustrate the westward movement of these smaller-scale features, Fig. 2.5 is a Hovmöller diagram of the 3-hourly *GOES–9* data, averaged from 2°–12°N, from 13–22 August. Many westward-moving features are apparent within the eastward-

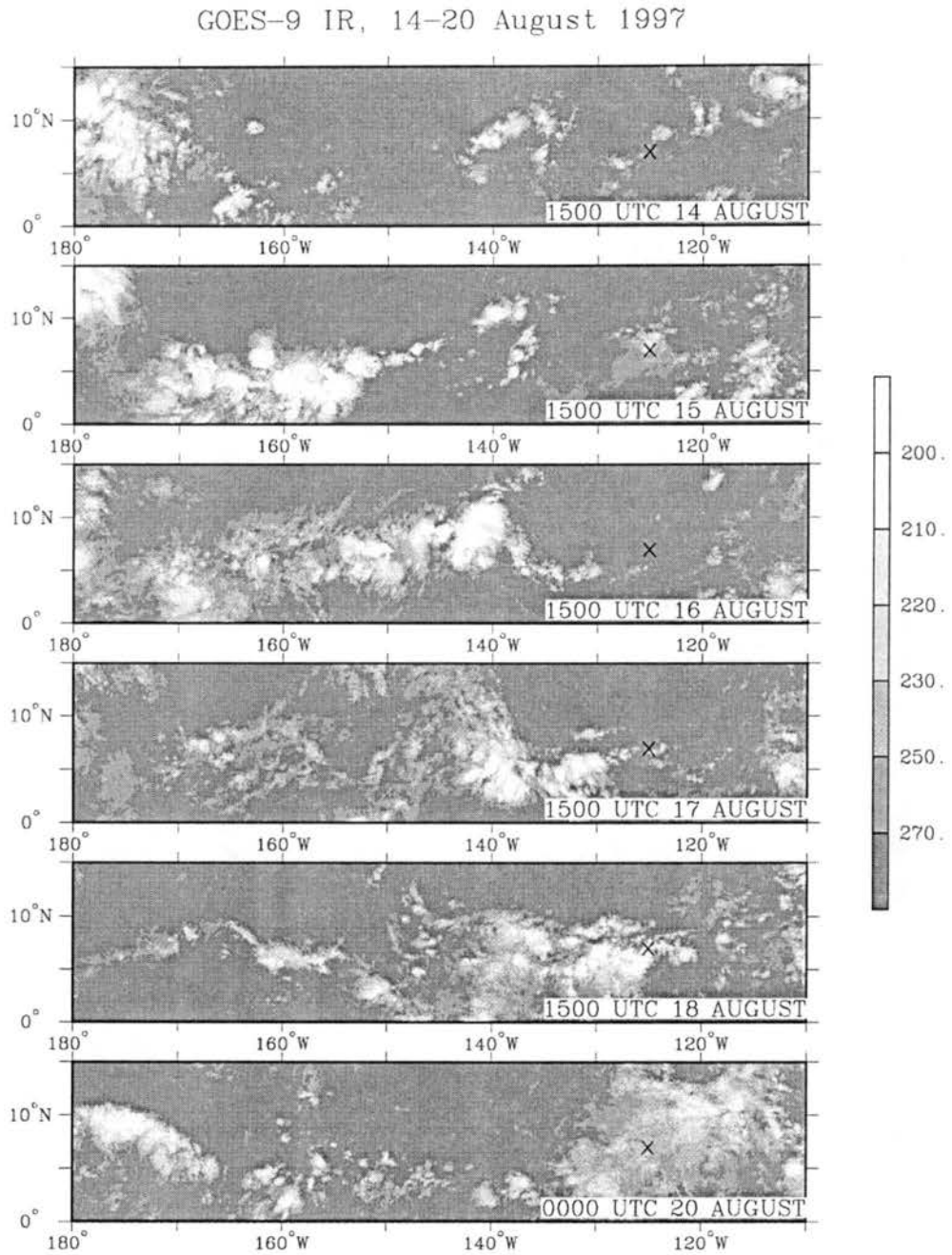


Figure 2.4: *GOES–9* IR images for 14–20 August 1997. Gray scale is at right, in K. The location of the *Ronald H. Brown* is indicated by an "x" in each panel.

propagating envelope of convection, most notably on 16–17 August near 140°W and on 20 August near 120°W. Of course, since this convective signal is averaged over a 10° latitude band, it illustrates only the largest and most intense of the westward-moving features, which appear to have widely varying westward phase speeds. Additional

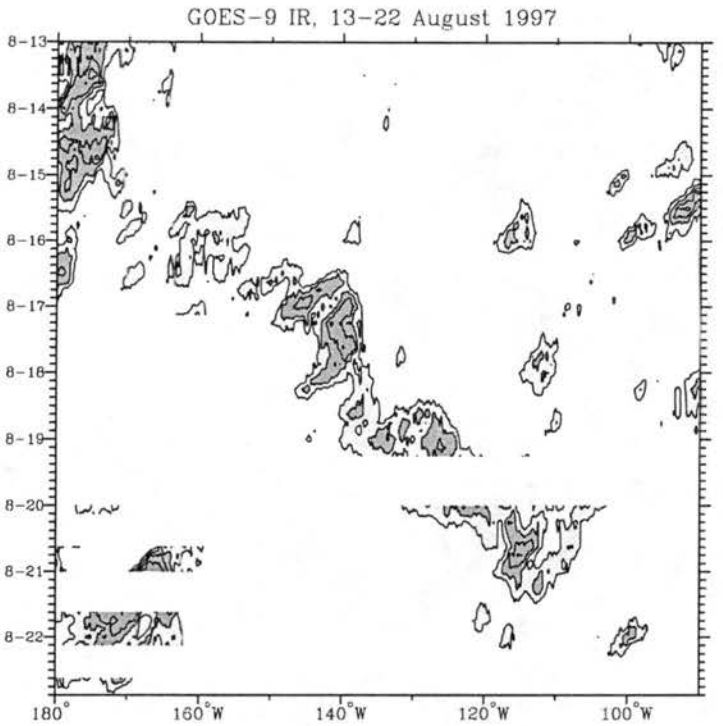


Figure 2.5: Hovmöller diagram of three-hourly *GOES–9* IR data, averaged from 2° to 12°N, for 13–22 August 1997. Contours from 225 K to 255 K by 10 K. Dark shading denotes temperatures less than 245 K, light shading between 245 and 255 K. Missing data were filled in by a linear interpolation in time if only one or two sequential observations were missing.

evidence of the westward movement of the smaller-scale embedded features is apparent in the 3-hourly maps of the *GOES–9* data (not shown) as well as the radar data discussed in the next section. The hierarchical structure of convection shown here for the TEPPS Kelvin wave is also observed within other eastern Pacific Kelvin waves we have examined.

Nakazawa (1988) first detailed this hierarchy of convection in eastward-propagating "super clusters" within the MJO in the western Pacific, using OLR and GMS infrared data. Super clusters propagate eastward at 10–15 m s^{-1}, and consist of smaller-scale "cloud clusters" which move westward within the envelope, in a similar manner to the observations presented in Fig. 2.5. In fact, the specific examples of super clusters

illustrated in Nakazawa (1988) are identified in our Kelvin wave filtered OLR dataset as clear examples of convectively coupled Kelvin waves (not shown). Thus it is suggested in both Nakazawa (1988) and the present study that an eastward-propagating convectively coupled Kelvin wave envelope consists primarily of smaller-scale, westward-moving convective features.

2.3.3 Radar and vertical profiler

To further examine the small-scale structure of convection in the eastward-propagating Kelvin wave convective envelope during TEPPS, data are presented from the C-band Doppler radar and the 2835 MHz vertical profiler located aboard the *Ronald H. Brown*. These measurements provide a more complete picture of local convection in the vicinity of the ship during the Kelvin wave passage.

2.3.3.1 Radar

The Massachusetts Institute of Technology (MIT) C-band Doppler radar collected three-dimensional reflectivity and velocity measurements every 15 minutes while the ship was on station in the eastern Pacific ITCZ. Maps of reflectivity at 0.5-km altitude will be analyzed in this section. To provide a broader context for these data, simultaneous *GOES–9* IR images will also be presented.

At 0000 UTC on 18 August (1700 LST), the Kelvin wave convective envelope is centered about 1000 km to the southwest of the ship, at approximately 3°N, 132°W (Fig. 2.6a). Convection in the vicinity of the ship, as observed by radar, is widely scattered, fairly small scale, and generally shallow, with most cells on the order of 5–10 km across

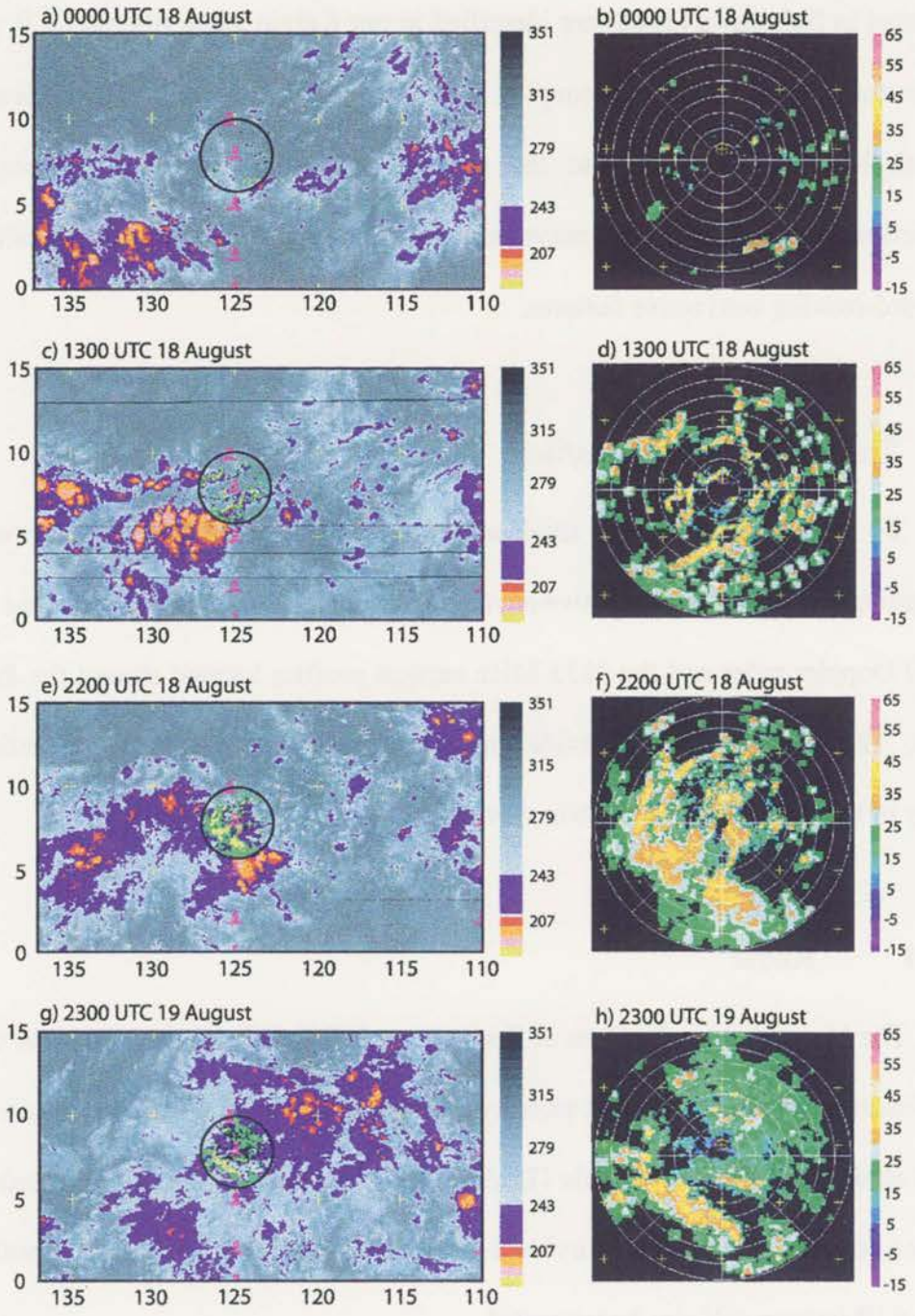


Figure 2.6: *GOES-9* IR images (left, in K) and MIT C-band Doppler radar reflectivity maps at 0.5-km elevation (right, in dBZ), for (a), (b) 0000 UTC 18 August; (c), (d) 1300 UTC 18 August; (e), (f) 2200 UTC 18 August; and (g), (h) 2300 UTC 19 August. Radar reflectivity maps are superimposed onto *GOES-9* images; red icons represent locations of TAO buoys. Range rings in reflectivity maps are at 30-km intervals.

(Fig. 2.6b). The low clouds in the area are noted in the ship's cloud log as cumulus mediocris and humilis, with altocumulus the predominant cloud type at midlevels. These small convective cells generally move to the northwest, consistent with the mean flow in the lowest 3 km (3.9 m s^{-1} from 112°, as calculated from radiosonde data), similar to observations by Wu and LeMone (1999) during TOGA COARE easterly wind periods. This relatively "suppressed" convective environment had been in place for at least the past 48 hours. We note, however, that this suppressed environment does not preclude the development of isolated deep convective events, as can be inferred from occasional 40+ dBZ radar reflectivities and a waterspout sighting noted in the cloud log at 1900 UTC 17 August.

By 1300 UTC (0600 LST) 18 August, convection around the ship has increased in areal coverage and in intensity, as well as in its scale of organization (Fig. 2.6d). This general intensification of convection is associated with the eastward propagation of the large-scale Kelvin wave convective envelope toward the ship, as is evidenced by the eastward shift of the coldest cloud tops to 125°–130°W (Fig. 2.6c). Several linear features are apparent in the radar data, oriented from southwest to northeast and on the order of 50–100 km in horizontal extent, with maximum reflectivities at the 0.5 km level of 45 dBZ. These features generally move to the northwest, and have lifetimes on the order of several hours. Cloud observations at the ship over the time period from 0000 UTC to 1300 UTC confirm the deepening of convection from cumulus to cumulonimbus. Lightning to the northwest of the ship is noted at 1100 UTC, suggesting that convection is deep and vigorous enough at this time to electrify through ice-phase processes (e.g.,

Williams 1988; Houze 1993). Observations of lightning are rare in the tropical eastern Pacific (Zipser 1994).

By 2200 UTC 18 August (1500 LST), the coldest cloud tops in the large-scale region are located to the southeast of the ship (Fig. 2.6e), with deep convection extending in a northwesterly direction into the southwestern quadrant of the radar coverage (Fig. 2.6f). These cells are organized on an even larger scale than at 1300 UTC, extending over 100 km in the horizontal. Less linear organization is apparent than at 1300 UTC, with larger regions of stratiform precipitation surrounding the expanding convective cores. These systems move westward and southward. The predominant cloud types observed at the ship during this period are towering cumulus and altocumulus. Rain begins to fall at the ship at 1800 UTC, and lasts until 0200 UTC 19 August, as is discussed further in the following section.

The large-scale convective envelope continues to shift eastward over the next 24 hours. At 2300 UTC on 19 August (1600 LST), the coldest cloud tops are located to the northeast of the ship, centered at approximately 10°N, 120°W (Fig. 2.6g). The ship is located at the western edge of the Kelvin wave envelope. A large percentage of the radar domain is now covered by lower reflectivities, signifying stratiform rainfall (Fig. 2.6h), with smaller embedded deep convective cores. To the southwest is a vigorous convective line, oriented from northwest to southeast and moving slowly to the northeast. The change in orientation and direction of motion of this line from that observed on 18 August may be related to the observed shift in the low-level wind direction, from southeasterly to southwesterly. As will be discussed further in Section 2.3.4, the low-level wind field of a theoretical Kelvin wave is expected to shift from easterly to westerly

at a fixed point as enhanced convergence (and in the moist case, precipitation) propagates past.

Convection in the vicinity of the ship dissipates as rapidly as it initially grew, declining from widespread stratiform precipitation to very few scattered radar echoes within just 2–3 hours on 20 August. The speed at which convection intensifies and dissipates suggests the presence of strong large-scale forcing in the vertical motion and/or stability fields, which effectively turns deep convection on and off.

In summary, the radar data collected aboard the *Ronald H. Brown* suggest a rapid buildup of convection as the Kelvin wave convective envelope approaches from the west. Initially, convection consists of small, isolated cells that move to the northwest, in the direction of the mean low-level wind. Linear features build from these small cells, and convective elements in general become more interconnected. Large stratiform regions then develop, while deep convection continues to consolidate into larger systems. As the large-scale envelope moves to the east, stratiform features become progressively more predominant, and finally, all convection rapidly dissipates within just a few hours. The total duration of convection observed at the *Ronald H. Brown* during this Kelvin wave event is approximately 48 hours.

2.3.3.2 Vertical profiler

Two NOAA Aeronomy Laboratory vertical profilers (915 and 2835 MHz) collected data on the vertical structure of convection directly above the *Ronald H. Brown.* The 2835 MHz (or "S-band") data are analyzed here, because of this instrument's higher sensitivity to rain compared to the 915-MHz profiler. However, the qualitative aspects of

the data from the two profilers are very similar. The data have a temporal resolution of approximately 1 minute.

Measurements of rain rate taken at the ship are presented with the profiler data. Rain rates were calculated based on measurements from the Institut fuer Meereskunde (IfM) optical disdrometer located aboard the *Ronald H. Brown.* Measurements were also generally taken every minute.

Figures 2.7a and 2.7b show the S-band profiler data and the IfM rain rate data for the 48-hour period from 1200 UTC 18 August to 1200 UTC 20 August, which covers the period of significant rainfall at the ship associated with the Kelvin wave passage. In general, the timing of the reflectivity signal in the profiler data and the rain rate signal match very well.

As was shown in the radar data in Fig. 2.6, convection in the vicinity of the *Ronald H. Brown* builds rapidly on 18 August. The first rain signal at the ship associated with the Kelvin wave passage occurs as convection is just beginning to intensify, at 0500 UTC on 18 August, and is associated with a very isolated, shallow convective event (not shown). By 1500 UTC, convection near the *Ronald H. Brown* has intensified substantially, and the first deep convective signal is observed by the profiler, with echo top heights reaching at least 13 km. The most intense rainfall event of the 3-day period from 18 to 20 August then begins at 1800 UTC 18 August. This event is primarily convective in nature, with little evidence of a stratiform bright band. Rain rates reach a maximum of 35 mm hr^{-1} at 1818 UTC. The cumulative rainfall total for the 12-hour period from 1500 UTC on 18 August to 0300 UTC on 19 August is 23.77 mm.

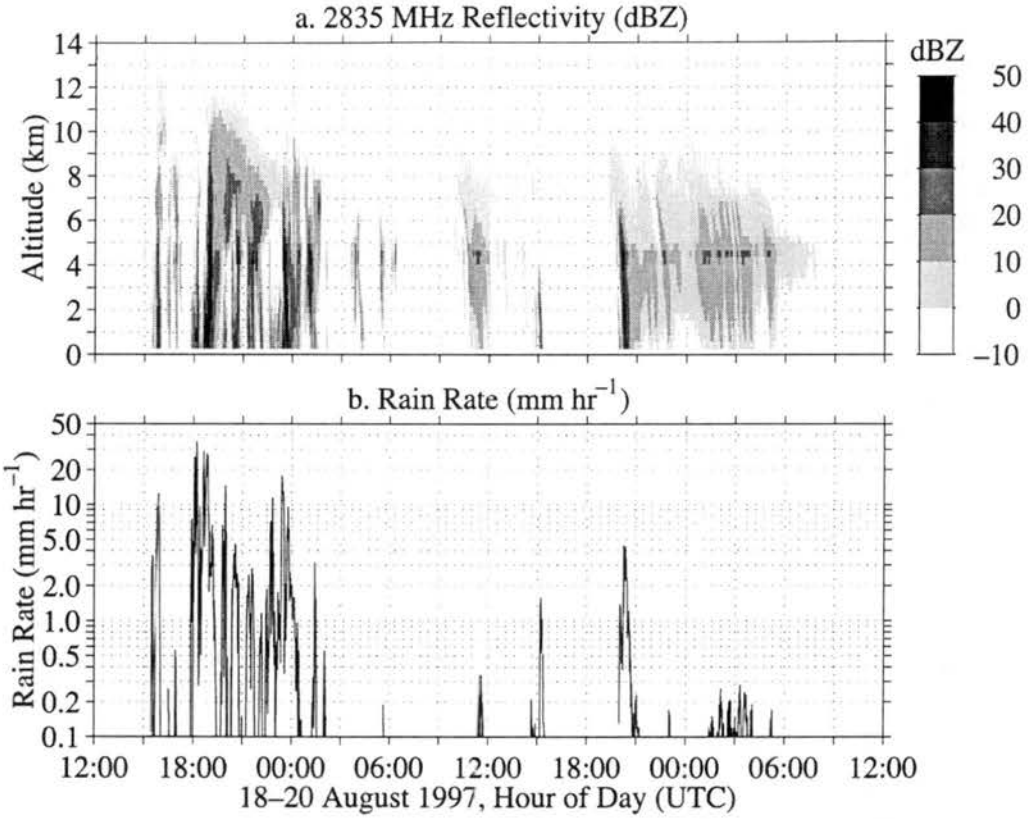


Figure 2.7: (a) Time–height plot of 2835 MHz vertical profiler reflectivity (dBZ), from 1200 UTC 18 August 1997 to 1200 UTC 20 August 1997, for 500-m pulse mode and 315-m range gate spacing. (b) Rain rate (mm hr^{-1}) for same time period, plotted on a logarithmic scale. Graph courtesy of Christopher Williams, NOAA Aeronomy Laboratory.

After this initial convective event, the remainder of the rainfall signal at the ship appears to be primarily stratiform in nature, as identified by the prominent bright band in the reflectivity data at 4.5 km. Rain rates during this stratiform precipitation are very light, generally less than 0.2 mm hr^{-1}, and the total accumulation at the ship is 0.44 mm. The initial deep convective precipitation event thus accounts for the majority of the rainfall measured at the *Ronald H. Brown* (92% of the total) during the Kelvin wave passage.

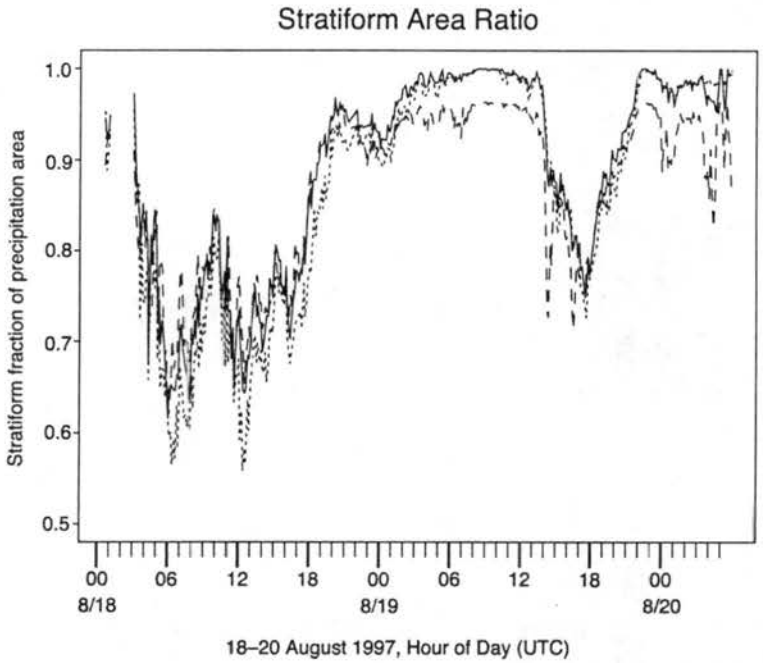


Figure 2.8: Ratio of radar echo classified as stratiform precipitation (Steiner et al. 1995; Yuter and Houze 1997) to total precipitating echo area in the 83-km range region surrounding the *Ronald H. Brown* for the period from 0000 UTC 18 August 1997 to 0600 UTC 20 August 1997. The three curves represent high (dashed), medium (solid), and low (dotted) estimates based on uncertainty in the radar calibration. Graph courtesy of Sandra Yuter, University of Washington.

The disdrometer rainfall data collected aboard the *Ronald H. Brown*, however, represent only one point measurement of rainfall, and thus may not accurately portray the large-scale environment surrounding the ship. Presented in Fig. 2.8 is a time series of the stratiform fraction of the total precipitation area as observed by the C-band Doppler radar, from 0000 UTC 18 August to 0600 UTC 20 August. [For details on the analysis procedure, see Steiner et al. (1995) and Yuter and Houze (1997).] As convection initially intensifies on 18 August (see Fig. 2.6), the stratiform area fraction decreases rapidly, corresponding to an increase in deep convective rainfall. The total area covered by precipitating echo also increases during this period (not shown), again suggesting the rapid growth of deep convection in the vicinity of the ship. As the cloud systems

organize onto larger scales, during the latter half of 18 August and into 19 August, the stratiform fraction steadily increases, reaching a value of 1.0 at approximately 0800 UTC 19 August. The stratiform fraction then decreases again between approximately 1300 UTC and 2100 UTC 19 August, corresponding to the deep convective signal observed by the vertical profiler at the ship at 2000 UTC 19 August (Fig. 2.7). Finally, as the Kelvin wave envelope departs to the east on 20 August, the stratiform fraction increases once again to values approaching 1.0. Interestingly, during the entire TEPPS ITCZ cruise (8–23 August 1997), the stratiform fractional area remains higher than 0.5 at all times (not shown). This suggests that stratiform rainfall is predominant during active periods in the eastern Pacific ITCZ region.

In summary, during the Kelvin wave passage, the stratiform fractional area initially decreases rapidly, then generally increases as a function of time, punctuated by several distinct periods of more active deep convection. Based on both the vertical profiler data and the stratiform area fraction data, it appears that the highest rainfall rates and the largest deep convective fraction occur in the initial stages of this Kelvin wave passage. As the envelope propagates eastward across the observational domain, the stratiform area fraction increases, associated with smaller rain rates over a proportionally larger area.

2.3.3.3 Discussion

The radar and profiler data imply a clear sequence of events at a fixed point as the Kelvin wave convective envelope passes by. As the large-scale envelope approaches the ship from the west, the rainfall has a substantial convective component, with echo top

heights generally above 10 km. These convective cells increase in intensity, size, and organization with time as the large-scale envelope approaches, beginning with small-scale, unorganized cells and progressing to larger-scale, more intense features. These features generally move with the mean low-level wind. As the convective envelope propagates to the east of the ship, the convective portion of the rainfall gradually decreases and the stratiform component increases. The cloud systems that produce the stratiform rainfall tend to be large in horizontal extent, covering a larger portion of the total domain, and the rainfall at a single point lasts for a significant time period. While the interpretation of the disdrometer rainfall data might suggest that the total rainfall accumulation during the Kelvin wave passage is dominated by its deep convective component, the area-averaged radar data in Fig. 2.8 show that it is instead dominated by the stratiform component.

These measurements suggest that the Kelvin wave envelope consists of deeper convection on its eastern side, and predominantly stratiform precipitation to the west. This is consistent with observations of large-scale features within the envelope moving westward with time, as shown in Fig. 2.5. New convection appears to be initiated to the east of the existing envelope, and is organized into deep, intense convective cells. These cells then mature into stratiform-dominated systems as they move westward.

2.3.4 Surface meteorology

Surface meteorology and sea surface temperature (SST) measurements were continuously recorded aboard the *Ronald H. Brown* during the Kelvin wave passage. Presented in Fig. 2.9 are time series of total shortwave radiation; anomalous temperature,

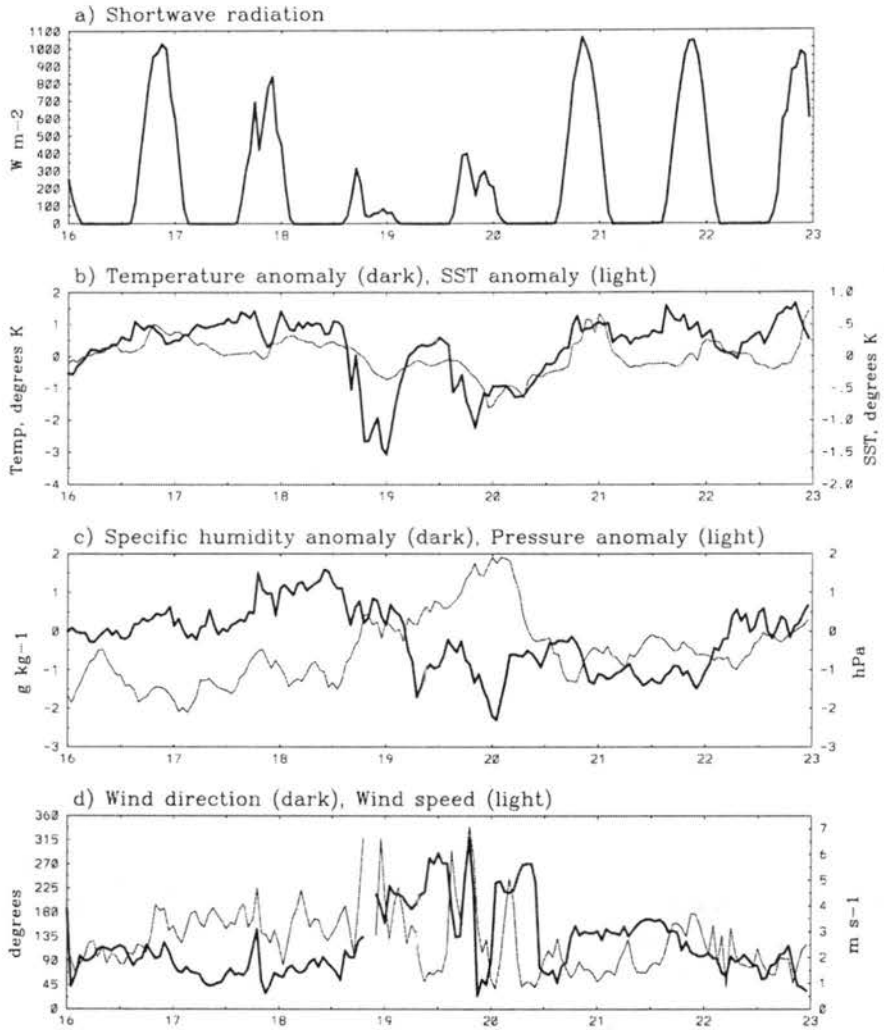


Figure 2.9: Hourly-averaged surface meteorological data from the *Ronald H. Brown*, for 16–22 August 1997. (a) Shortwave radiation (W m^{-2}), (b) air temperature anomaly (dark line, left scale, K) and SST anomaly (light line, right scale, K), (c) specific humidity anomaly (dark line, left scale, g kg^{-1}) and pressure anomaly (light line, right scale, hPa), (d) total wind direction (dark line, left scale, degrees) and total wind speed (light line, right scale, m s^{-1}).

SST, specific humidity, and pressure; and total wind speed and direction, for 16–22 August. Data were reported at 1-second intervals and averaged to 1-hour intervals. Anomaly time series were created by subtracting the 16-day average daily cycle (8–23 August 1997, at hourly resolution). A slight warming trend (0.042° day^{-1}) was removed

TABLE 1. Average surface observations at the *Ronald H. Brown* for 8–23 August 1997.

Shortwave radiation (daytime)	406 W m^{-2}
Air temperature	27.4°C
Sea surface temperature (SST)	29.0°C
Specific humidity	17.8 g kg^{-1}
Pressure	1008.8 hPa
Wind speed	3.4 m s^{-1}
Wind direction	157°

from the SST time series by a least squares fit. The mean values of the surface variables are shown in Table 1.

Evidence of the cloudiness signal associated with the Kelvin wave passage can be seen in the shortwave radiation time series (Fig. 2.9a). Prior to and subsequent to the disturbance passage, the daily cycle of shortwave radiation is quite evident, with a maximum insolation of approximately 1050 W m^{-2}. During the Kelvin wave passage, however, the shortwave radiation at the ship is very low, with an average daytime value of approximately 150 W m^{-2} (calculated from 1200 UTC 18 August to 1200 UTC 20 August). One day before the Kelvin wave begins to affect conditions in the vicinity of the ship, on 17 August, there is cloud over the ship in early afternoon, around 1900 UTC (1200 LST). However, the profiler and rain rate data for this time period show no associated rainfall. On the two most convectively active days, 18 and 19 August, there appears to be little cloudiness over the ship for the first 3–4 hours after sunrise, followed by a sharp drop in shortwave radiation as cloudiness builds. The maximum drop occurs

at approximately 1800–2000 UTC each day (1100–1300 LST). The lowest overall insolation occurs on 18 August, when the deepest convective signal and highest rain rates are observed at the ship.

Figure 2.9b shows the surface temperature and SST anomaly time series at the ship. Corresponding to the large rain events seen in the profiler and rain rate data are sharp drops in surface temperature (e.g., 1900 UTC 18 August; 0000 UTC 19 August; 2000 UTC 19 August), presumably associated with the evaporative cooling of rainfall in convective downdrafts. Typically, the surface temperature drops 1°–2°C during a strong rain event. This is consistent with observations in the western Pacific of a 1.1°C surface temperature difference between convectively disturbed and undisturbed periods (Young et al. 1992).

The SST anomaly time series generally follows the surface temperature series, with a maximum correlation between the two series of 0.67 when SST lags air temperature by 3 hours. Prior to the Kelvin wave passage, the SST is anomalously warm. As the convection passes over the ship, SST gradually decreases, reaching its lowest value at approximately 0000 UTC 20 August, during the last stratiform rainfall event of the wave passage. After the Kelvin wave convection ends, the SST rises to as high as 0.7°C above average, most notably at 0000 UTC 21 August. This sharp rise in SST, combined with the coincident increase in shortwave radiation, suggests a quiescent, cloud-free, subsident environment following the Kelvin wave passage. Cloud photos taken from the ship on 21 August show only widely scattered shallow cumuli and thin cirrus clouds at this time.

Figure 2.9c illustrates the surface specific humidity and pressure anomalies at the ship. Prior to the Kelvin wave passage, specific humidity increases to a maximum of approximately 1.5 g kg^{-1} above the mean. This maximum occurs at 1000 UTC 18 August, as convection is rapidly building near the ship. As convection becomes more widespread, specific humidity generally decreases, with two intense negative anomalies apparent at 0900 UTC 19 August and 0100 UTC 20 August. These rapid drops in specific humidity are coincident with sharp increases in temperature, suggesting the presence of unsaturated downdrafts in the wake of organized mesoscale convective systems (Zipser 1977). Specific humidity finally climbs back to its average value on 22 August, just prior to the outbreak of the next convective event.

In a theoretical Kelvin wave, pressure and zonal wind should be positively correlated; that is, low pressure should occur during easterlies and high pressure during westerlies, with convergence (and perhaps precipitation, if this structure is observed in the boundary layer of a moist atmosphere) between the easterlies and westerlies (see Fig. 6 in WKW00). The surface observations recorded during the TEPPS Kelvin wave passage are consistent with this theoretical model. Initially, pressure is anomalously low and winds are easterly (Figs. 2.9c, d). As convection begins to build, on 18 August, pressure rises rapidly, and winds veer to southwesterly. This wind shift can also be detected in the direction of motion of large convective elements, as described in Section 2.3.3.1. Wind speed and direction become more variable during the deep convective events, as might be expected. Subsequent to the Kelvin wave convection, pressure falls rapidly (3 hPa drop on 20 August), and winds return to easterly.

In summary, the surface meteorological data collected aboard the *Ronald H. Brown* during the Kelvin wave passage agree well with the expected structure of a large-scale, eastward-propagating convective disturbance. Temperature, SST, and specific humidity exhibit positively correlated low-frequency variations tied to the development and decay of deep convection. Surface pressure and winds agree well with the theoretical structure of a linear Kelvin wave disturbance. These observations suggest that large-scale Kelvin wave dynamics play a role in constraining the shorter-timescale fluctuations at the surface.

2.3.5 Radiosondes and ECMWF reanalysis

In this section, the 4-hourly radiosonde data collected aboard the *Ronald H. Brown* during the TEPPS Kelvin wave passage are analyzed. These data provide a high-resolution time series describing the upper-air dynamical features of the passing Kelvin wave.

The radiosonde data have been linearly interpolated in pressure to regular 10 hPa intervals. Single missing points in time (4%–8% of data) were then filled in by a subsequent linear interpolation. Anomalies were created by subtracting from each individual interpolated sounding the average value at each vertical level for the entire ITCZ portion of TEPPS (8–23 August 1997).

For comparison purposes, vertical structure plots based on ECMWF reanalysis dynamical fields are also presented. Rather than directly comparing the vertical structures for the TEPPS time period, however, we instead create a statistical composite Kelvin wave disturbance from the ECMWF reanalysis data to compare with the TEPPS

radiosonde data. This is done to reduce the impact of any inherent model bias or random errors that would be apparent in the comparison of a single episode from the reanalysis with simultaneous radiosonde measurements. In addition, since the ECMWF reanalysis dataset extends only from 1979 to 1993, a comparison with the 1997 TEPPS data preserves the independence of the two samples.

The "composite" Kelvin wave fields are calculated by linearly correlating and regressing the reanalysis dynamical fields (e.g., temperature, wind) against the Kelvin wave filtered OLR at the closest grid point to the location of the *Ronald H. Brown* during TEPPS (7.5°N, 125°W), for the 15 Northern Hemisphere summers (JJA) from 1979 to 1993. This technique is more thoroughly described in WKW00. The daily ECMWF reanalysis fields include 16 pressure levels in the vertical, from 1000 to 10 hPa. The regressions are calculated at successive temporal lags, such that time–height vertical sections at the TEPPS basepoint can be created to compare with the TEPPS radiosonde data.

2.3.5.1 Temperature

Time–height plots of temperature from the TEPPS radiosonde data and the ECMWF reanalysis regression are presented in this section. Figure 2.10a shows the TEPPS radiosonde temperature anomalies from 16–21 August 1997. The plot includes a total of 6 days of data (37 soundings), centered around 1800 UTC 18 August, when the OLR at the grid point closest to the ship (7.5°N, 125°W) reached its minimum value. The data series has been smoothed 3 times each in time and height with a 1-2-1 filter.

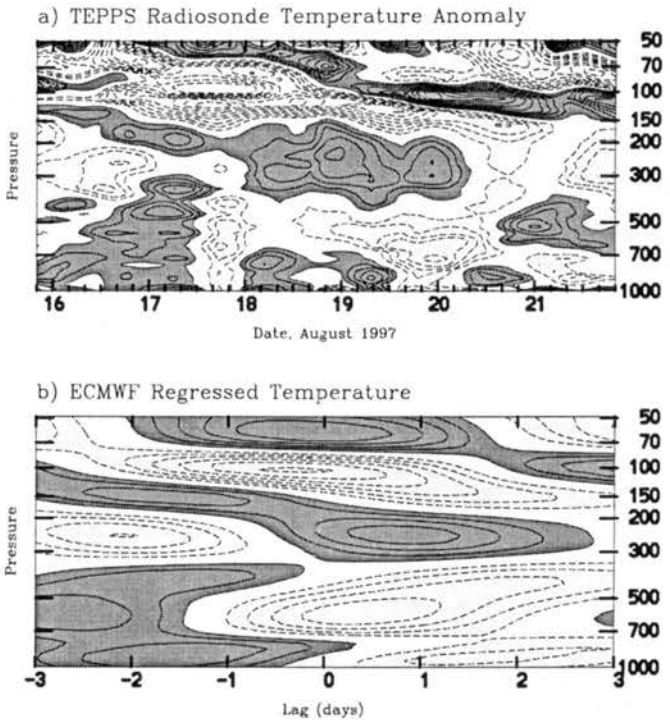


Figure 2.10: (a) TEPPS 4-hourly radiosonde temperature anomalies for 16–21 August 1997, from 1000 to 50 hPa. (b) Regressed daily ECMWF temperatures from day –3 to day +3, based on a –125 W m^{-2} anomaly in OLR at the TEPPS basepoint on day 0. Contour interval in both plots is 0.3 K, with zero contour omitted. Dark shading represents positive anomalies.

Figure 2.10b is the corresponding regressed temperature plot from the ECMWF reanalysis. The regressed values are scaled to a –125 W m^{-2} anomaly in OLR on Day 0, which represents the lowest observed value of OLR (110 W m^{-2}) during the TEPPS Kelvin wave passage relative to the long-term mean at that gridpoint (235 W m^{-2}). This OLR anomaly represents both the Kelvin and non-Kelvin components of convection observed at the *Ronald H. Brown* during TEPPS. The regressions are scaled to this value so as to provide a realistic comparison with the radiosonde data, in which the temperature

anomalies are presumably influenced by the total convection, not just that associated with the Kelvin wave.[2]

The regressed temperature plot extends from Day –3 to Day +3, spanning the same time interval as the radiosonde plot (6 days). In a similar manner to the radiosonde plot, the reanalysis plot is centered around the time of lowest OLR at the basepoint (which is defined as Day 0 in the regression). Because of the statistical reduction of noise achieved by including many events in the regression, there is no need to smooth this plot.

The radiosonde and reanalysis plots have many important features in common. As will be discussed throughout the remainder of this paper, a number of these features resemble the theoretical structure of a linear, dry, vertically-propagating Kelvin wave (Andrews et al. 1987). Beginning in the stratosphere and upper troposphere, above about 250 hPa, there is a downward phase propagation of temperature in both plots, with alternating warm and cold anomalies in the vertical. This structure is predicted by linear theory for a vertically propagating Kelvin wave, where phase lines tilt upward and eastward, parallel to the direction of energy dispersion (Andrews et al. 1987). At a fixed point, then, one would expect a downward propagation of phase with time as a Kelvin wave propagated past, which is seen in Figs. 2.10a and 2.10b. This suggests that the upper troposphere and lower stratosphere are responding in a linear, dry dynamical

---

[2] The amplitude of the regressed temperature anomalies would be reduced by a factor of 2.5 if they were scaled to the observed Kelvin wave filtered OLR anomaly (50 W m^{-2}) instead of the total OLR anomaly (125 W m^{-2}). In this case, the amplitudes of the reanalysis and radiosonde data in Figs. 9 and 10 would not agree quite as favorably. However, considering that there are no regularly reported radiosonde data near the location of the *Ronald H. Brown* which are assimilated into the ECMWF reanalysis, we feel that even an agreement within a factor of 2.5 is noteworthy.

fashion to the presumed upper tropospheric heat source associated with the Kelvin wave convection. The observed vertical wavelength of temperature perturbations in the stratosphere during the TEPPS Kelvin wave is approximately 4–5 km, which is consistent with the theoretical 3–6 km vertical wavelength for dry Kelvin waves of equivalent depth 12–50 m, based on typical stratospheric values of scale height (6.1 km) and lapse rate (+2.5 K km^{-1}), as discussed in WKW00. The close correspondence of the radiosonde and reanalysis plots to one another in this region further suggests that the ECMWF global model is realistically capturing both the heating associated with these fast-moving Kelvin waves and the dynamical response associated with this heating.

A significant warm anomaly is centered at approximately 250 hPa in both the radiosonde and reanalysis plots, around the time of minimum OLR. This timing strongly suggests that the warm anomaly is caused by upper tropospheric latent heating in the Kelvin wave convective envelope. In the radiosonde data (Fig. 2.10a), the warm anomaly stretches from approximately 0000 UTC 18 August to 0400 UTC 20 August, the same time period when convection is active near the *Ronald H. Brown*. The maximum anomaly occurs around 0000 UTC 19 August, during the strongest convective rain event of the Kelvin wave passage (see Fig. 2.7).

The overall warm anomaly lasts for approximately two days in both the radiosonde and reanalysis data, with a peak amplitude of at least 1.2 K. However, the warm anomaly is centered about a day later in the reanalysis than in the radiosonde data. This result is somewhat surprising, since the regressed vertical motion (not shown) is maximized in the upward direction on Day 0, coincident with the minimum OLR. This

suggests that an additional diabatic or dynamical mechanism is contributing to the upper tropospheric warming in the composite ECMWF Kelvin wave.

In the lower troposphere, the observed vertical structure of temperature is not as clearly related to the predicted linear response as in the upper troposphere and stratosphere. This is most likely caused by interactions between the Kelvin wave convective heating and dynamics. However, there is still a good correspondence between the radiosonde and reanalysis temperature structures in the lower troposphere, with warm anomalies preceding the convective maximum, and cold anomalies following it. This agreement suggests that the reanalysis is realistically capturing the large-scale structure resulting from these interactions.

2.3.5.2 Zonal Wind

Figures 2.11a and 2.11b show the zonal wind anomaly for the TEPPS radiosonde data and the ECMWF reanalysis composite, respectively. As in the temperature analyses, the correspondence between the two structures is excellent. In the stratosphere and upper troposphere, an easterly zonal wind anomaly propagates downward over the 6-day period from 50 to 200 hPa. In the reanalysis composite, this easterly anomaly is sandwiched between westerly anomalies, which also propagate downward in time. The upper westerly anomaly in the reanalysis appears to correspond to the westerlies centered at about 100 hPa on 20–22 August in the radiosonde data. In both figures, the stratospheric and upper tropospheric zonal wind anomalies are in quadrature with the corresponding temperature anomalies in Fig. 2.10, as is expected based on the theoretical structure of a linear Kelvin wave.

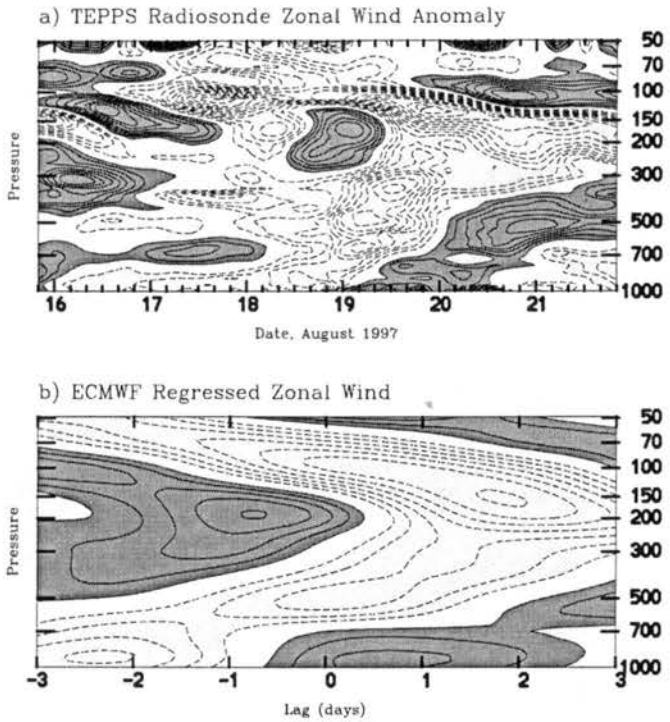


Figure 2.11: As in Fig. 2.10 except for zonal wind. Contour interval is 1.0 m s^{-1}.

The downward-propagating anomalies in the stratosphere and upper troposphere intersect at about 200 hPa with upward-propagating anomalies in the lower troposphere, in both the radiosonde and reanalysis plots. These two features lead to a "boomerang"-like shape in the wind anomalies, as was also noted in the Kelvin wave temperature field in WKW00.

At approximately 200 hPa, there is a pronounced shift from westerly to easterly anomalies just after Day 0 in the reanalysis, and just after the maximum convective anomaly in the radiosonde data (at about 1200 UTC 19 August). This shift reflects the zonal component of the upper tropospheric divergence associated with the large-scale convective outflow. At the surface, on the other hand, the wind shifts from easterly to westerly approximately 12–24 hours prior to the upper tropospheric wind shift. The difference in the timing of the wind shift is due to the tilted structure of the wind and

temperature anomalies in a Kelvin wave forced by upper tropospheric heating (Holton 1972). This structure allows convergence at the surface to precede the convective anomaly, facilitating the eastward propagation of the convective envelope and the wave structure as a whole.

TAO buoy data

To further analyze the zonal wind structure associated with the Kelvin wave passage during TEPPS, data from Tropical Atmosphere Ocean (TAO) buoys in the central and eastern Pacific are presented in this section. A map of TAO buoy locations can be found in Kessler and McPhaden (1995). Hourly data were obtained for buoys from 0°–8°N, 155°E–95°W, for 8–23 August 1997. All available data for each longitude were averaged at each time. Anomalies were then created by subtracting the 8–23 August mean at each longitude.

Figure 2.12 is a Hovmöller diagram of zonal wind anomalies from the TAO array during the TEPPS Kelvin wave passage. The dark solid contours represent the Kelvin wave filtered OLR, also shown in Fig. 2.3. Note the changeover from easterly anomalies prior to the OLR minimum to westerly anomalies during and after the convection. These wind anomalies propagate eastward with the same phase speed as the convection. However, the zonal wind anomalies do not appear to be smoothly eastward-propagating features; instead, they are more localized in space and time. When the location and timing of the westerly wind maxima in Fig. 2.12 are compared with the total OLR minima in Fig. 2.3, the correspondence is good, suggesting a strong relationship between the deepest convection and anomalous surface westerlies.

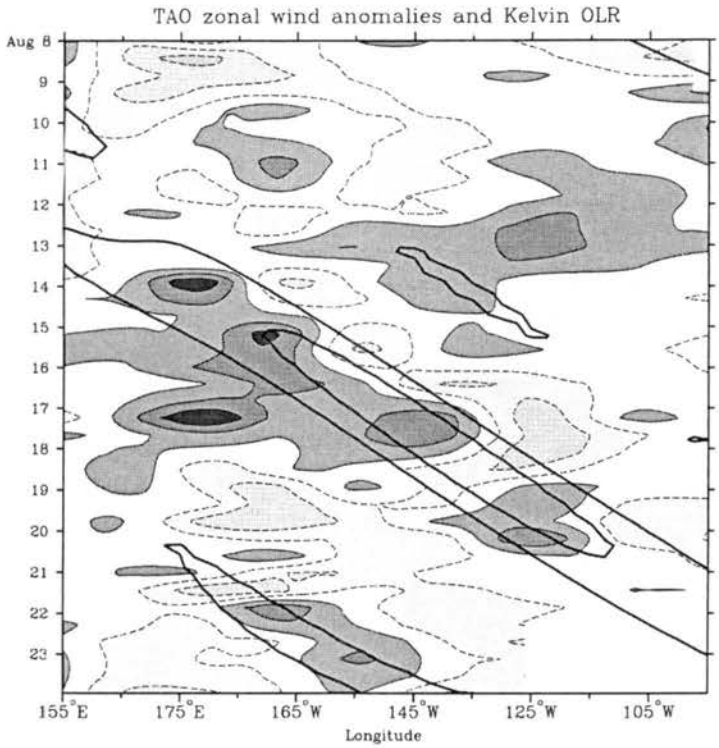


Figure 2.12: Hourly TAO zonal wind anomalies, averaged from 0°–8°N, for 8–23 August 1997. Values have been smoothed with one pass of a 1-2-1 filter in time. Contour interval is 2 m s^{-1}, starting at ±1 m s^{-1}. Dark shading represents positive anomalies. Dark solid lines represent twice-daily Kelvin wave filtered OLR, averaged from 0°–10°N, contoured at –10 and –30 W m^{-2}.

For comparison, Fig. 2.13 is a Hovmöller diagram of 1000-hPa zonal wind from the ECMWF composite Kelvin wave. This composite structure was calculated in the same manner as in Fig. 2.11b, by regressing zonal wind at all ECMWF reanalysis grid points against the Kelvin wave filtered OLR at the TEPPS basepoint, again for the 15 Northern Hemisphere summers (JJA) from 1979 to 1993. Fig. 2.13 shows the 1000-hPa zonal wind averaged from 0°–10°N, from Day –11 to Day +5 and 155°E to 95°W. Since the regression is calculated such that the minimum OLR occurs on Day 0, the timing of this minimum is plotted so as to correspond with the minimum OLR at the ship on 19 August in the TAO plot (Fig. 2.12). The solid contours in Fig. 2.13 represent the regressed total OLR anomaly, calculated in the same manner as the zonal wind. Note the

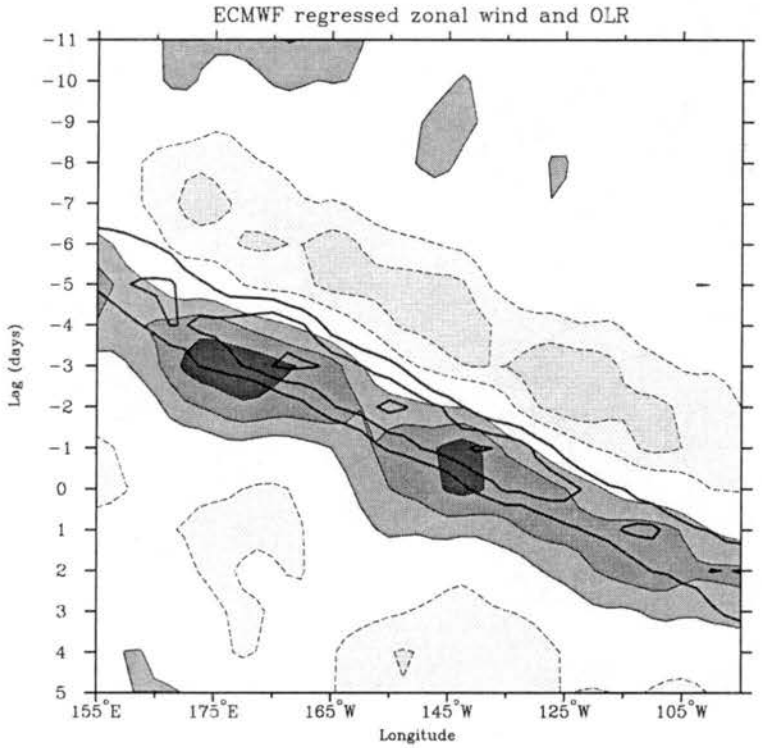


Figure 2.13: Hovmöller diagram of regressed ECMWF daily 1000-hPa zonal wind and OLR from day –11 to day +5, averaged from 0°–10°N, based on a –125 W m^{-2} anomaly in OLR at the TEPPS basepoint on day 0. Contour interval for wind is 1 m s^{-1}, with zero contour omitted. Dark shading represents positive anomalies. Heavy contours represent regressed OLR, contoured from –40 to –80 W m^{-2} in 20 W m^{-2} intervals.

clear eastward propagation of both OLR and 1000 hPa zonal wind in the regressed fields, at a slightly faster speed than in the TAO data, about 17 m s^{-1}. In a similar manner to Fig. 2.12, easterlies precede the convective signal. As the convective anomaly intensifies in time, the 1000-hPa wind anomaly shifts to westerly, and remains westerly while the convection peaks and then dissipates.

2.3.5.3 Specific Humidity

We now return to a comparison of the TEPPS radiosonde data with the time-height reanalysis composite for the specific humidity field. Relative humidity data were

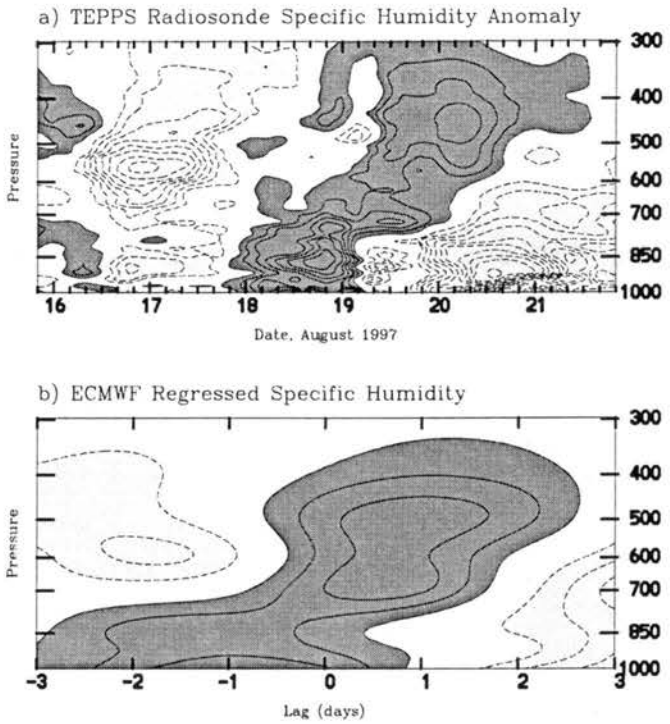


Figure 2.14: As in Fig. 2.10 except for specific humidity. Contour interval is 0.3 g kg^{-1}.

converted to specific humidity so that the large temperature changes associated with the Kelvin wave (see Fig. 2.10a) do not mask changes in total moisture.

Figures 2.14a and 2.14b show the radiosonde and reanalysis specific humidity, respectively, for the 6-day period surrounding the Kelvin wave passage (shown only to 300 hPa). In the radiosonde data (Fig. 2.14a), there appears to be a quasi-periodicity in the specific humidity variations of around 4 days, which is apparent throughout the entire 16-day radiosonde dataset, as also shown by Serra and Houze (2002). These variations are not seen in the reanalysis plot (Fig. 2.14b), most likely because they are due to modes that are not present in the Kelvin filtered dataset.

In the radiosonde data, specific humidity increases in the lower troposphere, below 700 hPa, for about 24 hours prior to the OLR minimum. This moistening of the lower troposphere occurs concurrently with the deepening cumulus observed in the radar

and profiler data on 18 August. The maximum specific humidity anomaly of 2.3 g kg^{-1} occurs near 850 hPa at 2000 UTC 18 August, during the deepest convective event of the Kelvin wave passage. After this event, starting at approximately 0400 UTC 19 August, there is a pronounced shift in the specific humidity profile, with a sharp decrease in low-level humidity and a more gradual increase in humidity above 700 hPa. The lower tropospheric specific humidity anomaly reaches its minimum value, a –3.3 g kg^{-1} anomaly at 930 hPa, at 1200 UTC 20 August, after all convection associated with the Kelvin wave convective envelope has dissipated, and conditions have returned to a suppressed regime. The specific humidity in the mid-troposphere (at approximately 450 hPa), on the other hand, reaches its maximum value (a +1.2 g kg^{-1} anomaly) just prior to this low-level minimum, at approximately 0400 UTC 20 August. This suggests that the mid-tropospheric moist anomaly arises either locally, as a result of the pervasive stratiform convection in the region on 19 and 20 August, or else is advected westward from convection developing to the east of the ship by the mid-level easterlies.

The ECMWF reanalysis composite captures only the grossest features of the specific humidity changes apparent in the radiosonde data. In the lower troposphere, the composite shows a weak moist anomaly beginning three days prior to the peak in convection, and lasting until after the OLR minimum on Day 0. This differs sharply from the rapid buildup of specific humidity in the lower troposphere in the radiosonde data. The reanalysis composite does, however, capture the upward propagation of positive specific humidity anomalies after the peak in convection, and the development of negative anomalies in the lower troposphere several days after this peak.

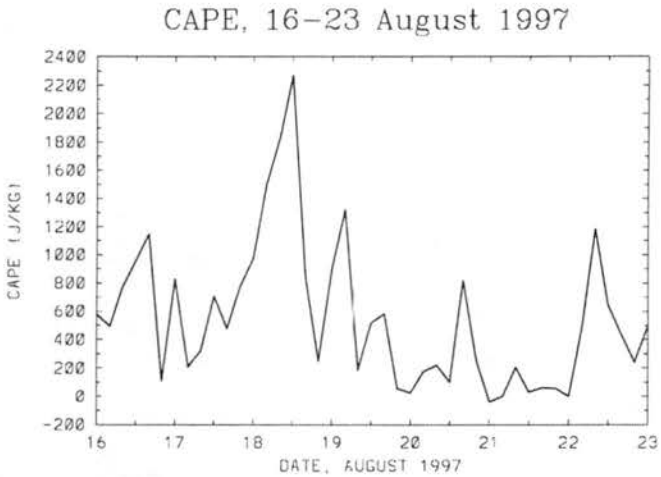


Figure 2.15: CAPE (J kg^{-1}) at the *Ronald H. Brown* from 16 to 23 August 1997, calculated from 4-hourly radiosonde data.

2.3.5.4 CAPE

The radiosonde temperature and humidity profiles allow a calculation of the convective available potential energy (CAPE) as a function of time. In this study, CAPE is defined as the net positive area on a thermodynamic diagram, between the observed temperature sounding and the temperature of a parcel lifted moist pseudoadiabatically from the lifting condensation level to the level of neutral buoyancy (Emanuel 1994).

Figure 2.15 is a time series of CAPE at the ship from 16–23 August. Prior to the Kelvin wave passage, on 16–17 August, CAPE fluctuates around its cruise mean of 650 J kg^{-1}. CAPE then increases dramatically on 18 August, reaching a maximum of nearly 2300 J kg^{-1} at 1200 UTC. This buildup of CAPE coincides with the rapid intensification of deep convection on 18 August as observed in the radar data (Fig. 2.6). The maximum CAPE at 1200 UTC precedes by approximately 3 hours the outbreak of deep convection at the ship as observed by the vertical profiler (Fig. 2.7). The radiosonde data in Figs. 2.10a and 2.14a suggest that this increase in CAPE is due to a substantial warming and moistening of the boundary layer air, and not a cooling aloft.

CAPE decreases rapidly after 1200 UTC 18 August, then reintensifies to another maximum at 0400 UTC 19 August. By 0000 UTC 20 August, when stratiform rainfall is dominant near the ship, CAPE has fallen to nearly zero. This gradual decline can be attributed to a cooling and drying at the surface, as observed in Figs. 2.10a and 2.14a.

The time series of CAPE at the *Ronald H. Brown* illustrates the local effect of the Kelvin wave passage on the potential for deep convection. CAPE builds rapidly as warm, moist boundary layer air is advected westward toward the ship by the low-level easterlies. Deep convection is able to quickly decrease CAPE by both transporting moisture upward and also cooling the boundary layer air via convective downdrafts. In addition, the lower-frequency decline in CAPE can be attributed to the advection of cooler, drier boundary layer air from the west as the Kelvin wave propagates eastward.

2.4 Large-scale wave structure

The similarities between the ECMWF reanalysis Kelvin wave structures and the TEPPS radiosonde data in Figs. 2.10, 2.11, and 2.14 give us confidence that the reanalysis is realistically capturing the dynamics of convectively coupled Kelvin waves. To further investigate these dynamics, the ECMWF regressions are expanded to include all grid points on the globe and all vertical levels. In this manner, the three-dimensional structure of a typical Kelvin wave in the eastern Pacific ITCZ can be assessed.

To give a general overview of the eastward propagation of the Kelvin wave fields, Fig. 2.16 shows the regressed OLR (shading) and 150-hPa temperature (contours) and winds (vectors) on Days –3, 0, and +3, based on a –50 W m^{-2} anomaly in OLR on Day 0 at the TEPPS base point. This OLR anomaly corresponds to a typical perturbation during

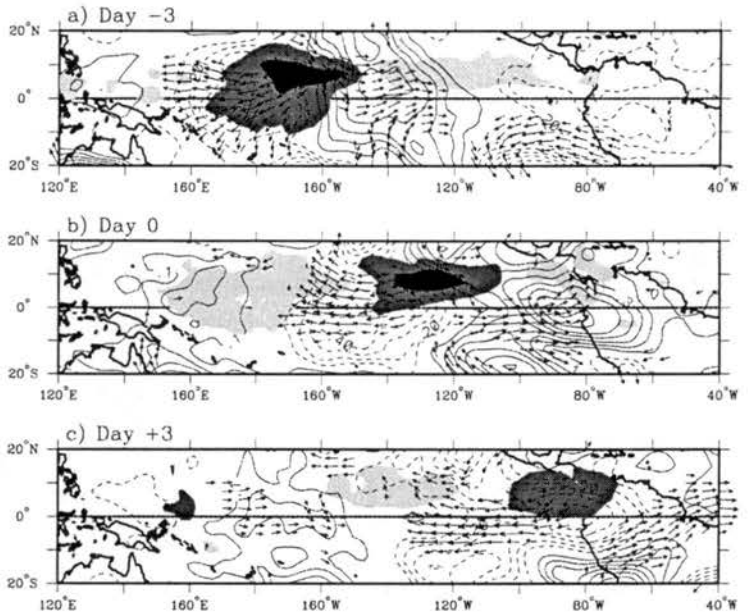


Figure 2.16: Regressed OLR (shading, dark negative, ±10 and 30 W m^{-2}) and 150-hPa temperature (contours, solid positive, contour interval 0.1 K, zero contour omitted) and winds (vectors, maximum 10 m s^{-1}, shown only where 95% significant) for (a) day –3, (b) day 0, and (c) day +3, based on a –50 W m^{-2} OLR anomaly at the TEPPS base point on day 0.

a strong Kelvin wave event, and represents only the Kelvin wave filtered portion of the total OLR anomaly. As shown in Fig. 2.16, the regressed OLR, temperature, and wind signals propagate together to the east at approximately 17 m s^{-1}, which is quite close to the phase speed of the TEPPS Kelvin wave (15 m s^{-1}).

The 150-hPa temperature perturbations are fairly symmetric with respect to the equator in the vicinity of the OLR signal. The zonal component of the wind perturbations is also quite symmetric near the equator at this level (Fig. 2.16; note that winds are plotted as vectors only at a significance level of 95% or greater), although significant off-equatorial, asymmetric wind signals can also be seen. The symmetry in the temperature and zonal wind fields, as well as the geopotential height field, becomes much more pronounced in the lower stratosphere (not shown). The symmetry above 150 hPa is

consistent with the structure of a dry, linear, upward-propagating Kelvin wave, as might be forced by an upper tropospheric heat source (Holton 1972). We consider this signal to be the coherent Kelvin wave response to the upper tropospheric heating associated with the eastward-propagating convective envelope. The temperature response propagates eastward at approximately the same phase speed as the OLR signal most likely because it is being continually forced by the convection. Faster vertically-propagating Kelvin waves may also be excited by this convective heat source (Salby and Garcia 1987); however, these waves are filtered out by the technique used to produce Fig. 2.16, since they radiate away at faster phase speeds and thus are not coherent with the Kelvin filtered OLR signal.

While the regressed 150-hPa winds are predominantly zonal near the equator, they do include a non-negligible meridional component, especially in the vicinity of the enhanced deep convection, e.g., at 10°N, 160°W in Fig. 2.16a. Although a theoretical Kelvin wave is comprised of purely zonal flow, one might expect a moist Kelvin wave in the real atmosphere to contain Rossby-like components associated with the mass circulation due to deep convection. These meridional winds are primarily associated with the off-equatorial location of the divergence signal at 150 hPa, which is collocated with the lowest OLR (not shown). The fact that the winds at 150 hPa do contain these signatures supports the hypothesized coupling between convection and circulation in this wave.

The near symmetry of the upper tropospheric and lower stratospheric perturbations associated with the eastward-propagating deep convection agrees well with linear equatorial Kelvin wave theory. The structure in the lower troposphere, on the other

hand, is not as well accounted for by simple dry linear dynamics, since active convection most likely interacts with the low-level circulation. Interestingly, though, the dynamical symmetry observed above 150 hPa is also apparent throughout the majority of the troposphere, above 850 hPa. The near symmetry of these regressed dynamical fields in the troposphere is somewhat surprising, considering that the convective portion of the wave (as signified by the OLR perturbations) is significantly off-equatorial, especially eastward of 140°W.

At 1000 hPa, however, the temperature and zonal wind fields are centered to the north of the equator, between 5° and 10°N (not shown). As can be inferred from Figs. 2.10 and 2.11, the warmest temperatures and strongest easterly winds are located directly to the east of the lowest OLR signal. Moisture convergence is also strongest to the east of the existing convection. This is consistent with the fact that the OLR signal propagates eastward with time, as new convection is preferentially initiated to the east of existing convection, in the region of strongest low-level moisture convergence. This region of convergence to the east of the heating may simply be the low-level Kelvin response to the tropospheric heat source, as illustrated by Mapes (1998) in a linear vertical spectral band model. Thus it appears that both convection and dynamics play a role in setting the phase speed of the wave structure as a whole.

We note here that the asymmetry in the convective field is not dependent on either the Northern Hemisphere location of the OLR basepoint or the choice of OLR as the filtered variable. Additional regressions were calculated using a basepoint on the equator (0°N, 125°W), based on both Kelvin filtered OLR and Kelvin filtered 100-hPa zonal wind (not shown). Both regressions depict a similar evolution of the OLR signal to Fig. 2.16,

with low OLR propagating eastward at 17 m s^{-1} along the ITCZ, consistent with the maximum in Kelvin wave OLR variability to the north of the equator in the eastern Pacific, as shown in Fig. 2.2.

These results illustrate that the free tropospheric dynamical structure of a Kelvin wave in the eastern Pacific ITCZ may be largely symmetric about the equator, as predicted by theory, while the convection and boundary layer signals maximize to the north of the equator. The off-equatorial location of convection is most likely due to the warm SSTs to the north of the equator in this region, which provide the necessary boundary layer moist static energy to fuel deep convection. Near the equator itself, climatologically cold SSTs in the eastern Pacific cold tongue prevent deep convection from occurring.

While the relationship between convection and dynamics in Fig. 2.16 may be surprising in light of the theoretical Kelvin wave structure, it must be remembered that the theoretical shallow water modes are dry modes of the atmosphere; these modes account for the structure of the divergence field without moisture, but not necessarily the associated precipitation field. Given equatorially asymmetric lower boundary conditions (i.e., SST), it seems reasonable that equatorially symmetric dynamical forcing (e.g., upward motion, wind, or pressure fields) may result in an equatorially asymmetric OLR distribution. We suggest that this is the case in the eastern Pacific ITCZ. This hypothesis is further supported by observations of a systematic shift in Kelvin wave convection toward the equator during warm ENSO events, when the eastern Pacific equatorial cold tongue is significantly weakened (not shown).

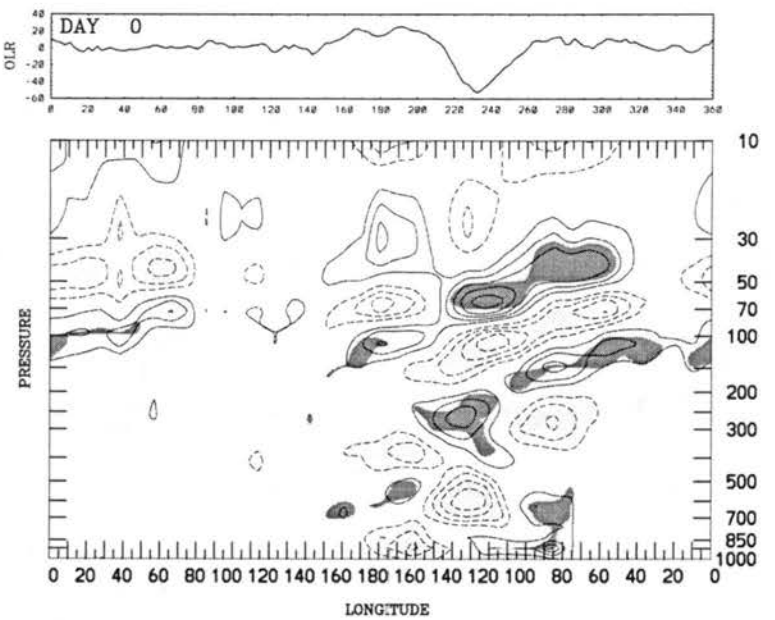


Figure 2.17: Longitude–height cross-section of regressed temperature along the equator on day 0 (bottom), and regressed OLR along 7.5°N (top), based on a –50 W m^{-2} OLR anomaly at the TEPPS basepoint on day 0. Contour interval is 0.2 K, with zero contour omitted. Regions of 95% or greater statistical significance are shaded, with dark shading denoting positive correlations.

The vertical structure of the eastern Pacific composite Kelvin wave also shows many similarities to the theoretically predicted Kelvin wave structure, particularly in the upper troposphere and lower stratosphere, above the heating associated with deep convection. Shown in Fig. 2.17 is a longitude-height cross-section of temperature along the equator on Day 0 (bottom), and an OLR cross-section along 7.5°N (top), where the convective signal is maximized. The temperature phase lines tilt eastward with height in the stratosphere and upper troposphere, and westward with height below about 250 hPa. Note that the stratospheric temperature structure in Fig. 2.17 is similar to that in Fig. 2.10b, but with the x-axis reversed, consistent with a propagating structure. The stratospheric signals are consistent with a vertically propagating Kelvin wave, where energy travels upward and eastward, parallel to lines of constant phase. The phase lines

themselves propagate downward and eastward with time. This structure is consistent with forcing by an upper tropospheric convective energy source, namely the deep convective heating associated with the Kelvin wave.

The Kelvin wave horizontal and vertical structures in the eastern Pacific ITCZ shown in Figs. 2.16 and 2.17 are similar to those calculated for a Kelvin wave in the Indian Ocean region by WKW00 (see their Figs. 5 and 7). This suggests that the Kelvin wave dynamical structures are not strongly affected by differences in basic state winds between the Indian Ocean and eastern Pacific. The horizontal distribution of convection changes from region to region, however, most likely due to changes in the underlying thermal boundary conditions.

2.5 Summary and conclusions

In this study, observations are presented of a convectively coupled Kelvin wave that propagated eastward within the eastern Pacific ITCZ during the 1997 TEPPS field program. These observations represent a unique high-resolution, in situ, multiparameter dataset detailing the convective and dynamical structure of this type of convectively coupled wave.

The large-scale convective envelope of the TEPPS Kelvin wave moves eastward at approximately 15 m s^{-1}, and consists of smaller-scale westward-moving convective elements, similar to observations of "super clusters" within the MJO by Nakazawa (1988). Radar and vertical profiler data show that the large-scale Kelvin wave envelope significantly affects local convection. Convective activity increases rapidly from small-scale, shallow cumulus to deep cumulonimbus within 24 hours, organizing into linear

features that move with the mean low-level wind. Much larger-scale convective and stratiform regions then develop, with stratiform rainfall becoming predominant within the next 24 hours. Convection then dissipates rapidly, within 2–3 hours. The evolution of convection as observed at the *Ronald H. Brown* suggests that a Kelvin wave envelope is much more convectively active on its eastern side, with widespread stratiform precipitation composing the trailing western region.

The dynamical properties of the TEPPS Kelvin wave in the upper troposphere and lower stratosphere are largely consistent with linear equatorial Kelvin wave theory. Locally downward-propagating temperature and zonal wind signals are observed, as would be expected for an upward-propagating Kelvin wave forced by upper tropospheric latent heating. At the surface, there is a significant wind shift from easterly to westerly anomalies at the time of deepest convection, which is also observed as a coincident shift in the direction of movement of convective elements.

The TEPPS radiosonde data compare very well with a composite Kelvin wave disturbance calculated from 15 years of ECMWF reanalysis data, suggesting that the reanalysis is accurately capturing Kelvin wave convective variability and its dynamical manifestations. When this composite Kelvin wave structure is expanded to three dimensions, its dynamical structure looks similar to the Kelvin waves in the Indian Ocean studied by WKW00, with wind and temperature anomalies fairly symmetric with respect to the equator. However, the OLR signal in the eastern Pacific Kelvin wave is strongly asymmetric, existing only in the Northern Hemisphere, where SSTs are warm enough to support deep convection. It is thus hypothesized that the dry dynamical structure of Kelvin waves remains intact as these waves propagate eastward into the eastern Pacific

ITCZ, but that their convective signal shifts latitudinally into the region of warmest SSTs. Apparently the maximum in latent heating to the north of the equator is still able to project onto the equatorially symmetric Kelvin wave dynamical mode as the entire structure propagates eastward.

The reanalysis data used in constructing the composite Kelvin wave should continue to be very useful in further diagnosing the full three-dimensional structure of Kelvin waves in the eastern Pacific ITCZ. In addition, we plan to incorporate data from several other field programs in which convectively coupled Kelvin waves were observed [e.g., South China Sea Monsoon Experiment (SCSMEX) and Nauru99] to determine whether the structure we observe in the eastern Pacific ITCZ is truly a global signature. In addition, reanalysis and in situ data will allow the analysis of other equatorially trapped waves, such as mixed Rossby-gravity and equatorial Rossby waves, as well as the modulation of these waves by longer-timescale variability such as the MJO and ENSO.

3 EXTRATROPICAL FORCING OF CONVECTIVELY COUPLED KELVIN WAVES DURING AUSTRAL WINTER

3.1 Introduction

Convectively coupled Kelvin waves are large-scale, eastward-propagating tropical convective disturbances whose spectral characteristics in the deep cloudiness field lie along the theoretical dispersion curves for dry Kelvin waves of shallow equivalent depth (Takayabu 1994; Wheeler and Kiladis 1999; Wheeler et al. 2000, hereafter WKW00; Straub and Kiladis 2002b, hereafter SK02b). Deep convection in these waves propagates eastward at approximately 17 m s^{-1}, and is accompanied by large-scale kinematic and thermodynamic perturbations in the troposphere and lower stratosphere that are broadly consistent with the theoretical internal Kelvin wave response to an eastward-propagating upper tropospheric heat source (Holton 1972; WKW00). Convectively coupled Kelvin waves are thus thought to arise from the interaction between a dry Kelvin mode and moist convective processes. The observed phase speed of convectively coupled Kelvin waves of 17 m s^{-1} is slower than that of dry Kelvin waves observed in the atmosphere, which propagate eastward at 40–50 m s^{-1} (Andrews et al. 1987; Milliff and Madden

1996), and is faster than that of the Madden-Julian Oscillation (MJO), which propagates eastward at 5–10 m s^{-1} (Madden and Julian 1971, 1994).

Previous studies of convectively coupled Kelvin waves have illustrated the observed horizontal and vertical structures of these waves in their developed stage (Takayabu 1994; WKW00; SK02b), but have not addressed the mechanisms by which Kelvin waves might be initially excited. In this paper, we argue that a substantial fraction of convectively coupled Kelvin waves are excited through a distinct forcing from the extratropics.

Convectively coupled Kelvin waves are observed most frequently in the central Pacific intertropical convergence zone (ITCZ) during austral winter (June–July–August, or JJA). During this season, the subtropical jet in the Southern Hemisphere attains its largest amplitude and northernmost position in the vicinity of Australia (see Fig. 3.1), and Rossby waves excited in the jet propagate eastward and equatorward from this region, as shown by Chang (1999) and discussed in more detail in Section 3.4. In the current study, we present observations that link these equatorward-propagating Southern Hemisphere subtropical jet disturbances with the initiation of tropical Kelvin wave activity in the Pacific ITCZ, and suggest a possible dynamical mechanism for this interaction.

This paper is organized as follows. A literature review is presented in Section 3.2. In Section 3.3, the datasets and methodology used in this study are detailed. A climatology of the parameters relevant to Kelvin wave activity during austral winter is presented in Section 3.4. Sections 3.5 and 3.6 discuss the typical horizontal and vertical structures of the circulation anomalies associated with a convectively coupled Kelvin wave in the tropical Pacific. In Section 3.7, the longer timescale relationship between

Kelvin wave activity in the Pacific and the variability of the Southern Hemisphere subtropical jet is described. In Section 3.8, a case study is presented which illustrates the relationship between the extratropical circulation and Kelvin wave activity during two contrasting months. Finally, a summary and conclusions are given in Section 3.9.

3.2 Background

A number of previous observational and modeling studies have explored the relationship between the extratropical circulation and the initiation of tropical convection and equatorially trapped waves. Observations suggest that tropical convection can be forced from the extratropics via pressure surges from strong midlatitude systems in the winter hemisphere (Lau 1982; Love 1985a, b; Hsu et al. 1990; Meehl et al. 1996; Compo et al. 1999), or by an upper tropospheric trough propagating equatorward through the tropics during boreal winter, in a region of equatorial upper tropospheric mean westerlies (Liebmann and Hartmann 1984; Kiladis and Weickmann 1992b, 1997; Kiladis 1998; Liebmann et al. 1999). Williams (1981) and Lau (1982) present case studies of northeasterly cold surges off the Asian continent during boreal winter that are followed by the initiation of equatorially symmetric, eastward-propagating convective anomalies near Borneo. Both authors suggest that these convective anomalies are related to Kelvin waves. Kiladis (1998) presents observations of lower tropospheric equatorially trapped Rossby wave structures initiated following a deep convective outbreak in the eastern Pacific, which itself is initiated by an equatorward-propagating extratropical Rossby wavetrain. Finally, Magaña and Yanai (1995) document a correlation between Southern Hemisphere westward-propagating extratropical circulation anomalies and the initiation

of equatorially trapped mixed Rossby-gravity waves in the central Pacific during boreal summer and fall. In summary, observations suggest that extratropical circulation features may be responsible for forcing some large-scale regions of deep tropical convection, and may also play a role in initiating equatorial waves.

Theoretical and modeling studies have also addressed the topic of the extratropical forcing of equatorially trapped waves and tropical convection. For example, Mak (1969) demonstrates that stochastic forcing at the latitudinal boundaries of a two-level model can excite tropical waves with mixed Rossby-gravity and equatorial Rossby mode characteristics. Lamb (1973) presents solutions to a more complex model, which show that lateral forcing from the extratropics can excite equatorially trapped waves whose structures are then modified by the presence of condensational heating. Lim and Chang (1981) illustrate in a shallow water model that extratropical mass forcing analogous to a lower tropospheric pressure surge excites a spectrum of equatorially trapped waves including Kelvin, mixed Rossby-gravity, and n=1 equatorial Rossby waves. Matthews and Kiladis (2000) excite equatorward-propagating Rossby waves in the eastern Pacific in a baroclinic model by perturbing the climatological boreal winter east Asian jet, and show that lower tropospheric n = 1 equatorial Rossby wave structures can be excited through the addition of diabatic forcing. These studies and others have provided evidence suggesting that equatorially trapped waves can theoretically be forced from the extratropics.

Two additional studies that are particularly relevant to the present work are those of Zhang (1993) and Hoskins and Yang (2000). Both studies find that a *propagating* extratropical vorticity source can force a spectrum of equatorially trapped waves in the

tropics, including Kelvin waves, even in regions of mean tropical easterlies. Previously, it had been thought that such tropical-extratropical interaction would be suppressed in regions of tropical easterlies, based on the Rossby wave propagation theories of Charney (1969) and Webster and Holton (1982). These theories predict that Rossby waves become evanescent at their critical line, where their zonal phase speed equals that of the background zonal wind. However, Zhang (1993) demonstrates that Kelvin wave amplitudes should actually be larger in the presence of equatorial easterlies, for eastward-propagating forcing with periods greater than 6 days. Similarly, Hoskins and Yang (2000) show that the strongest Kelvin wave response to eastward-propagating forcing occurs in tropical easterlies, for low zonal wavenumbers. In general, the equatorial Kelvin wave response is shown to maximize when the Doppler-shifted forcing frequency approaches the modal eigenfrequency, that is, when the local forcing speed matches the theoretical Kelvin wave phase speed for a given basic state flow. These results allow for the possibility of the remote forcing of Kelvin waves from the extratropics even when the equatorial winds are easterly, as is the case in the tropical Pacific during austral winter.

The question then arises as to which Kelvin wave eigenfrequencies (i.e., phase speeds) can be forced from the extratropics in the Earth's atmosphere. Observations show that dry Kelvin waves exist in the tropics over a wide range of frequencies and phase speeds (see Salby and Garcia 1987), but that moist (or convectively coupled) Kelvin waves are constrained to Doppler-shifted phase speeds between 15–20 m s^{-1} (Takayabu 1994; WK99). If, then, convectively coupled Kelvin waves do represent an intrinsic mode of the moist atmosphere, it appears that they could potentially be forced by extratropical vorticity perturbations that also propagate eastward at 15–20 m s^{-1}. We thus

hypothesize that extratropical vorticity forcing in the form of eastward-propagating perturbations in the subtropical jet might be able to force equatorial Kelvin waves, even in the presence of equatorial easterlies. The remainder of this study seeks to show that this is indeed the case in the Pacific during austral winter.

3.3 Data and methodology

Two primary datasets are utilized in this study. NOAA outgoing longwave radiation (OLR) data are used to represent large-scale deep tropical convection, and European Centre for Medium-Range Weather Forecasts (ECMWF) reanalysis fields are used to represent the atmospheric circulation. Both datasets are available globally, on a regular 2.5° horizontal grid, and are averaged to daily time resolution. The reanalysis data are available on 16 pressure levels in the vertical, from 1000 hPa to 10 hPa, and extend from 1979–1993. The OLR data extend from 1979–2001 (Liebmann and Smith 1996).

The relationship between Kelvin wave convection and the tropical and extratropical circulation is determined through a linear regression technique, in a similar manner to many previous studies of this type (Kiladis and Weickmann 1992b, 1997; Kiladis 1998; WKW00; SK02b). The majority of the results in the present study are obtained by linearly regressing daily ECMWF reanalysis fields (horizontal and vertical winds, temperature, geopotential height, and specific humidity) and total OLR against an index of Kelvin wave OLR, for the 15 austral winters (JJA) from 1979–1993, as a function of temporal lag. The Kelvin wave OLR index is constructed by filtering the total OLR data in wavenumber–frequency space such that the output includes only

variability in the region surrounding the climatological Kelvin wave spectral peak (see WKW00 for more details). The filter spans periods of 2.5–17 days and wavenumbers 1–14, specifically isolating disturbances with eastward phase speeds from 8–30 m s^{-1} [see Wheeler and Kiladis (1999), WKW00, or SK02b (Fig. 2.1 in Chapter 2) for an illustration]. A reverse transform in space and time then results in a filtered dataset that includes only variability on these preferred Kelvin wave space and time scales. The Kelvin wave index used in this study is the daily value of the Kelvin wave filtered OLR at the point of its climatological variance maximum in austral winter, which is at 7.5°N, 172.5°W (see Fig. 3.1). The linear regression results based on this index are then scaled to a –40 W m^{-2} anomaly in OLR at the basepoint on day 0, a typical value for a strong Kelvin wave event. The statistical significance of these results is calculated based on a local two-sided significance test, which takes into account the correlation coefficients and a reduced number of degrees of freedom based on the decorrelation timescale, as in Livezey and Chen (1983). Results are considered significant at the 95% level or greater.

To assess the robustness of the relationship between convection and circulation determined from the Kelvin wave filtered OLR, regressions were also calculated based on several other indices of tropical convection and the extratropical circulation. These results show strong similarities with those based on the Kelvin wave OLR, and are discussed in Section 3.5.1. In addition, we have calculated composite disturbances based on strong Kelvin wave events. The composite results are also very similar to those calculated in the regressions, based on both positive and negative OLR perturbations. This suggests a strong linearity in the observed Kelvin wave dynamical fields, and supports the use of the linear regression technique.

In Section 3.7, 200-hPa NCEP/NCAR reanalysis data are used in place of the ECMWF reanalysis data in constructing composites of monthly averaged circulation parameters related to Kelvin wave activity in the Pacific, because of the longer data record, which extends from 1979–2001. The analysis presented in Section 3.7 has been carried out using the overlapping periods of 1979–1993 in both the ECMWF and NCEP/NCAR datasets, and the results are nearly identical, as are the case study results presented in Section 3.8. Finally, monthly-averaged Reynolds sea surface temperature (SST) data are utilized in Section 3.8. These data were obtained from the NOAA–CIRES Climate Diagnostics Center on a 1° grid, and interpolated to a 2.5° grid to match the resolution of the OLR and reanalysis data.

3.4 Climatology

Before discussing the regression results, we first review the climatological background fields from which disturbances originate, and through which they propagate. Figure 3.1 shows the JJA climatological values of total OLR (dark shading), 200-hPa zonal wind (light contours), Kelvin wave filtered OLR variance (dark contours), 200-hPa <30 day filtered meridional wind variance (light shading), and 200-hPa <30 day filtered E-vectors. The E-vectors are defined as:

$$E = \left(\overline{v'^2 - u'^2}, -\overline{u'v'}\right)$$

(Hoskins et al. 1983), where u and v are the zonal and meridional wind, respectively, the primes represent <30 day filtered fluctuations and the bars represent a climatological average over the JJA season from 1979–1993. The <30 day filtered meridional wind variance and <30 day E-vectors are intended to provide a qualitative measure of the

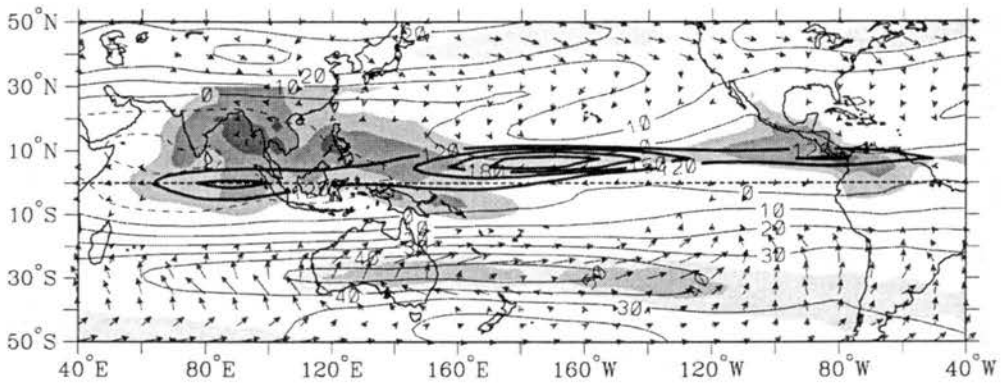


Figure 3.1: Austral winter (JJA) climatological values of total OLR (dark shading), Kelvin wave filtered OLR variance (dark contours), 200-hPa zonal wind (light contours), <30 day filtered 200-hPa meridional wind variance (light shading), and <30 day filtered E-vectors, based on the years 1979–1993. OLR is shaded at 200, 220, and 240 W m^{-2}, and is set to zero outside the range 20°S–30°N for plotting purposes. Kelvin OLR variance is contoured from 120 to 210 W^2 m^{-4} by 30 W^2 m^{-4}. Zonal wind is contoured every 10 m s^{-1}. Meridional wind variance is shaded at 160 and 200 m^2 s^{-2}. Longest E-vectors are 150 m^2 s^{-2}; vectors are not plotted below 10 m^2 s^{-2}.

amplitude and direction of propagation of upper tropospheric extratropical wave activity. In a quasigeostrophic framework, the E-vectors point in the approximate direction of the group velocity of a wave packet (Hoskins et al. 1983). The studies of Zhang (1993) and Hoskins and Yang (2000) motivate the selection of these parameters, as both studies have shown in model simulations that equatorial Kelvin waves can be excited by a transient vorticity source in the extratropics. The <30-day time scale was chosen to represent a broad band of submonthly fluctuations, while also removing intraseasonal and interannual variability.

The total OLR field in Fig. 3.1 (dark shading) is dominated by convection in the Asian monsoon region. Low OLR extends across the Pacific ITCZ, from the Maritime Continent to the coast of Central America, along 5°–10°N. The distribution of subseasonal convective variance closely follows the distribution of OLR, with greater subseasonal variance in regions of lower OLR (not shown). In the central Pacific,

between the two centers of intense convective activity in the Asian and North American monsoon regions, lies the maximum in Kelvin wave activity, as represented by the variance of the Kelvin wave filtered OLR (dark contours). The maximum variance lies to the north of the equator, just to the east of the Dateline, with high variance extending along the latitude of maximum total convection (minimum OLR). Note that the maximum in Kelvin wave activity is collocated with a relative *minimum* in total convection along the ITCZ. A similar overall relationship emerges between Kelvin wave OLR variance and a variety of parameters representing overall convection and the large-scale moist environment in the Pacific, including total OLR variance, SST, and boundary layer equivalent potential temperature (not shown). These relationships suggest that while tropical Kelvin wave activity is modulated by the large-scale lower boundary conditions (that is, activity exists only in regions satisfying certain threshold conditions on low-level moisture, SST, etc.), other factors are involved in determining the distribution of this activity within the ITCZ.

Figure 3.1 also shows the 200-hPa zonal wind field (light contours) during austral winter. The extratropical wind field is dominated by the Southern Hemisphere subtropical jet, which maximizes to the east of Australia along 30°S. Extending along the jet core is a distinct maximum in submonthly meridional wind variance (light shading), which stretches from Australia eastward to approximately 120°W. The meridional wind variance is chosen as a proxy for extratropical Rossby wave activity. A similar distribution of activity is also found using streamfunction or vorticity variance. The preferred direction of energy propagation of these submonthly jet perturbations can be estimated by the direction of the E-vectors, which point northeastward. It thus appears

that during austral winter, submonthly Rossby wave perturbations in the subtropical jet tend to propagate eastward and equatorward in the vicinity of Australia. The equatorward propagation of individual Rossby wavetrains should theoretically be facilitated by the existence of westerlies at relatively low latitudes in the central Pacific, allowing Rossby waves to propagate quite close to the equator before they are influenced by their critical line (Webster and Holton 1982).

Observations by Chang (1999) show that the dominant wave propagation pattern in this region during austral winter is consistent with the above conclusions. A wavetrain of zonal wavenumber 6 propagates eastward over the south Indian Ocean at approximately 8–12 m s^{-1}. When this wavetrain reaches Australia, it splits into two branches. The stronger northern branch propagates northeastward, toward the equator, and the weaker southern branch continues to propagate eastward along 50°–60°S. This preferred wave pattern will be shown in Section 3.5 to be associated with the initiation of convectively coupled Kelvin waves in the central Pacific.

3.5 Horizontal structure

In this section, results are presented that link equatorward-propagating transient wave activity over Australia to the initiation of a convectively coupled Kelvin wave in the Pacific. The results are based on linear regressions of ECMWF reanalysis data against the Kelvin filtered OLR index at the basepoint 7.5°N, 172.5°W, for the 15 austral winters from 1979–1993, as described in Section 3.3.

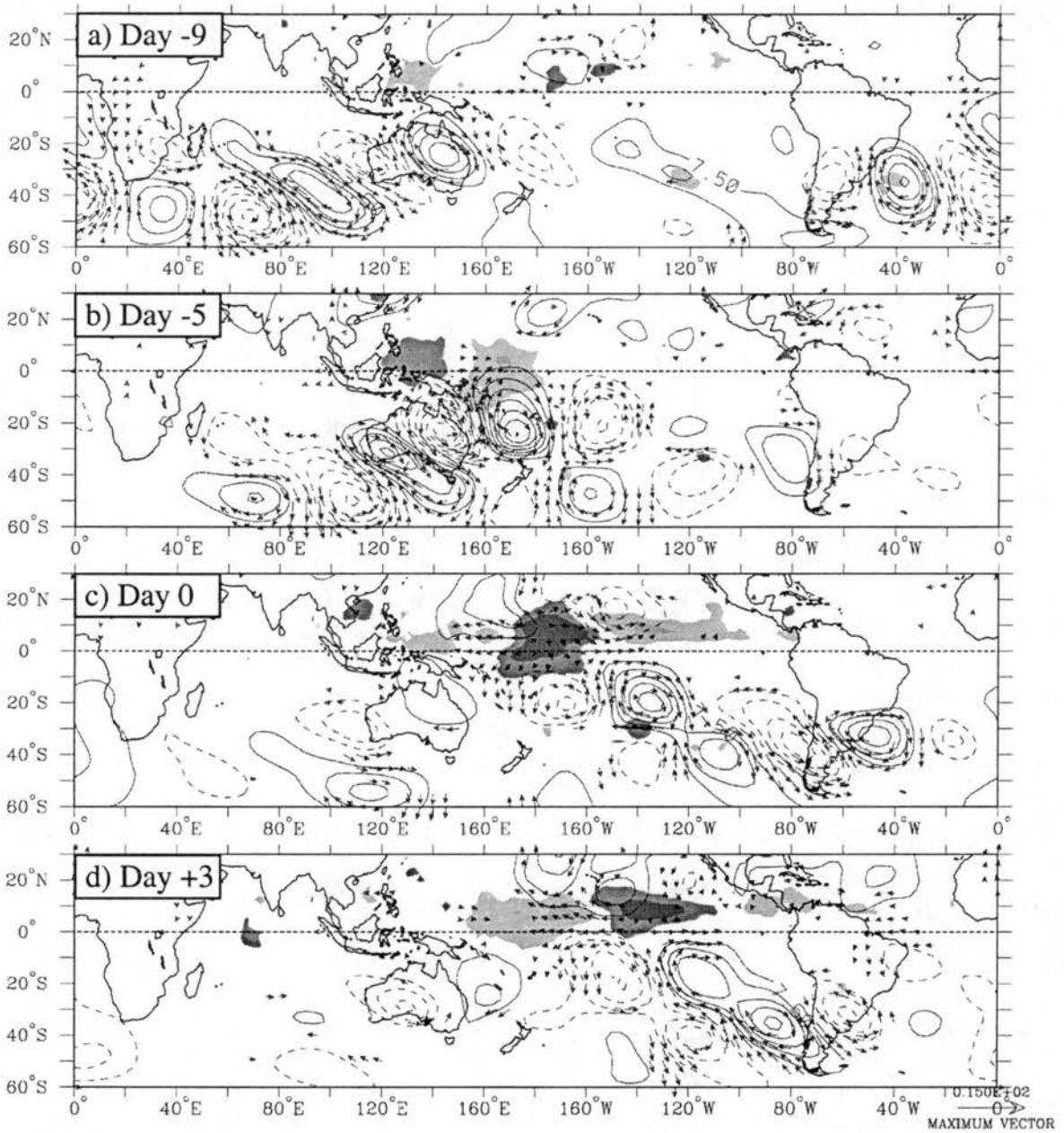


Figure 3.2: Regressed values of OLR (shading) and 200-hPa streamfunction (contours) and winds (vectors), based on a –40 W m^{-2} anomaly in Kelvin wave filtered OLR at the basepoint on day 0, for (a) day –9, (b) day –5, (c) day 0, and (d) day +3. OLR is shaded at ±6 and 15 W m^{-2}; dark shading represents negative OLR anomalies. Streamfunction contour interval is 7.5 x 10^5 m^2 s^{-1}; the zero contour has been omitted. The longest wind vectors correspond to a 10 m s^{-1} wind, and are plotted only where either the *u* or *v* component is significant at the 95% level or greater.

3.5.1 200 hPa

Figure 3.2 shows the regressed values of OLR (shading) and 200-hPa streamfunction (contours) and winds (vectors, plotted only where significant at the 95% level or greater), for days –9, –5, 0, and +3. On day –9 (Fig. 3.2a), a highly statistically significant wavetrain in the Southern Hemisphere stretches eastward from South America to the east of Australia, near the Dateline. This wave packet propagates eastward in time, with new circulation centers forming to the east of existing centers, due to the eastward dispersion of energy. The wavetrain splits into two branches to the east of Australia, as seen on day –5 in Fig. 3.2b, with the stronger northern branch first propagating equatorward and then eastward along 20°S, and the weaker southern branch propagating eastward along approximately 50°S. This wavetrain pattern represents the preferred dispersion path for energy in the Southern Hemisphere subtropical jet during austral winter (Chang 1999), as discussed in Section 3.4. The positive tilt of the anomalies in the northern wavetrain, from northwest to southeast, implies an equatorward transport of wave energy and a poleward transport of westerly momentum. The structure, tilt, and spatial scale (zonal wavenumber 6) of the circulation anomalies on day –5 are reminiscent of the LC1 baroclinic wave life cycle of Thorncroft et al. (1993, their Fig. 7), suggesting that these disturbances may represent the most unstable baroclinic mode of the subtropical jet.

Low (high) OLR, indicating enhanced (suppressed) deep convection in the tropics (or upper-level cirrus in the subtropics) and represented by the dark (light) shading, forms to the northwest of the high (low) pressure center in the northern branch of the wave packet by day –5 (Fig. 3.2b), and is linked with poleward (equatorward) 200-hPa flow to

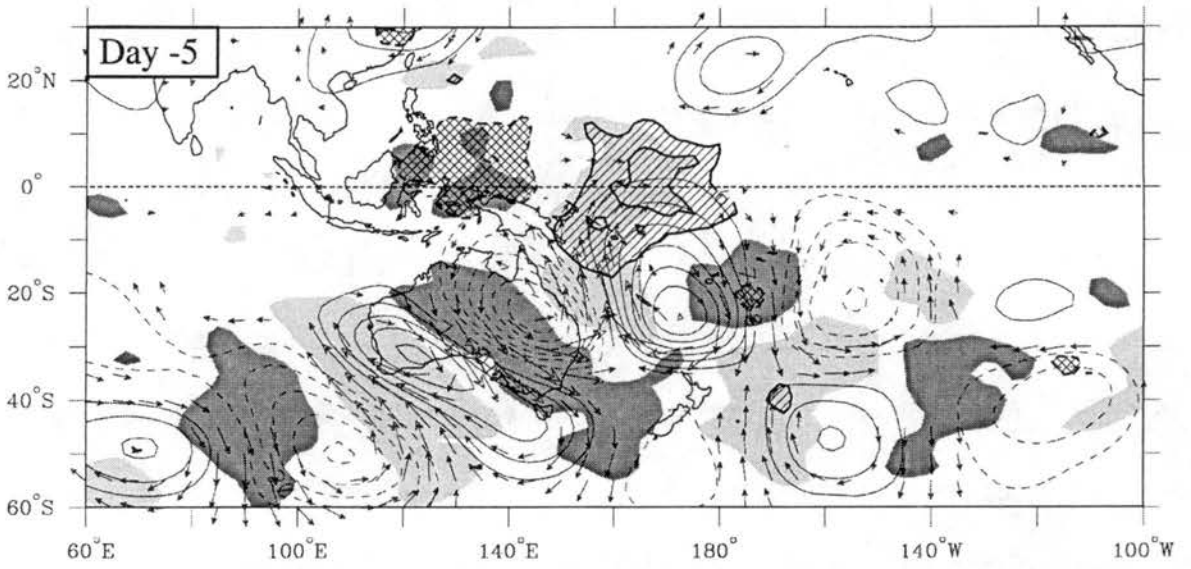


Figure 3.3: As in Fig. 3.2b except that OLR is represented by hatching (cross-hatching negative, single hatching positive), and shading represents 400-hPa vertical motion (dark positive; shading at 0.2 cm s^{-1}).

its south in the Southern Hemisphere subtropics. The horizontal scale of the tropical OLR anomalies is similar to the scale of the subtropical circulation anomalies, with a zonal wavelength of approximately 60°. Anomalous 200-hPa divergence (convergence) exists in the poleward (equatorward) subtropical flow as the wavetrain propagates equatorward (not shown), as might be expected based on quasigeostrophic Rossby wave vorticity arguments. The upper tropospheric divergence fields and their associated vertical motion fields spread northward and eastward as the wavetrain approaches the equator. Figure 3.3 illustrates the 400-hPa vertical motion field on day –5 (shading), along with the OLR (hatching) and 200-hPa streamfunction (contours) and winds (vectors). Low (high) OLR on the equator is collocated with 400-hPa upward (downward) motion, which has propagated into the tropics from the subtropics. Since the extratropical wavetrain exists for several days before the tropical and subtropical Pacific

convective anomalies appear, it is suggested that the circulation forces the vertical motion and cloudiness signals at this time.

In the following days, the tropical and subtropical OLR anomalies propagate eastward in tandem with the subtropical circulation centers at a phase speed of approximately 17 m s^{-1}. By day 0 (Fig. 3.2c), low (high) OLR is located almost directly to the north of the subtropical high (low) pressure cell. It is unclear at this developed stage the extent to which the circulation is forcing the convection, or the convection is forcing the circulation, since upper tropospheric divergence associated with deep convection would be expected to spin up anticyclonic circulations in the subtropics, with the stronger circulation in the winter hemisphere, as observed. In the tropics, the winds diverge from the center of low OLR, suggesting that a substantial portion of the upper tropospheric divergence at this time is due to the deep convection itself.

The deepest convection on day 0, as represented by the negative OLR anomalies in Fig. 3.2c, is centered to the north of the equator, at approximately 7.5°N. Convection continues to maximize in the Northern Hemisphere as it propagates eastward into the eastern Pacific at positive lags (Fig. 3.2d). This off-equatorial shift of convection is believed to be a consequence of the asymmetric SST distribution in the eastern Pacific, where cold SSTs lie along the equator and warm SSTs exist farther to the north (SK02b).

Several additional regressions were calculated to assess the robustness of the above results. First, <30 day filtered OLR was used as the independent variable instead of the Kelvin wave filtered OLR. The results from this regression are similar to those shown in Fig. 3.2, demonstrating that eastward-propagating Kelvin wave OLR anomalies represent the dominant submonthly convective variability in the central Pacific ITCZ

during austral winter. A second regression was then calculated to determine whether an eastward-propagating tropical OLR signal could be detected in a regression in which the independent variable was based purely on an extratropical dynamical field. A regression was calculated using the 200-hPa meridional wind as the independent variable, which was filtered in the same space-time region as the Kelvin wave OLR. This isolates disturbances with eastward phase speeds between 8 and 30 m s^{-1}. The basepoint for this regression was the point of the maximum JJA filtered meridional wind variance, at 27.5°S, 127.5°E. The results using this circulation index are similar to those using tropical Kelvin wave OLR, with an upper tropospheric wavetrain propagating eastward and equatorward over Australia (not shown). The tropical OLR signal is weaker, but still retains the same phase relationship with the circulation anomalies as in the original Kelvin OLR regression. These results clearly demonstrate that Kelvin waves are associated with perturbations in the subtropical jet, and suggest that Kelvin waves might be initiated as a response to the eastward-propagating forcing of the subtropical Rossby wave dynamical fields.

Based on the regressed fields shown in Fig. 3.2 and those discussed in the preceding paragraph, we hypothesize that enhanced (suppressed) convection, as represented by low (high) OLR, is forced at least partially as a response to the upper tropospheric divergence (convergence) field and upward (downward) motion induced by the equatorward-propagating Rossby wavetrain. Of course, the initiation of deep tropical convection depends not only on large-scale vertical motion, but also on the convergence of warm, humid air in the boundary layer. This topic is addressed in Sections 3.5.3 and 3.6.

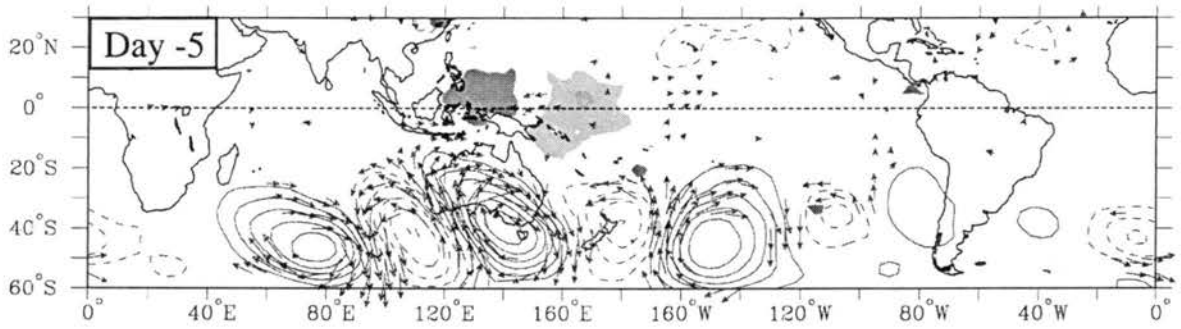


Figure 3.4: As in Fig. 3.2b except at 850 hPa. Streamfunction contour interval is 4.0 x 10^5 m^2 s^{-1}, and longest vectors correspond to a 5 m s^{-1} wind.

3.5.2 850 hPa

Figure 3.4 shows the 850-hPa circulation anomalies on day –5. Only the southern branch of the 200-hPa wavetrain shown in Fig. 3.2b extends into the lower troposphere, with anomalies at 850 hPa centered along approximately 40°S. As the upper tropospheric wavetrain splits into two branches prior to day –5, its equatorward-propagating branch largely decouples from the lower troposphere, while its poleward branch retains a baroclinic structure, with circulation anomalies displaying poleward and westward tilts with height. The northern wavetrain becomes progressively shallower in the vertical as it approaches the equator, due to the influence of the lower tropospheric equatorial easterlies, in a similar manner to the equatorward-propagating Rossby waves in the eastern Pacific studied by Kiladis (1998).

A strong cyclone is centered to the south of Australia near 140°E on day –5, directly to the south of the emerging low OLR anomaly on the equator. It will be shown in the following section that this cyclone affects the low-level tropical wind and pressure fields so as to promote convergence and the initiation of deep convection to its north. Throughout the evolution of the tropical Kelvin wave fields, the southern branch of the

wavetrain remains remarkably coherent, both in the vertical and horizontally with respect to the Kelvin wave OLR anomaly.

3.5.3 1000 hPa

The large-scale extratropical circulation features associated with the growth and decay of the tropical Kelvin wave OLR signal are similar between 850 hPa and 1000 hPa. An interesting feature of the 1000-hPa maps, however, is the existence of Kelvin wave-like height and temperature anomalies in the tropics, which appear to originate as a response to the extratropical baroclinic waves, and which precede the development of the initial convective anomalies.

Figure 3.5 shows the 1000-hPa geopotential height field (Fig. 3.5a) and temperature field (Fig. 3.5b) on day –5, corresponding to the 200- and 850-hPa maps shown in Figs. 3.2b and 3.4. To the east of the high OLR anomaly (single hatching, representing suppressed deep convection) is a region of high heights and low temperatures at 1000 hPa, which has a fairly symmetric distribution with respect to the equator, suggesting a Kelvin wave-like structure. These height and temperature anomalies reached the tropics on day –8 (not shown), having propagated northward from a high pressure system centered to the southeast of Australia, in a surge-like manner similar to that documented by Love (1985a) and analogous to the surges often seen propagating southeastward from Asia in boreal winter (Compo et al. 1999, and references therein). The surge propagates northward at a phase speed of at least 25 m s^{-1}, and is constrained to the lowest 2 km of the atmosphere. Regressions using radiosonde data from Darwin and Alice Springs, Australia for the years 1979–2000 confirm the existence

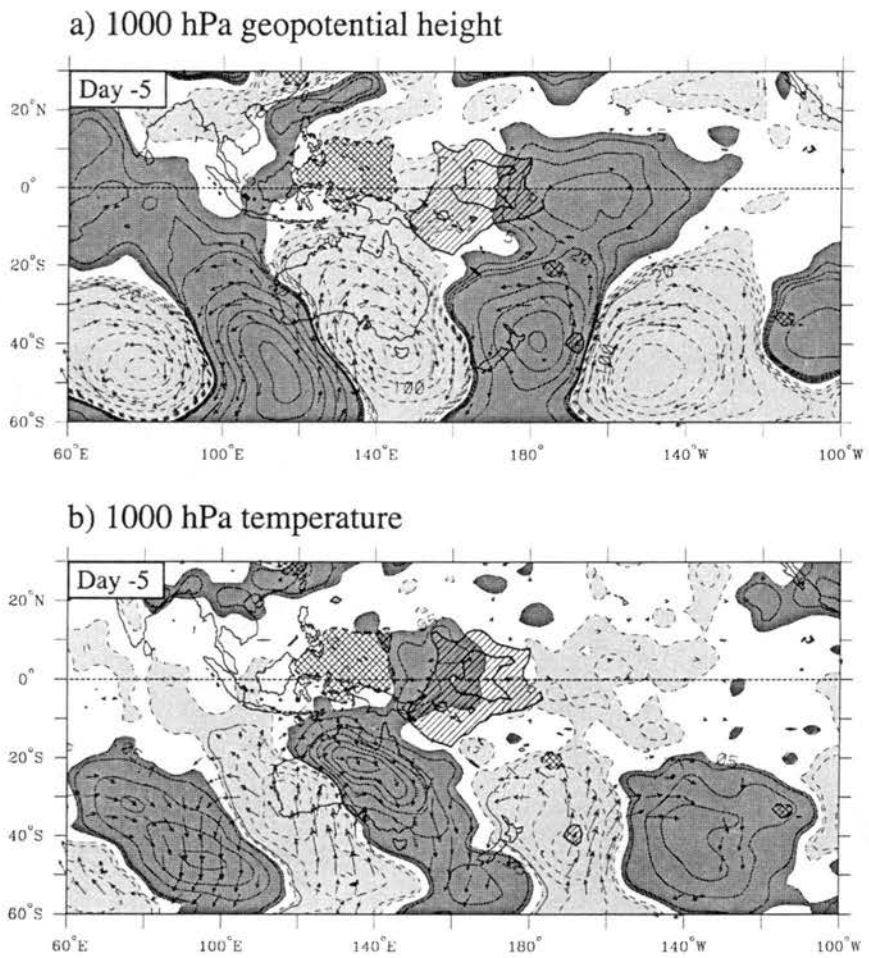


Figure 3.5: As in Fig. 3.3 except at 1000 hPa, for (a) geopotential height and (b) temperature on day –5. Geopotential height contour interval is 5 m from 5 to 20 m, then 40 m; temperature contour interval is 0.05 K from 0.05 to 0.1 K, then 0.2 K. Longest vectors correspond to a 5 m s^{-1} wind.

of the surge, it shallowness, and its timing relative to the initiation of deep convection in the tropics (not shown). The subtropical high responsible for this pressure surge has since propagated eastward to 180° by day –5, and remains connected to the eastward-propagating height anomaly along the equator.

Between the tropical high OLR anomaly at approximately 165°E and the developing low OLR anomaly to its west on day –5 is a similar height and temperature signal of the opposite sign. Low heights and warm temperatures are centered on the

equator, symmetric with respect to the equator, and are linked to extratropical perturbations of the same sign associated with the developing low pressure system centered at 40°S, 145°E. These tropical height and temperature anomalies appear first on day –5, and then propagate eastward in tandem with the tropical convection and extratropical circulation. Note that high (low) 1000-hPa geopotential heights lead high (low) OLR by a quarter wavelength, a relationship consistent with linear Kelvin wave theory if high (low) OLR is considered a proxy for divergence (convergence), as might be expected for the lower troposphere.

The equatorial pressure gradient on day –5 between 150°E and 170°W is followed by the appearance of easterly winds flowing from high to low heights on day –4 between 10°S and 10°N (not shown). The rapid development of tropical wind anomalies in response to an extratropically forced equatorial pressure gradient is also documented by Chu (1988). These easterlies produce a region of low-level zonal wind convergence to the east of the developing low OLR anomaly, which converges moisture and increases the convective available potential energy (CAPE) in this region (not shown). This relationship, of low-level convergence leading low OLR, is retained throughout the evolution of the wave, as shown in Fig. 3.6, a longitude-time diagram of the regressed OLR (shading) and 1000-hPa convergence (contours), averaged from 5°S–10°N. Note that the maximum 1000-hPa convergence leads the minimum OLR by approximately 15° longitude, or less than a quarter wavelength, throughout the wave's life cycle. The regressed 1000-hPa specific humidity, CAPE, and 700-hPa upward motion fields are all in phase with the 1000-hPa convergence (not shown), and thus also lead the minimum OLR by less than a quarter wavelength. The low OLR anomaly is itself in phase with

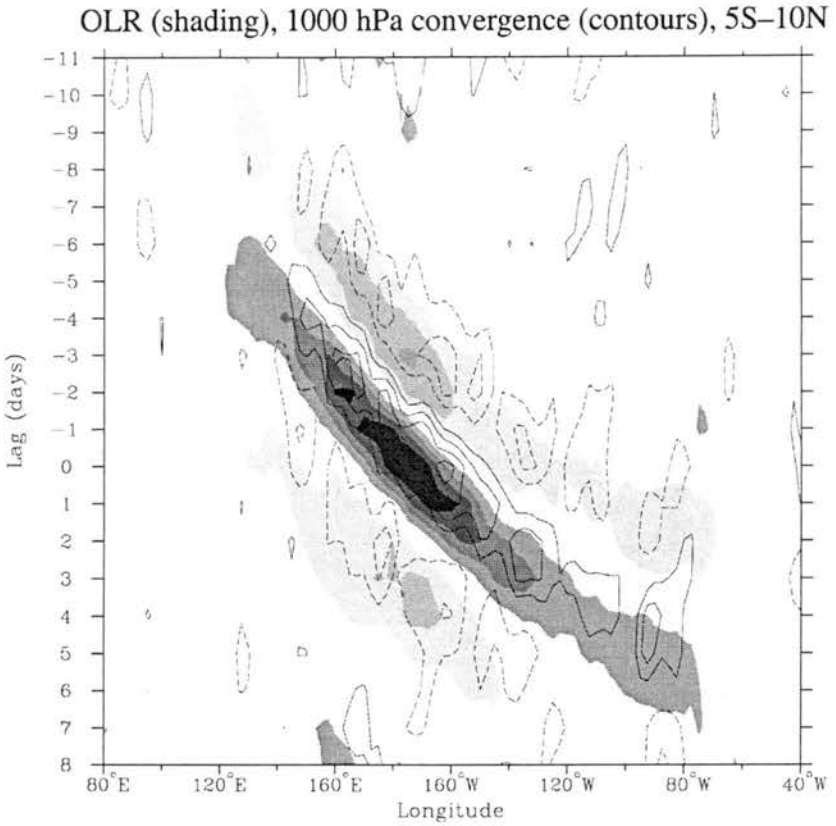


Figure 3.6: Longitude–time diagram of regressed OLR (shading) and 1000-hPa convergence (contours), averaged from 5°S–10°N, from day –11 to day 8. OLR is shaded at intervals of ±5 W m^{-2}, with dark shading representing negative anomalies. Contour interval for 1000-hPa convergence is 2.5 x 10^{-7} s^{-1}, with solid contours representing convergence. The zero contour has been omitted.

400-hPa upward motion. From these relationships we conclude that the deepest convection develops only after a period of lower tropospheric convergence and upward motion, which gradually moistens the lower troposphere over a time span of approximately one day. This idea is consistent with results from a case study of a developed Kelvin wave in the eastern Pacific by SK02b, which show that shallow convection moistens the lower troposphere (below 700 hPa) for approximately 24 hours prior to the lowest OLR anomaly.

Based on the results in this section, it appears that the initial convective anomaly associated with the Kelvin wave is forced by the upper tropospheric upward motion

anomaly that propagates equatorward from the extratropics. The lower tropospheric fields then converge boundary layer moisture to the east of this initial OLR anomaly, creating a region favorable for subsequent deep convection. The wave propagates eastward in tandem with the eastward-propagating subtropical circulation anomalies, but presumably also provides its own internal dynamical and moisture feedbacks that modulate the influence of the extratropical anomalies.

3.6 Vertical structure

In this section, the vertical structures of the extratropical and tropical circulations associated with convectively coupled Kelvin wave OLR signals are examined. The focus in the current study is primarily on the circulations coincident with the development of the tropical OLR anomalies. The developed wave circulations associated with a convectively coupled Kelvin wave in the Indian Ocean region are discussed in WKW00, and Kelvin waves in the Pacific ITCZ are more thoroughly described in Chapter 4.

Figure 3.7a is a longitude–height cross-section along 20°S of the regressed meridional wind (contours), vertical motion (shading), and zonal–vertical circulation (vectors) on day –5. The northern branch of the subtropical Rossby wavetrain (see Fig. 3.2b) is clearly visible in Fig. 3.7a, as evidenced by the vertically coherent positive and negative meridional wind anomalies (contours), which alternate in sign in the horizontal and maximize at 200 hPa. Vertical motion anomalies (shading) are in phase with the meridional wind maxima, with upward (downward) motion below 200 hPa in the regions of northerly (southerly) flow. Opposite signed anomalies occur above 200 hPa. Temperature anomalies along 20°S (not shown) are consistent with the expected structure

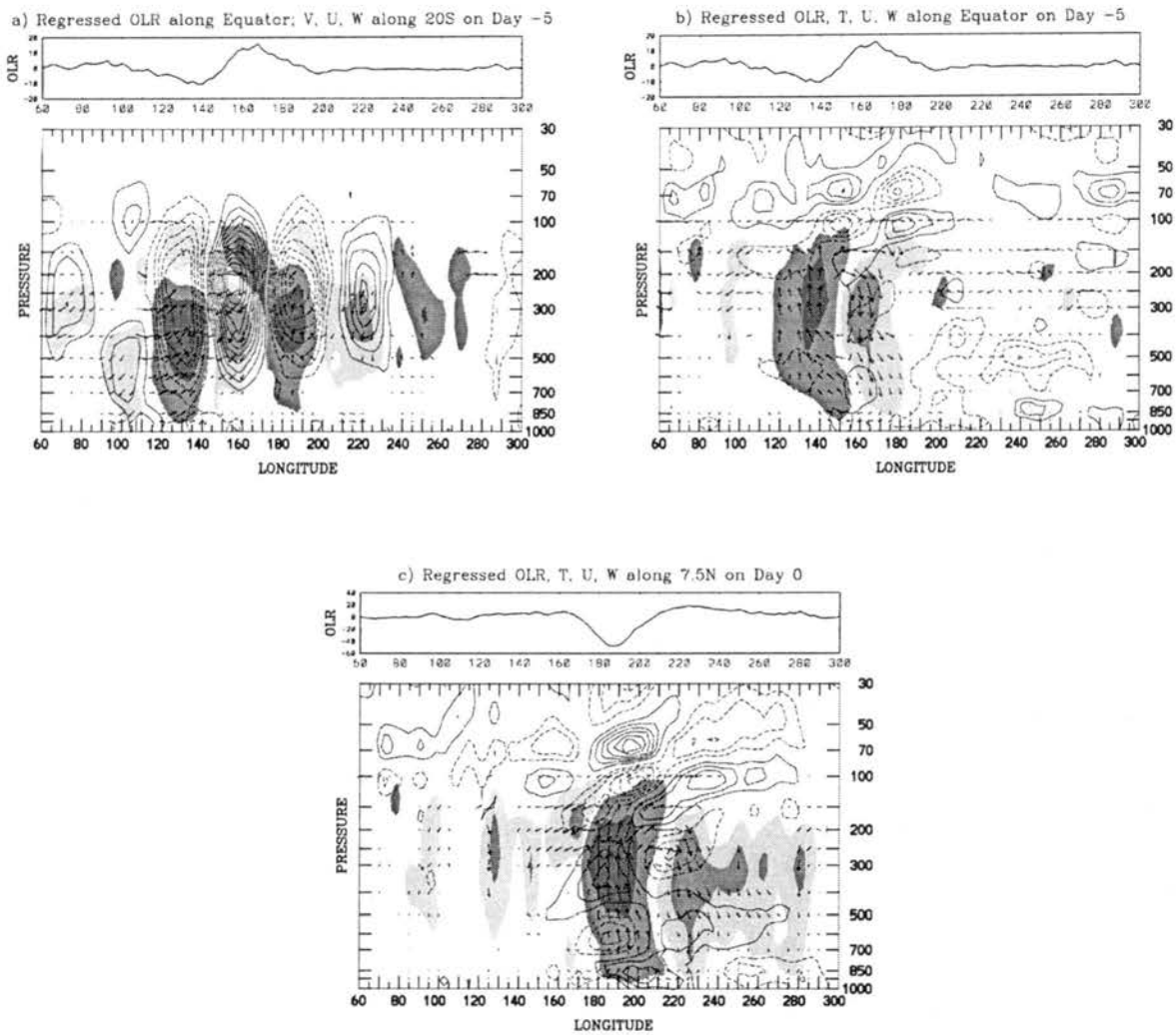


Figure 3.7: Longitude–height cross-sections of regressed (a) meridional wind (contours) and vertical motion (shading) along 20°S (lower plot), and OLR along equator (upper plot), (b) temperature (contours), vertical motion (shading), and OLR along equator, and (c) temperature (contours), vertical motion (shading), and OLR along 7.5°N. Contour interval in (a) is 0.5 m s^{-1}, and in (b) and (c) is 0.1 K, and all zero contours have been omitted. Regressed vertical motion is shaded at ±0.1 and ±0.3 cm s^{-1} in (a) and (b), and at +0.1, +0.6, –0.1, and –0.3 cm s^{-1} in (c). Zonal–vertical circulation is shown by vectors, where the vertical component has been multiplied by 700 to account for the small aspect ratio of the plot. The longest vectors represent winds of (a) 5.0 m s^{-1}, (b) 3.5 m s^{-1}, and (c) 9.0 m s^{-1}.

of upper tropospheric potential vorticity anomalies, with warm (cold) air above and cold (warm) air below the centers of cyclonic (anticyclonic) vorticity.

The vertical motion anomalies centered at 130°E and 160°E in Fig. 3.7a extend northward to the equator in the upper troposphere, as shown in Fig. 3.3 and as also seen in latitude–height cross-sections along these longitudes (not shown). The circulations in the equatorial plane are shown in Fig. 3.7b, a longitude–height cross-section along the equator showing the regressed temperature (contours), vertical motion (shading) and zonal–vertical circulation (vectors) on day –5. Vertical motion anomalies are centered at 135°E and 160°E, directly to the north of those pictured in Fig. 3.7a, with maxima centered at approximately 300 hPa. OLR anomalies (top plot) are consistent with the vertical motion anomalies, with low (high) OLR corresponding to regions of upper tropospheric upward (downward) motion. A zonal–vertical circulation cell is present between 120°E and 180°. Note also that the upward motion field extends eastward below 600 hPa, such that upward motion in the lower troposphere is positioned approximately 15° to the east of that in the upper troposphere. This lower tropospheric upward motion anomaly is horizontally collocated with the maximum 1000-hPa convergence on day –5 (not shown). This relationship suggests that lower tropospheric upward motion is forced to the east of the developing OLR anomaly by the convergence of surface easterlies, which themselves develop in response to the geopotential height fields forced from the extratropics, as discussed in Section 3.5.3.

Also shown in Fig. 3.7b is the regressed temperature field on day –5 (contours). The temperature signals are weak throughout the troposphere at this time, and their relationship to the vertical motion fields no longer resembles the upper tropospheric

potential vorticity anomaly structures at 20°S, where temperature and vertical motion anomalies are in quadrature. Instead, upward (downward) motion in the tropics is collocated with a very weak warm (cold) anomaly in the upper troposphere and a cold (warm) anomaly in the lower troposphere, suggesting the presence of diabatic processes. The weak tropical temperature anomalies also suggest that upper tropospheric cold advection is not a primary factor in the initiation of deep convection in the Kelvin wave. These results contrast with those of Kiladis (1998), who documented strong upper tropospheric cold advection prior to the initiation of deep convection in eastern Pacific equatorward-propagating Rossby waves during boreal winter. Instead, convection in the present study appears to be initiated in regions of upper tropospheric upward motion and low-level moisture convergence forced from the extratropics.

As the coupled convective and dynamical fields of the Kelvin wave propagate eastward, the vertical motion anomalies strengthen and extend throughout the depth of the troposphere. Fig. 3.7c is a longitude–height cross section of temperature (contours), vertical motion (shading), and the zonal–vertical circulation (vectors) along 7.5°N on day 0, when the Kelvin wave OLR has reached its minimum value at the basepoint 7.5°N, 172.5°W (see Figs. 3.2c and 3.4). The vertical motion field retains a westward tilt with height below 600 hPa, such that surface convergence continues to precede the lowest OLR anomaly by approximately 15°. In the region of negative OLR anomalies, between 180° and 160°W, the troposphere is warm above 500 hPa and cold below, and the tropopause is cold (near 100 hPa). This temperature structure is consistent with other studies of convectively coupled tropical waves (Reed and Recker 1971; Dunkerton 1993; Takayabu and Nitta 1993; Haertel and Johnson 1998; WKW00), and suggests the

presence of a tropospheric heat source that includes both deep convective heating and a second baroclinic mode heating over cooling structure which arises from stratiform precipitation. A case study of a convectively coupled Kelvin wave in the eastern Pacific by SK02b shows that both deep convective and stratiform precipitation signals do exist within a developed wave, with stratiform precipitation dominating after an initial convective period.

In the region of positive OLR anomalies in Fig. 3.7c, where deep convection is suppressed, the temperature signal is opposite in sign to that associated with enhanced deep convection. The upper troposphere is cold, and the lower troposphere and tropopause regions are warm. The temperature response of the atmosphere to the convectively coupled Kelvin wave heating fields thus appears to be quite linear, as also documented in composite fields (not shown). In the stratosphere, above 100 hPa, the temperature anomalies tilt eastward with height, as expected for an upward propagating dry Kelvin wave forced from below (Andrews et al. 1987). The vertical wavelength of these temperature anomalies is approximately 6 km, which is consistent with the expected structure of an upward-propagating dry Kelvin wave of equivalent depth 40 m.

3.7 Longer timescale relationships

In this section, the relationship between jet variability and Kelvin wave variance on longer timescales is examined through the calculation of composite, or averaged fields. Monthly averages are used as a simple means of measuring the variability of tropical convection and the extratropical circulation on timescales longer than one typical Kelvin wave event, which lasts approximately 10 days from initiation to dissipation.

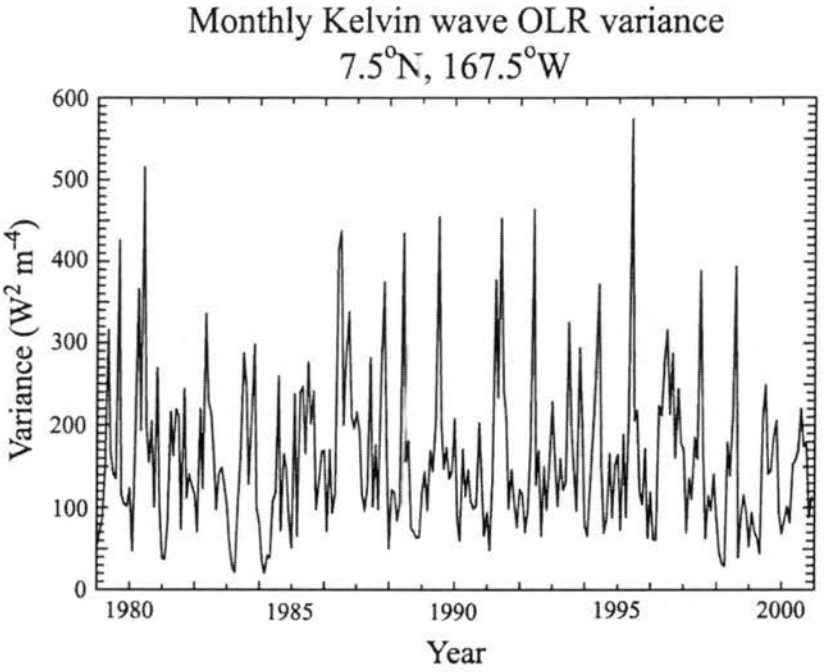
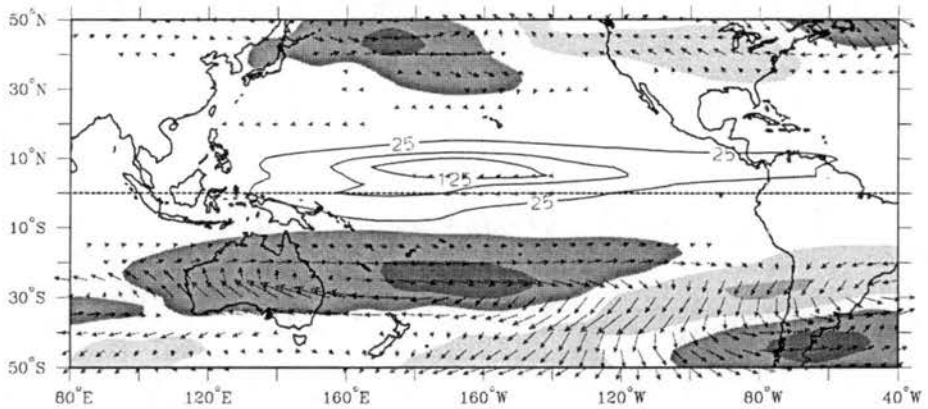


Figure 3.8: Time series of monthly-averaged Kelvin wave variance (in $W^2\ m^{-4}$) at 7.5°N, 172.5°W from January 1979 to December 2000.

A time series of monthly averaged Kelvin wave variance in a 5°x 5° box around the Kelvin wave OLR basepoint (5°–10°N, 170°–175°W) is shown in Fig. 3.8, for the period 1979–2000. Note the highly skewed variability over this 22-year period, with a number of months standing out as containing extremely high Kelvin wave variance. A majority of these months falls within the JJA period: for example, 13 of the 20 months with highest variance occur during JJA. A composite for these high variance events is calculated by averaging months within the JJA season that have a variance greater than one standard deviation above the JJA climatological mean (above 301 $W^2\ m^{-4}$). There are 11 such months. A composite approach is chosen in this context instead of a linear regression approach because, as can be seen in Fig. 3.8, there is no corresponding set of months with anomalously low variance to provide the necessary linearity for such a technique. Instead, a composite of low variance events is calculated based on the 11

a) High variance composite



b) Low variance composite

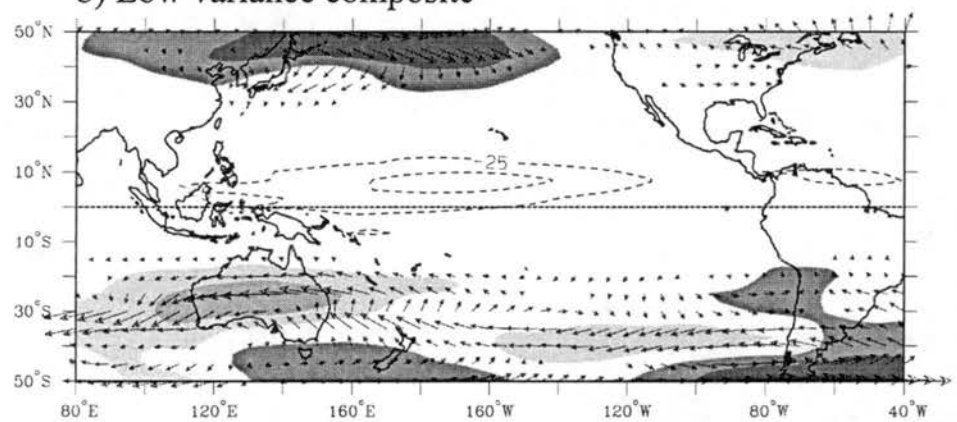


Figure 3.9: Monthly averaged Kelvin wave filtered OLR variance (contours), 200-hPa Kelvin filtered meridional wind variance anomalies (shading), and total Kelvin filtered 200-hPa E-vectors for (a) high and (b) low variance composites, based on the 11 months during the JJA season with highest or lowest monthly averaged Kelvin filtered OLR variance in a 5° x 5° box centered at 7.5°N, 172.5°W. Kelvin OLR variance is contoured from 25 W^2 m^{-4} by 50 W^2 m^{-4}. Meridional wind variance is shaded at ±3 and 10 m^2 s^{-2}; dark shading represents positive values. Longest E-vectors are 40 m^2 s^{-2}; vectors are not plotted below 2 m^2 s^{-2}.

months during the JJA season with lowest variance. The composites are constrained to include months within the JJA period to remove any effects due to the seasonal cycle.

Shown in Figs. 3.9a and 3.9b are the high and low variance composites. Each plot includes anomalous Kelvin wave variance (contours), 200-hPa Kelvin wave filtered meridional wind variance (shading), and 200-hPa Kelvin wave filtered E-vectors. The

Kelvin wave filtered meridional wind variance and E-vectors were created by first filtering the daily 200-hPa zonal and meridional wind fields to the same wavenumber–frequency region as the Kelvin wave filtered OLR, as described in Section 3.3. This constrains the filtered disturbances to be eastward propagating with phase speeds of 8–30 m s^{-1}. The wind fields were filtered in this manner to limit them to the same spatial scales and phase speeds as the tropical Kelvin wave OLR signals, since variability on these time and space scales is dominant in the regressions. Monthly averaged fields were then calculated from the daily data. Finally, monthly anomalies were calculated by subtracting the average annual cycle at each gridpoint from the raw monthly data.

When monthly averaged Kelvin wave variance is anomalously high in the 5° x 5° box in the central Pacific, it is also anomalously high across the Pacific ITCZ, from 140°E to 80°W (Fig. 3.9a). Meridional wind variance at 200 hPa is anomalously high over Australia and to its east, in the same region as the climatological subtropical jet maximum in austral winter (see Fig. 3.1). This result illustrates that enhanced eastward-propagating wave activity within the subtropical jet is associated with enhanced Kelvin wave activity in the Pacific. These relationships are also observed in individual months (not shown). The composite E-vector anomalies give an indication of the change in the direction of energy propagation of the disturbances from the mean seasonal values (which are similar in direction to the <30 day filtered E-vectors shown in Fig. 3.1, but smaller in magnitude due to the additional constraints of the Kelvin wave filtering). In the region of enhanced meridonal wind variance, the E-vectors primarily point northeastward to

eastward, signaling the enhanced eastward propagation of disturbance energy in the Kelvin filtered band.

On the other hand, when monthly averaged Kelvin wave variance is anomalously low in the central Pacific, it is also anomalously low across the Pacific ITCZ (Fig. 3.9b). At the same time, meridional wind variance is decreased over Australia and to its west, signaling a decrease in eastward-propagating wave activity in the subtropical jet entering the region from the Indian Ocean. The anomalous E-vectors in this region of low meridional wind variance point southwestward, signaling that the disturbances which are present during these months have a group velocity with a smaller eastward component than the more typical disturbances in the jet.

These results, coupled with the regression results presented in Fig. 3.2, suggest that Kelvin wave activity in the central Pacific is sensitive to the amplitude and character of wave activity within the subtropical jet during austral winter. When disturbances in the jet are strong and move eastward with zonal phase speeds between 8–30 m s^{-1}, Kelvin wave activity in the Pacific is enhanced. A decrease in eastward-propagating wave activity in the subtropical jet is associated with reduced Kelvin wave activity in the tropical Pacific.

One might argue that the enhanced subtropical wind variance in the high variance composite (Fig. 3.9a) can be accounted for by circulations forced by the Kelvin wave OLR perturbations in the tropics, instead of the reverse, as is suggested above. While it is certainly the case that enhanced Kelvin wave activity in the tropics should lead to enhanced circulation variability in the subtropics, the regressions shown in Fig. 3.2 confirm that the circulation anomalies occur prior to the initiation of the convective

anomalies. In addition, the negative composite shows a decrease in wave activity to the west of the Kelvin wave OLR variance minimum, in the region in which the equatorward-propagating Rossby wave packets originate. This, again coupled with the regressions shown in Fig. 3.2, suggests that a decrease in extratropical wave activity over Australia leads to a decrease in Kelvin wave activity in the Pacific.

Plots of individual months (not shown) suggest that the magnitude of Kelvin wave activity in the central Pacific depends not only on the wave activity in the subtropical jet, but, as might be expected, also on the underlying thermal and moisture boundary conditions in the Pacific. When SSTs in the central Pacific are anomalously low, Kelvin wave activity is suppressed even when the subtropical jet is very active. On the other hand, Kelvin wave activity can be suppressed even when the thermal boundary conditions are favorable, as will be shown in the following section. These relationships suggest that an enhancement of Kelvin wave activity in the central Pacific depends on both warm SSTs and an influx of extratropical wave energy.

3.8 Case study: July 1986 vs. July 1987

The conclusions reached in the previous section can be illustrated even more dramatically by considering a case study. The months of July 1986 and July 1987 provide an interesting juxtaposition, and will be examined in this section.

In Fig. 3.10, monthly averaged maps of total SST (hatching), total Kelvin wave OLR variance (dark contours), anomalous 200-hPa Kelvin wave filtered meridional wind variance (shading), and total E-vectors are shown for a) July 1986 and b) July 1987. SST in the western and central Pacific is quite warm during both months, consistent with the

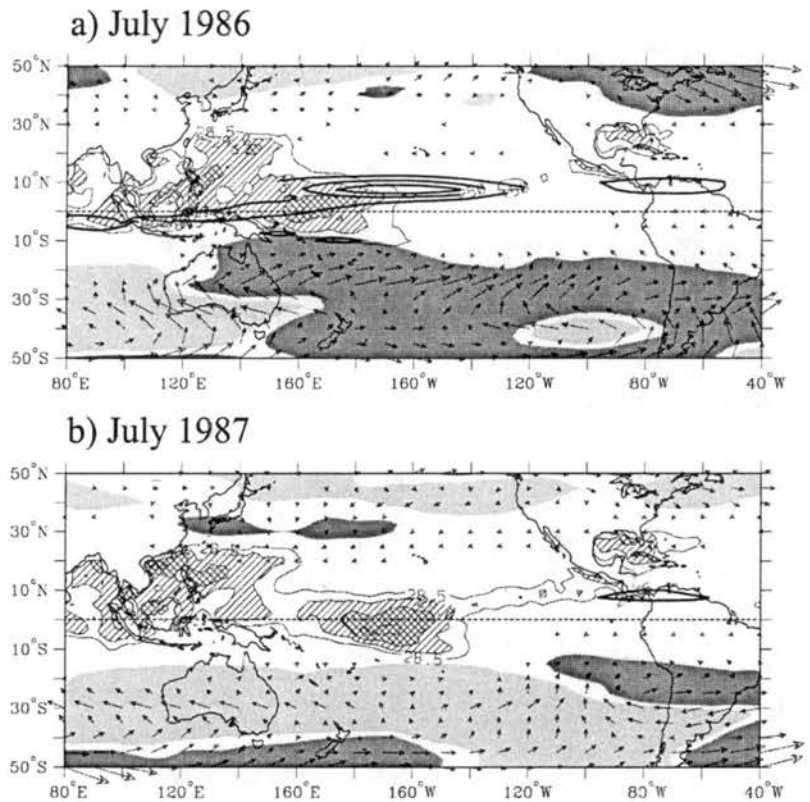


Figure 3.10: Monthly averaged total SST (hatching and light contours), Kelvin wave filtered OLR variance (dark contours), Kelvin wave filtered 200-hPa meridional wind variance anomalies (shading), total zonal wind (light contours), and Kelvin wave filtered 200-hPa total E-vectors, for (a) July 1986 and (b) July 1987. SST is contoured at 28°, 29°, and 29.5°C, with single hatching at 29°C and cross-hatching at 29.5°C. Kelvin OLR variance is contoured from 150 W^2 m^{-4} by 100 W^2 m^{-4}. Meridional wind variance anomalies are shaded at ±5 m^2 s^{-2}; dark shading denotes positive anomalies. Longest E-vectors are 150 m^2 s^{-2}, and are not plotted below 5 m^2 s^{-2}.

fact that both months fall within the 1986/87 warm El Niño–Southern Oscillation (ENSO) event. The warm event was in its initial stages in July 1986 and near its peak in July 1987, as measured by Niño 3.4 SST anomaly values of +0.33 and +1.78, respectively (see Trenberth 1997). Between 160°E and 140°W, SSTs are significantly warmer in July 1987 than in July 1986, with a distinct maximum in SST just south of the equator near the Dateline in July 1987. Total OLR variance follows this SST pattern, with higher variance in the central Pacific during July 1987 (not shown). Based on these

SST and OLR distributions alone, one might predict that Kelvin waves should be more active in the Pacific during July 1987 than during July 1986.

However, as shown by the dark contours in Figs. 3.10a and 3.10b, Kelvin wave activity is unusually intense during July 1986, and very weak during July 1987. The peak Kelvin wave variance in July 1986 exceeds 400 W^2 m^{-4}, while in July 1987, values maximize at 100 W^2 m^{-4}, a difference of a factor of 4. Consistent with the hypothesis that extratropical wave activity is associated with the initiation of Kelvin waves, the anomalous 200-hPa meridional wind variance distribution also shows substantial differences between July 1986 and July 1987. During July 1986 (Fig. 3.10a), meridional wind variance is anomalously strong eastward of 120°E, most notably in the region to the northeast of Australia, in the climatologically preferred region for equatorward-propagating wavetrains in austral winter. Total E-vectors point northeastward toward the tropics in this region. The 200-hPa jet core lies over southeastern Australia during July 1986, centered at approximately 150°E (not shown).

Contrast this situation with that in July 1987 (Fig 3.10b). The meridional wind variance is anomalously weak between the subtropical Indian Ocean and eastern Pacific, signifying a decrease in eastward-propagating subtropical wave activity in the jet region. The total E-vectors in this region point to the northwest. The jet core during July 1987 is located much farther to the east than during July 1986, centered at approximately 160°W (not shown), which is consistent with the eastward displacement of the local Hadley circulation during a warm ENSO event.

Daily maps of submonthly circulation anomalies for the months of July 1986 and July 1987 illustrate two quite different flow regimes (not shown), as might be expected

based on the difference in the 200-hPa meridional wind variance maps. During July 1986, wave packets flow freely to the east, often propagating northeastward over Australia as in Fig. 3.2. On the other hand, during July 1987, a blocking episode over Australia from 9–15 July disrupts the eastward propagation of waves. The difference between these two cases suggests the important role of fluctuations in the subtropical circulation on Kelvin wave variability in the tropics.

3.9 Summary and conclusions

A linear regression technique is used to determine the preferred circulation and convection patterns associated with the initiation and development of a convectively coupled Kelvin wave in the Pacific ITCZ during austral winter. A baroclinically developing wave packet in the Southern Hemisphere subtropical jet propagates eastward and equatorward over Australia, with a phase speed of approximately 15 m s^{-1}. The upper tropospheric divergence/convergence pair associated with the subtropical ridge and trough induces vertical motion anomalies that spread toward the tropics and acquire equatorially trapped, Kelvin wave-like characteristics. The zonal phase speed and wavelength of the developing Kelvin wave anomalies are similar to those in the extratropical perturbations, suggesting that the extratropical circulation anomalies are of the necessary spatial scale and frequency to excite a convectively coupled Kelvin wave. As the upper tropospheric vertical motion anomalies develop, a lower tropospheric pressure surge excited by the baroclinically-developing extratropical wavetrain also produces Kelvin-like temperature and height anomalies in the equatorial region. An easterly trade surge forms as mass flows from high to low pressure at the surface, causing

moisture convergence and upward motion in the lower troposphere ahead of the developing low OLR anomaly. The initiation of deep convection in the Kelvin wave appears to be due to a combination of the upper tropospheric vertical motion forced by the upper tropospheric Rossby wavetrain, and lower tropospheric moisture convergence and upward motion due to the extratropically generated pressure surge.

Once a convectively coupled Kelvin wave is established, it appears that it can be self-sustaining; that is, in many individual cases, eastward-propagating convective anomalies persist even after the initial subtropical circulation anomalies dissipate. This observation is consistent with the results of Lamb (1973), who suggested that equatorial waves may be initially excited by extratropical forcing, but that condensational heating provides the energy for the disturbances to continue propagating once they are excited. Primitive equation model simulations show that an eastward-propagating, Kelvin wave-like thermal forcing can induce a low-level convergence signal which propagates eastward out ahead of the forcing, further promoting the eastward propagation of convection and the Kelvin wave structure as a whole (M. Wheeler, personal communication). Furthermore, Haertel and Johnson (2000) show in a dry linear model that a moving thermal forcing creates a stronger gravity mode response in its direction of motion. Thus an eastward-propagating Kelvin wave thermal forcing should affect the boundary layer fields more strongly to its east, and through convergence and upward motion it may precondition the atmosphere for deep convection in this region. Mapes (2000) and Majda and Shefter (2001) suggest that convectively coupled Kelvin waves can be viewed as a result of "stratiform instability," which requires only two vertical modes: a deep convective heating and a stratiform heating over cooling. These studies

suggest that convectively coupled Kelvin waves, once initiated, may provide the necessary internal feedbacks to maintain their convective-dynamical structure as they propagate eastward.

On timescales longer than one individual wave, Kelvin wave variability in the Pacific is modulated by the strength of eastward-propagating extratropical wave activity in the subtropical jet. Increased Kelvin wave activity in the Pacific is associated with enhanced eastward-propagating wave activity in the jet, which typically propagates with a more equatorward group velocity than typical jet perturbations. Suppressed Kelvin wave activity, on the other hand, is associated with suppressed jet activity, and a weaker equatorward group velocity.

Two contrasting months during the 1986/87 warm ENSO event are compared, illustrating that Kelvin wave activity can be more strongly modulated by the strength of eastward-propagating subtropical wave activity than by changes in local SST. During July 1986, SSTs in the Pacific were marginally warm and extratropical wave activity was quite strong. Kelvin wave activity was anomalously strong during this time period. On the other hand, during July 1987, SSTs in the Pacific were very warm, but extratropical wave activity was weak. Kelvin wave activity during this period was suppressed. These two months provide an interesting comparison and support our theory that extratropical wave activity may be a precursor to Kelvin wave activity in the Pacific. An interesting sidenote to this case study is that while July 1987 was largely devoid of Kelvin wave activity in the Pacific, a strong convectively coupled mixed Rossby-gravity wave packet was observed in this region during this time (Dickinson and Molinari 2002). This observation suggests that the equatorial modes into which tropical convection is

organized may be dependent on the space-time characteristics of wave energy impinging on the tropical atmosphere from the extratropics.

4 THE OBSERVED STRUCTURE OF CONVECTIVELY COUPLED KELVIN WAVES: COMPARISON WITH SIMPLE MODELS OF COUPLED WAVE INSTABILITY

4.1 Introduction

Observations by Takayabu (1994), Wheeler and Kiladis (1999, hereafter WK99), and Wheeler et al. (2000, hereafter WKW00) demonstrate the existence of large-scale, zonally propagating variations in tropical cloudiness that are dynamically coupled to equatorially trapped wave structures in the troposphere and lower stratosphere. Space–time spectra of deep convective cloudiness data reveal spectral peaks which lie along the dispersion curves for the equatorially trapped shallow water waves discussed by Matsuno (1966), such as Kelvin, n = 1 Rossby, mixed Rossby-gravity, and inertio–gravity waves. The observed spectral peaks correspond to equatorial waves with small implied equivalent depths, typically 10–100 m, consistent with the fact that these convectively coupled, or moist, equatorial waves propagate at phase speeds much slower than their dry counterparts. For example, convectively coupled Kelvin waves are observed to propagate eastward at 15–20 m s^{-1}, whereas dry Kelvin waves in the lower stratosphere propagate eastward at 30–40 m s^{-1} (WKW00). Presumably, the reduction in

phase speed from dry to moist waves involves the interaction between tropical convection and the large-scale dynamical structure of the waves. The exact nature of this interaction, however, is not yet fully understood.

Several theories have been proposed to explain the existence of convectively coupled equatorial waves and the dynamics governing their behavior, including wave–CISK (Hayashi 1970; Lindzen 1974), WISHE (Wind-Induced Surface Heat Exchange; Emanuel 1987; Neelin et al. 1987), and more recently, stratiform instability (Mapes 2000; Majda and Shefter 2001). While all of these theories predict the existence of convectively coupled wave instabilities of some form, the true test of each theory lies in its ability to reproduce the *observed* structures of convectively coupled waves. However, there are few observational studies available presently with which to compare model results. An important step in improving our understanding of convectively coupled waves thus lies in an accurate observational diagnosis of the structures and phase relationships in these waves.

The present study provides detailed observations of one particular type of convectively coupled equatorial wave, the Kelvin wave. Convectively coupled Kelvin waves are perhaps the simplest form of an equatorially trapped wave, since their structure near the equator is essentially that of an eastward-propagating gravity wave. Observations of convectively coupled Kelvin waves may therefore provide a basis upon which theories of convectively coupled gravity waves, derived in relatively simple nonrotating two-dimensional frameworks, may be tested. Once a theory has successfully reproduced the observations in this simple case, it can be expanded to include rotation and other dynamical interactions. It may then become possible to understand the more

complex three-dimensional structures of convectively coupled Kelvin, mixed Rossby-gravity, and n = 1 Rossby waves, as well as the Madden-Julian Oscillation (MJO). The observed structures of convectively coupled Kelvin waves thus provide a simple test case through which the interaction between tropical deep convection and atmospheric wave circulations can initially be studied.

The observations presented in this study emphasize the tropospheric structure of convectively coupled Kelvin waves. The lower stratospheric structure of Kelvin and other equatorially trapped waves has been explained by WKW00 in terms of upward-propagating dry waves forced by a tropospheric heat source with a vertical structure similar to observations [see also Andrews et al. (1987)]. The tropospheric structure, on the other hand, is not as easily understood through these dry vertically propagating wave arguments. The approach taken here relies on "vertical mode" thinking rather than "vertically propagating wave" thinking, as has been similarly applied in observational and modeling studies such as Mapes (1993), Haertel and Johnson (1998), Mapes (2000) and Majda and Shefter (2001).

The remainder of this chapter is organized as follows. In Section 4.2, theories and models of convective coupling in equatorial waves are described in more detail. The datasets and methodology used in analyzing observed convectively coupled Kelvin waves in the present study are described in Section 4.3. In Section 4.4, the horizontal and vertical structures of Kelvin waves in the equatorial Pacific are presented, based on global reanalysis datasets, and are compared with radiosonde observations. Finally, in Section 4.5, a discussion of these observations in the context of the theories described in Section 4.2 is presented.

4.2 Theories of coupled wave instability

The interaction between deep convection and large-scale wave circulations in the tropical atmosphere has remained a subject of discussion for many years. At present, no theory is generally accepted as both 1) providing a complete conceptual picture of this interaction and 2) capable of reproducing observed features through numerical simulations based on such conceptualizations. Several proposed theories will be introduced and discussed in this section; in Section 4.5, these conceptual models will be compared with the observations of convectively coupled Kelvin waves to be presented in Section 4.4.

4.2.1 Wave–CISK

One of the first widely known theories describing the interaction between convection and the large-scale circulation in the tropics is CISK (Cooperative Interaction of the Second Kind). A broad interpretation of CISK theory states that instabilities in the large-scale circulation can be driven by the cooperative interaction between small-scale convective heating and the large-scale circulation [see Stevens et al. (1997) for other interpretations of CISK]. Namely, if deep convection is excited in a region of large-scale, low-level convergence, its associated latent heating will induce dynamical circulations that promote additional large-scale convergence (via a column-integrated warm anomaly), leading to more deep convection and further heating. When the initial large-scale convergence is supplied by a wave, the theory is known as wave–CISK (Hayashi 1970; Lindzen 1974). A schematic diagram of a first baroclinic Kelvin mode amplifying through the wave–CISK mechanism is presented in Fig. 4.1a. A positive

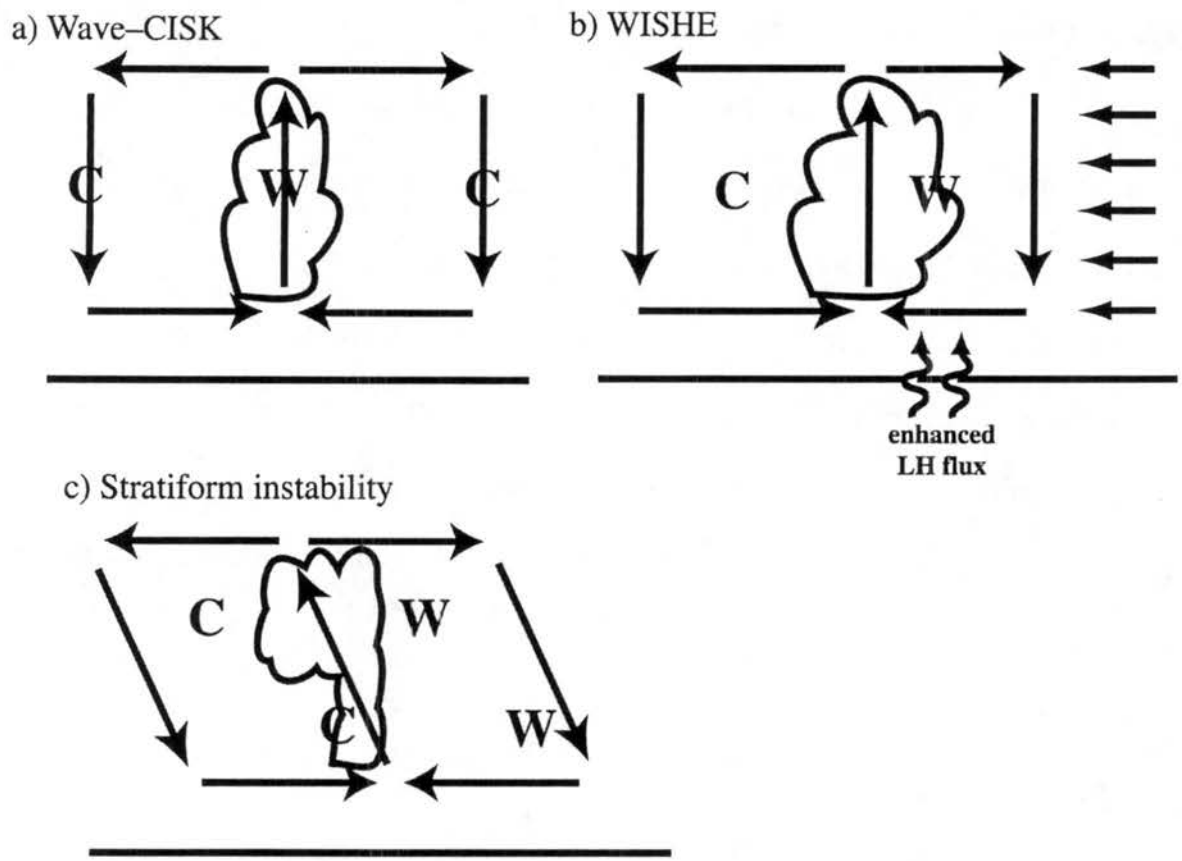


Figure 4.1: Schematic longitude–height diagrams illustrating the (a) wave–CISK, (b) WISHE, and (c) stratiform instability mechanisms of coupled wave instability. The wave–CISK and WISHE mechanisms in (a) and (b) are illustrated for a first baroclinic mode Kelvin wave. Vectors represent anomalous winds [except for vectors at right in (b), which represent easterly basic state winds], and cloud illustrations represent populations of cloud systems of the indicated type (convective or stratiform). W (C) represents warm (cold) anomalies. Upward arrows crossing the lower boundary represent surface fluxes.

correlation between latent heating (i.e., deep convection) and warm temperatures in the wave generates eddy available potential energy (EAPE), which induces wave growth. Observations of equatorial waves that display a positive correlation between heating and temperature are provided in studies such as Reed and Recker (1971), Stevens et al. (1997), Haertel and Johnson (1998), WKW00, and Yanai et al. (2000).

Although wave–CISK remains a reasonable conceptual picture of certain wave-like convection–circulation interactions in the tropics, modeling studies based on various wave–CISK parameterizations have not yet been able to avoid the "ultraviolet catastrophe," in which growth rates are largest on the smallest resolvable scales (Crum and Dunkerton 1992; Matthews and Lander 1999). Despite these numerical difficulties, modeled wave–CISK modes do provide simple structures with which to compare observations. Typically, the unstable modes produced in wave–CISK simulations have phase speeds between 15–30 m s^{-1}, which are too fast to account for the slow phase speed of the MJO, which propagates at 5–10 m s^{-1} (Madden and Julian 1994), but may be relevant to the convectively coupled Kelvin waves described in this study, which propagate eastward at 15–20 m s^{-1}. The structure of modeled Kelvin wave–CISK modes will be discussed in relation to observed Kelvin wave structures in Section 4.5.1.

The mechanism for the reduction in phase speed in wave–CISK-driven Kelvin waves involves an interaction between multiple vertical modes (Lau and Peng 1987; Chang and Lim 1988; Matthews and Lander 1999). A slower mode, with a higher vertical wavenumber, provides stronger boundary layer convergence and controls the speed of the wave. A faster, lower wavenumber mode dominates the vertical structure of the wave (Matthews and Lander 1999). Realistic convectively coupled Kelvin wave phase speeds are produced when heating maximizes in the upper troposphere, as observed.

4.2.2 WISHE

An alternative theory to explain the existence of convectively coupled waves is WISHE (Wind-Induced Surface Heat Exchange, or air-sea interaction; Emanuel 1987; Neelin et al. 1987). The application of WISHE theory to equatorial waves was introduced in the context of quasi-equilibrium (QE) theory (Arakawa and Schubert 1974). The QE closure implies that the convective available potential energy (CAPE) generated by adiabatic cooling and low-level moisture convergence in the rising branch of a large-scale wave circulation will be quickly consumed by convection, such that the cooling is nearly balanced by latent heating (Emanuel et al. 1994). Observations generally support QE theory, since the actual temperature changes associated with strong upward motion and large convective heating rates in equatorial waves are very small compared to the values that might be expected if convection were not present (Stevens et al. 1997).

A strict interpretation of QE theory states that convective heating will be exactly in phase with large-scale upward motion in an equatorial wave (Emanuel et al. 1994). A first baroclinic mode Kelvin wave propagating eastward in a strict QE system will display temperature and heating fields that are exactly in quadrature, with warm temperatures leading the upward motion and convective heating by a quarter cycle. In this system, moist unstable waves cannot grow through the interaction between convection and circulation alone, since the temperature and heating fields are always in quadrature. Emanuel et al. (1994) argue that large-scale coupled waves can thus only be neutral (i.e., neither amplifying nor decaying), or "moist convectively damped," if convection slightly lags vertical motion and the heating is shifted toward the cold temperature anomaly.

WISHE theory provides a mechanism by which amplifying convectively coupled wave modes can be generated in the strict QE system, by incorporating the effects of surface heat fluxes.[3] The role of convection in WISHE is not to act as a heat source, as in wave–CISK, but instead to rapidly redistribute boundary layer temperature changes throughout the vertical column. Boundary layer temperature fluctuations can be induced either by convection itself, in the form of convective downdrafts, or by interactions with the surface, through wind speed-dependent latent heat fluxes from the ocean (Emanuel et al. 1994). A first baroclinic mode Kelvin wave can thus amplify in the WISHE system in the presence of mean surface easterly winds, since the surface fluxes will be larger ahead of the rising branch of the wave (Fig. 4.1b). Convection will redistribute this surface warming throughout the troposphere, such that heating will be shifted into the warm phase of the wave, generating EAPE through the positive correlation between heating and temperature.

A weakness in WISHE theory is its assumption of nonzero basic state winds, specifically basic state easterlies for the case of eastward-propagating waves such as Kelvin waves and the MJO. Although surface winds in the tropics are generally easterly over the Pacific, monsoon westerlies exist in the Indian Ocean region during both austral and boreal summer, and can extend eastward into the Pacific during strong El Niño/Southern Oscillation (ENSO) events. WISHE theory cannot explain the intensification of eastward-propagating waves during periods of surface westerlies, or at times when the total surface fluxes are stronger to the west of the convection rather than

[3] The WISHE mechanism is discussed here only in terms of its ability to promote wave amplification, and is not suggested to influence the direction of propagation of the wave itself. It is assumed that the direction of propagation of a coupled wave can be explained by equatorial wave dynamics alone.

to its east. Examples of such instances were observed during the TOGA COARE period, when an MJO propagated eastward in the western Pacific during a period of basic state surface westerlies, and surface fluxes were strongest to the west of the deepest convection (Lin and Johnson 1996).

The reduced phase speed of WISHE modes, as compared to the dry speeds of uncoupled modes, is attributed to a reduction in static stability throughout the convecting column (Emanuel et al. 1994). Negative temperature fluctuations in the boundary layer induced by convective downdrafts are redistributed throughout the column such that the greatest cooling occurs at upper levels, thus reducing the static stability of the column. The "effective" static stability is argued by Emanuel et al. (1994) to be approximately one-tenth the value of the dry static stability.

4.2.3 Stratiform instability

The increase in direct observations of tropical convection in recent years has led to new ideas about how convection is triggered, how it is organized on the mesoscale, and how these mesoscale features evolve in time. Observations by Rickenbach and Rutledge (1998) suggest that approximately 80% of rainfall in some tropical regions may be associated with organized, mesoscale precipitation regions, of which 30–40% falls as stratiform precipitation. Such observations suggest the important role of stratiform precipitation in the large-scale moisture, momentum, and thermodynamic budgets of the tropical atmosphere. Stratiform regions are generally more horizontally extensive than the convective regions that precede them; they also persist for long time periods after

convection has dissipated, and thus may have a large impact on the potential for subsequent convective outbreaks.

Two recent studies, by Mapes (2000) and Majda and Shefter (2001), propose that the effects of stratiform precipitation are essential to the existence and structure of convectively coupled gravity or Kelvin waves. A "stratiform instability" mechanism of coupled wave instability is developed in the context of dynamically simple models that include only two vertical modes: a first baroclinic "convective" mode, and a second baroclinic "stratiform" mode.

The stratiform instability mode is generated through a positive correlation between a second mode temperature wave and the second mode stratiform heating profile. In the Mapes (2000) formulation, large-scale convectively coupled gravity waves organize from initial random noise when fluctuations in the convective inhibition (CIN) are parameterized to be dominant over fluctuations in CAPE. The second mode instability is activated when deep convection is triggered by a reduction in CIN, via a second mode warm over cold temperature anomaly, and is followed at lag by a stratiform (second mode) heating over cooling profile. The lower tropospheric cooling then further decreases CIN, which reinitializes deep convection, leading to further stratiform heating and a positive correlation between the second mode heating and temperature profiles. Fig. 4.1c illustrates the phase relationships between convective and stratiform heating and temperature for the stratiform instability mechanism of wave amplification. Circulation and temperature anomalies tilt westward with height, and temperature anomalies have a strong second baroclinic mode structure. No basic state winds are required for this mode to exist.

Stratiform instability waves propagate at phase speeds near the dry wave speed of the second internal mode. The reduction in phase speed in stratiform waves is attributed to the effects of the second vertical mode, as in wave–CISK, rather than the effect of moisture on the first vertical mode, as in WISHE (Mapes 2000).

4.3 Data and methodology

The observed relationships between tropical convection and the kinematic, thermodynamic, and moisture fields in convectively coupled Kelvin waves will be presented in Section 4.4. These relationships are analyzed through the use of a linear regression technique applied to many years of data, as in previous studies (WK99; WKW00; Straub and Kiladis 2002a, hereafter SK02a; Straub and Kiladis 2002b, hereafter SK02b). Deep tropical convection associated with convectively coupled Kelvin waves is isolated using a filtered version of the 2.5° resolution NOAA outgoing longwave radiation (OLR) dataset (Liebmann and Smith 1996). As described thoroughly in WK99 and WKW00, OLR fluctuations associated with convectively coupled Kelvin waves are separated from the raw OLR data by filtering the data in wavenumber–frequency space such that only fluctuations in the region of the climatological Kelvin wave OLR spectral peak are retained. The Kelvin wave filter retains OLR variability with periods between 2.5 and 17 days, and eastward phase speeds of 8–30 m s^{-1} (see Fig. 2.1). As in SK02a and SK02b, both symmetric and antisymmetric components of OLR with respect to the equator are allowed to pass through the filter. Data have been averaged to daily temporal resolution from twice-daily resolution.

European Centre for Medium-Range Weather Forecasts (ECMWF) reanalysis data are used to represent the global atmospheric circulation. The reanalysis data are available on the same 2.5° grid as the OLR data, at 16 pressure levels between 1000 and 10 hPa, for the years 1979–1993. Data are averaged to daily resolution from four-times daily resolution. Temperature, horizontal wind, vertical motion, geopotential height, and specific humidity data at all grid points are linearly regressed at lag against the Kelvin wave filtered OLR extracted at specific grid points of interest. The resulting regressed fields are then scaled to a -30 W m^{-2} anomaly in Kelvin wave OLR, which represents a moderate Kelvin wave event.

Composites have also been calculated based on both negative and positive OLR perturbations at the same base points as used in the linear regressions. The composite results are very similar to those calculated in the regressions, for both positive and negative OLR anomalies, suggesting a strong linearity in the Kelvin wave dynamical fields and justifying the use of the linear regression technique.

Radiosonde data from the National Climatic Data Center's (NCDC) Comprehensive Aerological Reference Data Set (CARDS) are also utilized in this study, to provide a validation of the reanalysis-based results. Data were extracted at either 15 mandatory levels or 29 mandatory and significant levels, depending on data resolution. The data have been averaged to daily temporal resolution, and extend from 1979–1999. The radiosonde data are subjected to the same linear regression procedure as the reanalysis data, based on the Kelvin wave filtered OLR at the nearest grid point to each radiosonde station, for the period 1979–1999.

4.4 Observed Kelvin wave structure

The Kelvin wave observations presented in this section are based on regressions of ECMWF reanalysis data and total OLR against the Kelvin wave filtered OLR at the point 7.5°N, 187.5°E, in the central Pacific. This base point is the location of the maximum climatological Kelvin wave OLR variance during the boreal summer season (June–July–August, or JJA), as illustrated in Figs. 2.2 and 3.1, and lies along the axis of the boreal summer climatological intertropical convergence zone (ITCZ). The regressions are calculated over the 15 JJA periods from 1979–1993. The results can thus be considered to be typical of Kelvin waves in the central Pacific during boreal summer. In Section 4.4.4, the reanalysis regressions are compared with regressions based on radiosonde data from Majuro, Marshall Islands, in the central Pacific.

Reanalysis- and radiosonde-based regressions have also been calculated for base points over equatorial Africa during boreal spring (MAM) and in the Indian Ocean region during JJA, both of which represent local Kelvin wave OLR variance maxima. The results for Kelvin waves over Africa and the Indian Ocean are not presented here, however, as the structures are similar to those in the central Pacific. The boreal summer central Pacific case is presented here because 1) the annual maximum in Kelvin wave activity occurs in this location and at this time of year, and 2) the open ocean location of the central Pacific eliminates complications due to land effects. Kelvin waves propagating over Africa appear to be disrupted by the elevated topography of eastern Africa, and in the Indian Ocean region, waves tend to dissipate when they reach the Maritime Continent.

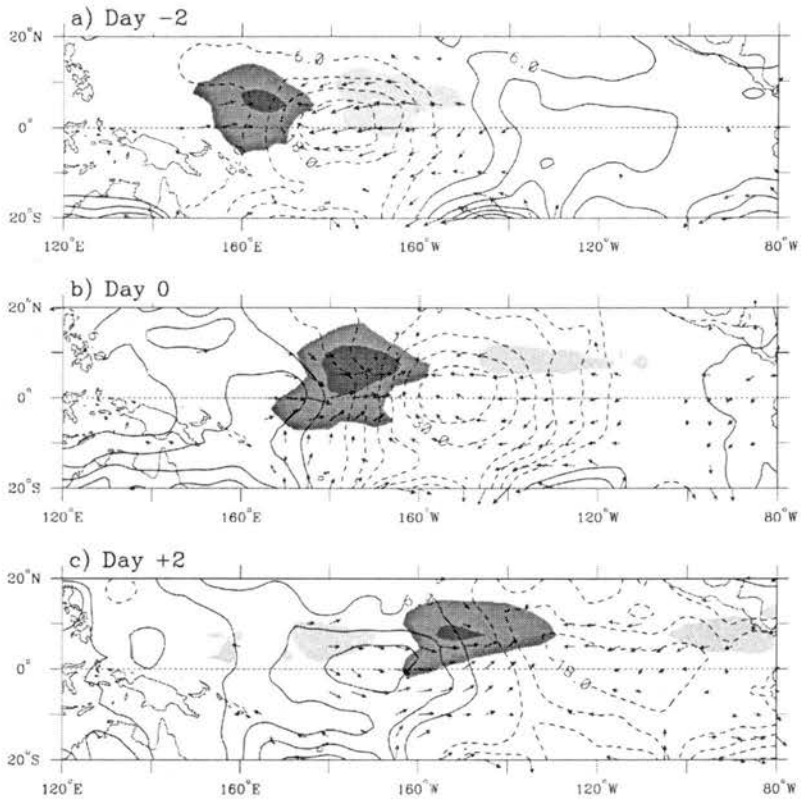


Figure 4.2: Regressed OLR (shading) and ECMWF reanalysis 1000-hPa geopotential height (contours) and winds (vectors) for days (a) –2, (b) 0, and (c) +2, based on a –30 W m^{-2} anomaly in Kelvin wave filtered OLR on day 0 at the base point 7.5°N, 187.5°E. Wind vectors are plotted only where significant at the 95% level or greater.

4.4.1 Horizontal structure

Figure 4.2 illustrates the regressed horizontal structure of OLR (shading) and reanalysis 1000-hPa geopotential height (contours) and winds (vectors) for a Kelvin wave in the central Pacific, on days –2, 0, and +2. The OLR anomalies move eastward at approximately 17 m s^{-1}, maximizing to the north of the equator at the latitude of the climatological ITCZ, where sea surface temperatures (SSTs) maximize during boreal summer (SK02b). Easterlies exist to the east of the low OLR signal, while westerlies exist both in-phase with the low OLR and to its west. Low (high) geopotential height anomalies maximize to the east (west) of the lowest OLR, and are symmetric with respect

to the equator throughout the life cycle of the Kelvin wave. As discussed in SK02b, the observed Kelvin wave dynamical fields throughout the troposphere and lower stratosphere are primarily symmetric with respect to the equator, even though the OLR signal maximizes in the Northern Hemisphere in the central and eastern Pacific. The phasing of OLR, wind, and height anomalies shown in Fig. 4.2 for the central Pacific Kelvin wave is similar to that for Kelvin waves over Africa during MAM and in the Indian Ocean during JJA (not shown). In these other locations, however, the OLR signal maximizes on the equator instead of in the Northern Hemisphere, due to the fact that the lower boundary conditions are more symmetric with respect to the equator.

The eastward-propagating region of low OLR in Fig. 4.2 represents an envelope of enhanced deep cloudiness, which was shown by SK02b to consist primarily of smaller spatial scale, shorter time scale convective activity. Much of this activity is organized into westward-propagating mesoscale systems of horizontal scale 100–500 km, which include both convective and stratiform precipitation regions. It is important to recognize that the large-scale dynamical structures illustrated in this study represent the net effect of these numerous smaller-scale events that occur within the eastward-propagating cloudiness envelope.

The maximum convergence of 1000-hPa wind anomalies lies to the east of the low OLR anomaly, as might be inferred from the wind vectors on day 0 in Fig. 4.2. Fig. 4.3a quantitatively illustrates this relationship throughout the wave's lifetime in a time–longitude diagram of regressed OLR (shading) and 1000-hPa divergence (contours),

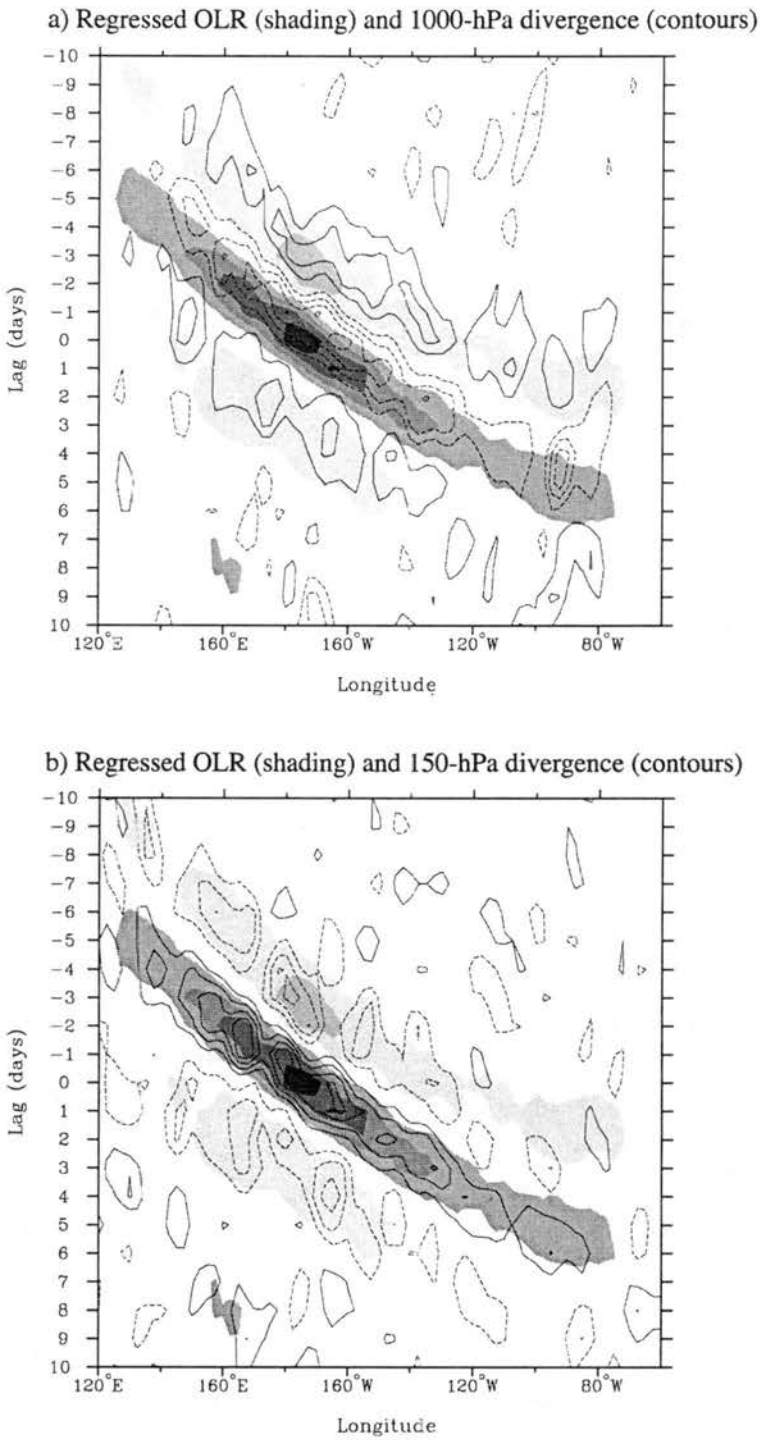


Figure 4.3: Time–longitude diagram of regressed OLR (shading at ±5 W m^{-2} intervals, dark negative) and divergence (contours, solid positive, zero contour omitted) at (a) 1000 hPa (contour interval 0.2 x 10^{-6} s^{-1}), and (b) 150 hPa (contour interval 0.4 x 10^{-6} s^{-1}). All fields have been averaged from 0°–10°N.

from day –10 to day +10. Both fields have been averaged from 0–10°N.[4] Maximum 1000-hPa convergence precedes the lowest OLR anomalies by approximately 10–15° of longitude, or approximately one-eighth of a cycle, based on a zonal wavelength of 80°.

The maximum upper tropospheric divergence in the Kelvin wave is located at approximately 150 hPa, and is collocated with low OLR, as shown in Fig. 4.3b. Figures 4.3a and 4.3b suggest the presence of a tilted structure in the vertical, with maximum lower tropospheric convergence located ahead of the maximum deep convection, and upper tropospheric divergence collocated with the low OLR itself. As will be shown in the following section, the 1000-hPa convergence anomaly illustrated in Fig. 4.3a is in phase with low-level moist, rising air, suggesting a buildup of shallow convection preceding deep convection in the wave.

4.4.2 Vertical structure

The vertical structure of temperature and winds associated with the Kelvin wave on day 0 is shown in Fig. 4.4a, a longitude–height cross-section along 7.5°N. OLR perturbations maximize at 7.5°N on day 0, and thus the dynamical anomalies should be most directly coupled to the convection at this latitude. Although the reanalysis temperature and vertical motion fields are highly constrained by the model's convective parameterization scheme, and thus may be not be regarded with as much confidence as the wind fields, comparisons with radiosonde data in Section 4.4.4 show that the large-scale temperature structures are actually quite similar.

---

[4] The results are similar for the latitude band from 5°S–5°N, except that in this case, the OLR signal appears to weaken over the eastern Pacific. This is because the convection associated with the Kelvin wave propagates along the latitude of the ITCZ, which shifts northward from the equator in the western Pacific to 5°–10°N in the eastern Pacific.

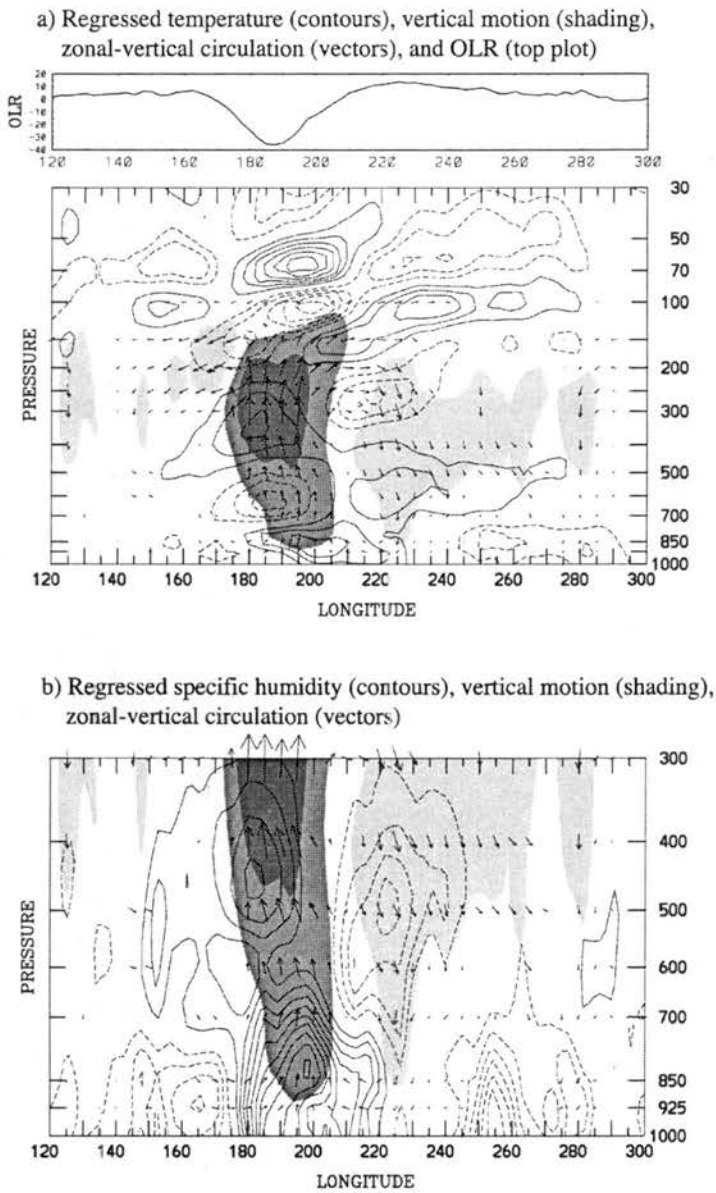


Figure 4.4: (a) Longitude–height cross-section along 7.5°N of regressed temperature (contours, interval 0.075 K), vertical motion (shading, at 0.15 and 0.5 cm s^{-1}), and zonal–vertical circulation (vectors). OLR cross-section at 7.5°N is shown in upper plot. The vertical component of the vectors has been multiplied by 700 to account for the small aspect ratio of the plot. The longest vectors represent winds of 5.0 m s^{-1}. (b) Same as (a) except for specific humidity (contours, interval 0.05 g kg^{-1}) shown only to 300 hPa.

Figure 4.4a illustrates the regressed ECMWF temperature (contours), vertical motion (shading), and zonal–vertical circulation (vectors), as well as the regressed OLR (top panel), along 7.5°N on day 0. The strongest vertical motion anomalies are found in

the upper troposphere between 180°–200°E, and are collocated with the lowest OLR. These large-scale, low-amplitude (order mm s^{-1}) vertical motion anomalies represent an average over the numerous smaller-scale, higher amplitude convective updrafts within the eastward-propagating envelope of convection. Downward motion anomalies are weaker, more horizontally extensive, and are located primarily to the east of the low OLR on day 0. The zonal component of the low-level convergence and upper-level divergence signals in Figs. 4.3a and 4.3b can be seen in the vector winds of Fig. 4.4a, with low-level convergence and upward motion leading the low OLR and upper tropospheric upward motion by approximately 15° of longitude. Upper tropospheric divergence is located directly above the maximum upward motion. Outflow between 100 and 200 hPa spreads both east and west in the upper troposphere, but the sinking motion that completes the zonal–vertical circulation cell is stronger to the east at this time. At later lags, the western cell becomes the stronger of the two.

The tropospheric temperature anomalies project strongly onto a second baroclinic mode structure, with warm over cold anomalies in the region of large-scale upward motion and low OLR, and cold over warm anomalies to the east. The existence of a second baroclinic mode temperature structure in the troposphere, with a node at approximately 500 hPa, suggests that stratiform precipitation processes play a role in determining the large-scale wave structure. It is well known that regions of stratiform precipitation are marked by an overall signature of latent heating and rising motion above 500 hPa, and evaporative cooling and sinking motion below 500 hPa (Houze 1997). In a case study of a convectively coupled Kelvin wave presented in SK02b, stratiform

precipitation is shown to comprise greater than 50% of the total precipitating echo area throughout the wave's passage.

The observed tropospheric temperature structure in Fig. 4.4a is not purely second mode, however. Additional low-level temperature perturbations exist between approximately 750 hPa and 1000 hPa. Warm low-level air slightly leads low-level convergence and upward motion anomalies (Fig. 4.4a), as well as positive specific humidity perturbations (Fig. 4.4b). Throughout the evolution of the wave, an in-phase relationship persists between temperature, moisture, upward motion, and convergence anomalies in the 850–1000 hPa layer (not shown). These signals suggest the presence of enhanced shallow convection to the east of deep convection. The upward transport of moisture due to deep convection can be detected in the upper tropospheric moist anomalies between 300 and 600 hPa in Fig. 4.4b, which lag the strongest upper tropospheric upward motion anomalies and low OLR.

The case study of a Kelvin wave in the eastern Pacific by SK02b is consistent with the idea that on the large scale, shallow convection tends to precede deep convection and stratiform precipitation in the Kelvin wave as it propagates eastward. As viewed from the NOAA ship *Ronald H. Brown*, which was stationed in the eastern Pacific ITCZ during a Kelvin wave passage, an overall progression of shallow convection to deep convection to stratiform precipitation was observed over a period of 2 days. The same wave viewed in high-resolution satellite imagery showed that the large-scale convective envelope consisted of smaller-scale, westward-propagating cloud clusters. The envelope of cloudiness moved eastward in time as new convection was initiated to the east of the existing convective envelope, intensifying and developing stratiform regions as it moved

westward within the envelope. In the western portion of the envelope, stratiform precipitation was dominant. In this manner, the large-scale temperature and moisture fields averaged over many Kelvin wave events can show systematic signals representative of the effects of shallow convection to the east of the deepest convection, and stratiform precipitation to the west. The tropospheric temperature, wind, and moisture anomalies detected in radiosonde data from the *Ronald H. Brown* (Figs. 2.10a, 2.11a, and 2.14a) are also consistent with the regressed reanalysis fields presented in Figs. 4.3 and 4.4. Warm lower tropospheric temperatures precede convection, while a warm-over-cold second vertical mode structure was observed during the deepest convection and thereafter. Moisture anomalies were strong and positive below 700 hPa prior to the lowest OLR, and from 700 to 300 hPa afterward.

4.4.3 Phase relationships between temperature and vertical motion

The temperature anomalies in the layer between approximately 200–500 hPa are highly correlated with vertical motion anomalies throughout the wave's life cycle. Shown in Fig. 4.5a is a time–longitude diagram of regressed 300-hPa vertical motion (shading) and temperature (contours), averaged from 0°–10°N. These two fields are also highly correlated with OLR and 150-hPa vertical motion (compare with Fig. 4.3b), such that upper tropospheric warm anomalies, upward vertical motion, 150-hPa divergence, and low OLR are all spatially and temporally phase-locked. These relationships suggest a generation of EAPE by the Kelvin wave, through the positive correlation between temperature and heating (as inferred by low OLR). The correlation between heating, upward motion, and 150-hPa divergence suggests the conversion of EAPE to eddy

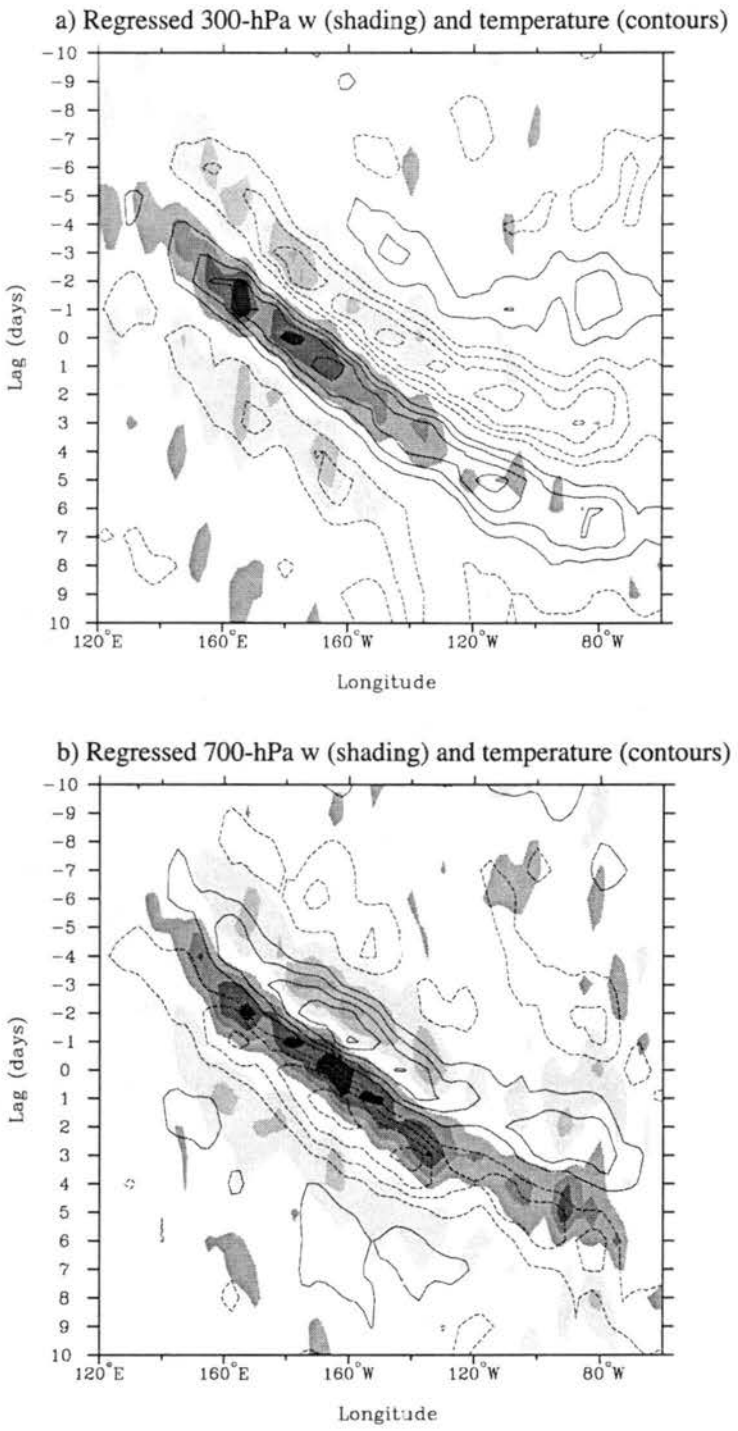


Figure 4.5: Time–longitude diagram of vertical motion (shading, dark negative) and temperature (contours, solid positive, contour interval 0.05 K, zero contour omitted), averaged from 0°–10°N, at (a) 300 hPa, and (b) 700 hPa. Shading in (a) is at ±0.15 cm s^{-1} intervals and in (b) is at ±0.05 cm s^{-1} intervals.

kinetic energy (EKE). Similar temperature structures and phase relationships with respect to heating and OLR are shown by Haertel and Johnson (1998) for 2-day waves in the Pacific.

In the lower troposphere, between about 500 and 850 hPa, temperature and vertical motion anomalies in the Kelvin wave exhibit a near quadrature relationship, quite different from the in-phase relationship in the upper troposphere. As shown in Fig. 4.5b, downward motion anomalies at 700 hPa (light shading) lead warm temperatures (solid contours), which lead upward motion (dark shading) and cold temperatures (dashed contours). The near quadrature relationship of temperature and vertical motion in the lower troposphere suggests the presence of either 1) free (unforced or uncoupled) Kelvin wave-like circulations or 2) coupled circulations obeying strict QE, as discussed in Section 4.2.2. Evidence of this quadrature relationship between temperature and vertical motion in cross-sections similar to Fig. 4.4a becomes more pronounced at latitudes farther removed from the strongest deep convective signal, for example, on the equator on day 0 (not shown), suggesting a dry Kelvin wave circulation. In the immediate vicinity of the deepest convection, on the other hand, there is a stronger out-of-phase relationship between temperature and vertical motion, such that upward (downward) motion anomalies at 700 hPa are correlated with cold (warm) temperatures (Fig. 4.4a). When a latitudinal average is constructed as in Fig. 4.5b, upward (downward) motion appears to lead cold (warm) temperatures by slightly less than a quarter cycle.

4.4.4 Radiosonde comparisons

A similar regression technique was applied to radiosonde data from Majuro, Marshall Islands (7.1°N, 171.4°E), to determine the local temperature, humidity, and wind changes associated with the passage of a Kelvin wave OLR signal. Figures 4.6a–d show the regressed OLR, temperature, specific humidity, and zonal wind anomalies associated with a –30 W m^{-2} anomaly in Kelvin wave filtered OLR at the closest grid point to Majuro (7.5°N, 172.5°E) on day 0. A primarily second baroclinic mode temperature structure can be seen in the troposphere (Fig. 4.6b), as in the reanalysis regressions, with a strong warm anomaly in the upper troposphere peaking on day 0, coincident with the lowest OLR. A warm anomaly in the lower troposphere, centered at 700 hPa, precedes the low OLR, maximizing between days –2 and –1, while a lower tropospheric cold anomaly follows the low OLR, with a peak between days +1 and +2. These signals extend down to the surface with no apparent change in phase, in contrast to the reanalysis data in Fig. 4.4a, where surface temperature anomalies lag the lower tropospheric anomalies. The difference in the structure of the lower tropospheric temperature anomalies between the reanalysis and radiosonde regressions suggests that the shallow convective heating in the reanalysis may be too strong. Since the ECMWF reanalysis convective parameterization includes separate schemes for shallow and deep convective heating, these results suggest that the partitioning of energy between the two schemes may not be accurate for Kelvin waves (A. Tompkins, personal communication). Overall, however, the ECMWF reanalysis does appear to quite successfully resolve the vertical temperature structure of convectively coupled Kelvin waves.

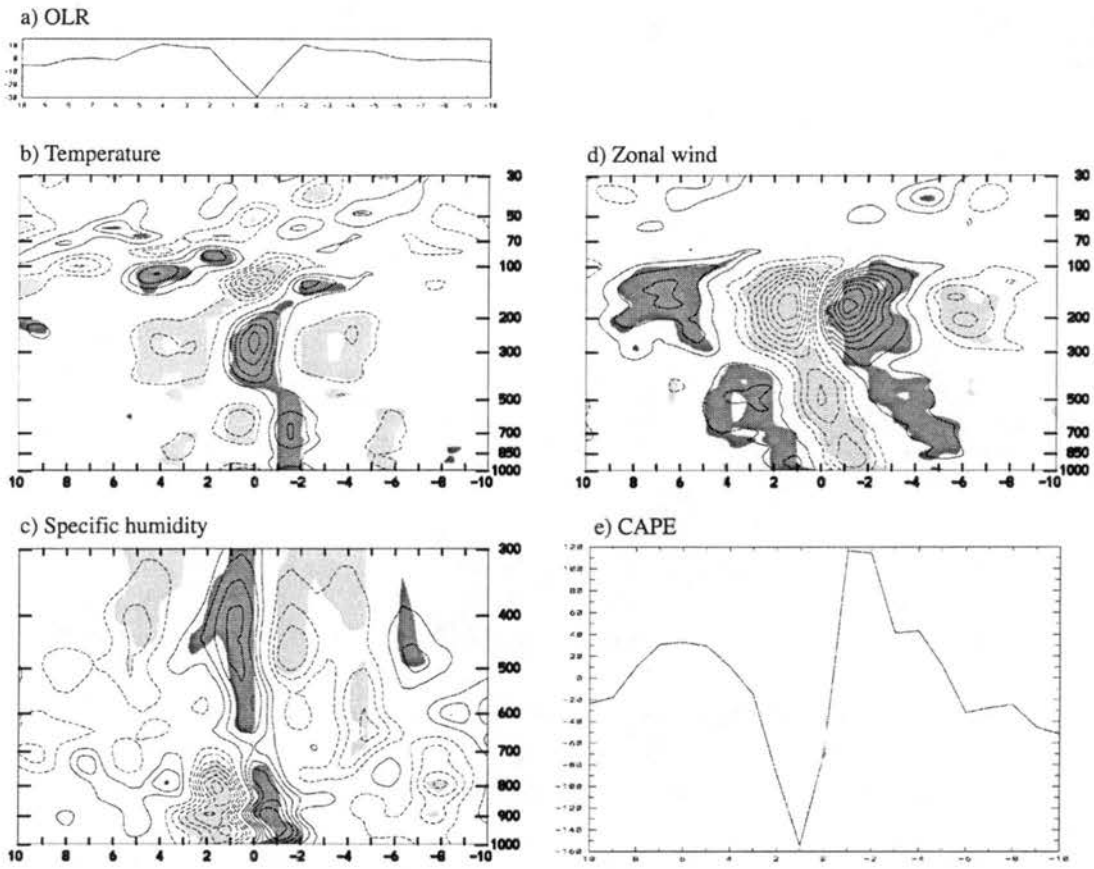


Figure 4.6: Regressed (a) OLR, time–height plots of radiosonde (b) temperature (contour interval 0.1 K), (c) specific humidity (contour interval 0.05 g kg^{-1}; shown only to 300 hPa), and (d) zonal wind (contour interval 0.25 m s^{-1}), and time evolution of (e) CAPE at Majuro (7.1°N, 171.4°E), based on a –30 W m^{-2} anomaly in Kelvin filtered OLR at the closest grid point (7.5°N, 172.5°E) on day 0. Time progresses from right to left, so that time–height structures in (b) and (c) can be compared with longitude–height structures in Figs. 4.4a and 4.4b. Twenty-seven levels of data are represented in (b) and (d), and 15 levels in (c). Shading represents regions of statistical significance at the 95% level or greater, with dark shading representing positive correlations.

Evidence of the effects of shallow convection, deep convection, and stratiform precipitation can be seen in the time–height diagram of regressed specific humidity at Majuro, in Fig. 4.6c. Prior to the lowest OLR on day 0, there is a rapid increase in lower tropospheric moisture, with moist anomalies maximizing between approximately 850 and 950 hPa on day –1. The significant depth of the moisture increase, to 700 hPa, suggests that shallow convection plays a role in transporting moisture upward. On day 0, when

deep convection occurs at Majuro, positive specific humidity anomalies extend through the troposphere to 300 hPa, suggesting the vertical transport of moisture by deep convection. There is an abrupt change from moist to dry air below 700 hPa on day 0, while moist anomalies linger in the upper troposphere for several more days. The moist over dry anomalies observed on days +1 and +2 suggest the presence of both deep convection and stratiform precipitation. The radiosonde humidity signals in Fig. 4.6c are consistent with those in the reanalysis regressions in Fig. 4.4b, where enhanced lower tropospheric moisture exists to the east of the low OLR and enhanced upper tropospheric moisture maximizes between 400–500 hPa to the west of the low OLR.

Figure 4.6d shows the regressed zonal wind anomalies at Majuro. Surface easterlies precede the deep convection, maximizing between days –2 and –1, and westerlies follow, maximizing on day +1. The magnitude of the easterlies preceding deep convection is larger than the magnitude of the westerlies following it, suggesting a stronger latent heat flux from the ocean ahead of the deep convection, especially since the basic state winds are easterly in this region. Surface zonal wind convergence can be estimated from the zonal wind gradient to be strongest between days –1 and 0, peaking before the lowest OLR signal as in the reanalysis regression in Fig. 4.3a. Between 300 and 100 hPa, strong westerly anomalies change over to easterly anomalies on day 0, signaling a maximum in divergent outflow occurring in phase with deep convection in the Kelvin wave, in a similar manner to the reanalysis regression in Fig. 4.3b.

The regressed CAPE anomalies at Majuro are shown in Fig. 4.6e. The mean CAPE at Majuro for the 21-year JJA period is 2154 J kg^{-1}. CAPE peaks on days –2 and –1, when the surface air is anomalously warm and moist and the upper troposphere is

cool. A sharp decline in CAPE occurs between days –1 and +1, during the time of enhanced deep convection, suggesting that convection itself reduces the CAPE. The lower tropospheric cooling and drying and the upper tropospheric warming and moistening observed in Figs. 4.6b and 4.6c after day 0 are consistent with the effects of deep convection and stratiform precipitation on the large-scale temperature structure of the atmosphere, which act to reduce CAPE.

The CAPE anomalies shown in Fig. 4.6e are small compared to the mean values at Majuro, suggesting that the atmosphere remains close to QE. The small increase in CAPE, which was presumably forced by the large-scale circulation (i.e., the anomalies causing the increase in CAPE are consistent with the structure of a large-scale Kelvin wave), is subsequently consumed by convection over a 2-day period. Anomalously high CAPE precedes enhanced convection by 1–2 days, allowing for a positive correlation between warm upper tropospheric temperatures and latent heating, which generates EAPE and allows the wave to grow.

The regressed temperature, moisture, wind, and CAPE anomalies at Majuro are similar to regressions using radiosonde data at other tropical stations (and the corresponding Kelvin filtered OLR at the nearest grid point to each station), such as Tarawa (central Pacific), Truk (western Pacific), Balboa (Central America), Bangui-Mpoko (Africa), and Singapore (eastern Indian Ocean). The similarities between these station data suggest that the Kelvin wave structures illustrated for Majuro are robust, and that the vertical structures and phase relationships in Kelvin waves are not strongly affected by differences in the basic state.

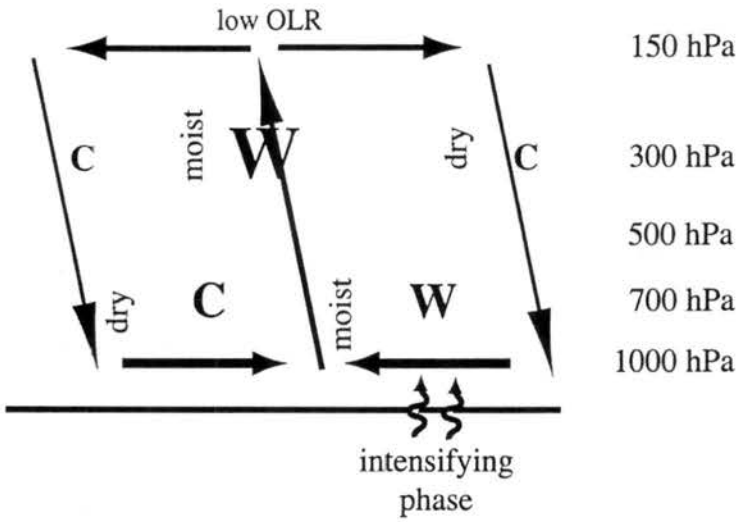


Figure 4.7: Schematic diagram of observed convectively coupled Kelvin wave structure. W (C) represents warm (cold) anomalies. Width of arrows and size of text denotes relative strength of anomalies. Upward arrows crossing the lower boundary represent surface fluxes.

4.4.5 Summary

Presented in Fig. 4.7 is a schematic diagram illustrating the phase relationships in the zonal–vertical plane in observed convectively coupled Kelvin waves. Circulation cells tilt westward with height, such that surface convergence leads upper tropospheric upward motion by approximately an eighth of a cycle. Surface convergence is in phase with lower tropospheric upward motion anomalies, and slightly lags lower tropospheric warm temperature and enhanced moisture anomalies. Upper tropospheric upward motion lags that in the lower troposphere, and is in phase with low OLR, warm temperatures, and upper tropospheric divergence. Upper tropospheric moisture anomalies lag vertical motion anomalies by about an eighth of a cycle. The observed tropospheric temperature structure projects primarily onto the second baroclinic mode, with a node at 500 hPa. In the lower troposphere, temperature and vertical motion anomalies are in quadrature, while in the upper troposphere, temperature and vertical motion anomalies are in phase.

The implications of these phase relationships for the wave–CISK, WISHE, and stratiform instability mechanisms of wave growth will be discussed in the following section.

4.5 Discussion and conclusions

4.5.1 Comparisons of observations with coupled wave instability theories

4.5.1.1 Wave–CISK

As discussed in Section 4.2.1, a central feature of wave–CISK theory is a positive correlation between heating and temperature, generated when low-level convergence forces convection. This relationship implies that latent heating more than compensates for the adiabatic cooling due to upward motion in a wave. Fig. 4.5a indicates a strong spatial and temporal correlation between upper tropospheric temperature and vertical motion (which is highly correlated with low OLR, here considered a proxy for heating) in the reanalysis, and Fig. 4.6b illustrates an in-phase relationship between low OLR and warm upper tropospheric temperatures in radiosonde data. Low-level convergence precedes the heating and temperature anomalies by approximately an eighth of a cycle (Fig. 4.3a). These relationships support the wave–CISK mechanism of coupled wave growth.

In the lower troposphere, the relationship between heating and temperature is less clear. If low OLR is assumed to represent heating throughout the atmospheric column (i.e., a first baroclinic mode heating), then lower tropospheric warm anomalies lead deep heating by at least a quarter cycle (Figs. 4.4a and 4.6b), and there exists a negative correlation between lower tropospheric temperatures and heating. However, the increase in lower tropospheric moisture prior to the lowest OLR (Figs. 4.4b and 4.6c) suggests the

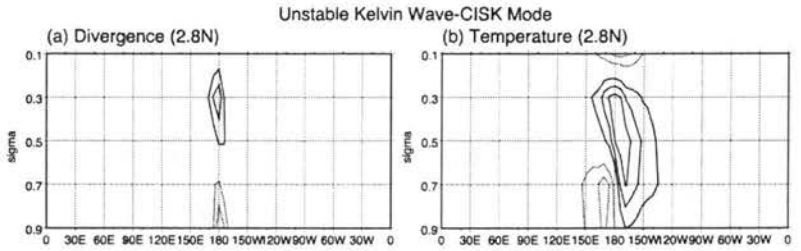


Figure 4.8: Structure of unstable Kelvin wave-CISK mode from Matthews and Lander (1999). Longitude–height cross-sections at 2.8°N of (a) divergence (contour interval is 1 x 10^{-6} s^{-1}) and (b) temperature anomaly (contour interval is 0.2 K). Negative contours are dashed and the zero contour is omitted.

presence of shallow convection leading deep convection, which indicates the possibility of an in-phase relationship between heating and temperature at low levels as well. However, it is difficult to assess lower tropospheric heating and temperature relationships without a detailed knowledge of the shallow convective heating fields. Accurate budgets of the apparent heat source and moisture sink from radiosonde data may also help to illuminate these relationships.

The structure of modeled Kelvin wave–CISK modes can be compared with observed waves to assess the degree to which the modeled waves reproduce observations. Fig. 4.8 illustrates an example of a Kelvin wave–CISK mode from Matthews and Lander (1999). This unstable Kelvin mode was generated in a primitive equation model using a positive-only CISK parameterization scheme, in which convective heating is proportional to low-level convergence. The vertical structure of the heating profile is specified as top-heavy, with maximum heating in the mid-to-upper troposphere. As illustrated in Fig. 4.8, surface convergence slightly leads upper tropospheric divergence in the modeled wave, in a similar manner to the observed waves in Figs. 4.3a and 4.3b. A deep warm anomaly exists ahead of the deep vertical motion, while a second mode temperature anomaly

exists to its west, leading to a positive correlation between heating and upper tropospheric temperature. Observed Kelvin waves also show a second mode temperature anomaly in phase with the deep convective heating, but in general, do not have a deep warm anomaly to the east.

The deep warm anomaly ahead of the convective heating in Fig. 4.8, and the second mode warm over cold anomaly behind it, give the appearance of a westward-tilted temperature anomaly, as noted in observed Kelvin waves in WKW00 and also illustrated in Figs. 4.4a and 4.6b. The very simple convective parameterization in the Matthews and Lander (1999) model is able to reproduce this westward tilt simply because it assumes a top-heavy heating profile [see also similar model results in Lau and Peng (1987), Chang and Lim (1988), and Lim et al. (1990)]. When convective heating is activated, the top-heavy heating profile separates into its component vertical modes, including a first baroclinic "convective" heating and a second baroclinic "stratiform" heating over cooling [see also Mapes (1998)]. The deep warm anomaly ahead of the vertical motion in the modeled wave in Fig. 4.8 is produced by the faster first baroclinic mode propagating out ahead of the heating, while the warm over cold anomaly to the west arises from the more slowly propagating second mode. A positive correlation between heating and upper tropospheric temperature generates the energy required for this instability. The reduced phase speed of 24 m s^{-1} in the unstable Kelvin mode is set by the dry phase speed of the second vertical mode, which produces a stronger convergence anomaly than the first mode and thus more strongly influences the convective heating (Matthews and Lander 1999). Chao (1995) suggests that the maximum wave–CISK instability is produced when

the heating travels eastward with a speed close to, but slightly less than, that of the free Kelvin wave.

The two primary vertical modes into which the initial top-heavy heating profile decomposes in the Matthews and Lander (1999) Kelvin wave–CISK model are similar to the two vertical modes in the stratiform instability model of Mapes (2000), as discussed in Sections 4.3.3 and 4.5.3. In both models, temperature anomalies associated with unstable waves have westward tilts with height, and the propagation speed is set by the second vertical mode. The simple wave–CISK parameterization implicitly subsumes the effects of stratiform precipitation into the top-heavy vertical heating profile, while the stratiform instability model explicitly parameterizes the separate convective and stratiform heating processes. The similarity between the simulated waves in these two models and the observations suggests that the first two baroclinic modes are of primary importance in the dynamics of convectively coupled Kelvin waves.

4.5.1.2 WISHE

WISHE theory predicts that coupled waves in a strict QE system will be modified such that enhanced surface heat fluxes and warm tropospheric temperatures precede upward motion, leading to a positive correlation between heating and temperature, and thus wave amplification. The observations of Kelvin waves in the Pacific presented in Section 4.4 lend some support to the WISHE mechanism, but with several important qualifications.

As illustrated in Fig. 4.2, surface easterly anomalies to the east of the low OLR signal are stronger than the westerly anomalies to its west prior to day 0, when the wave

is amplifying, whereas westerly anomalies are stronger than easterly anomalies after day 0, when the wave is dissipating. Similarly, radiosonde zonal winds (Fig. 4.6d) show stronger easterly than westerly anomalies as a Kelvin wave propagates past. If surface wind speeds are considered to be a good indicator of latent heat flux, these observations provide support for the WISHE mechanism of wave intensification, particularly since the basic state winds in the Pacific during JJA are easterly in the mean. However, observations of Kelvin waves over the Indian Ocean during JJA and Africa during MAM (in regions of prominent but weaker Kelvin wave variance maxima) show consistently stronger westerlies to the west of the convection than easterlies to its east, in both the amplifying and dissipating phases of the wave (see Fig. 4 in WKW00 for the Indian Ocean case). Basic state winds in these regions are near zero to westerly. In contrast to the results for Kelvin waves in the Pacific, the observations in the Indian Ocean and African regions do not support the WISHE mechanism of instability. WISHE therefore cannot be called upon to explain Kelvin wave instability in all regions, but may play a role in the Pacific Kelvin waves.

Observations of Pacific Kelvin waves may also support the WISHE mechanism through the quadrature relationship between lower tropospheric temperatures and upward motion (Fig. 4.5b). In WISHE theory, the warm anomalies located ahead of the maximum upward motion are produced both by the first baroclinic mode Kelvin wave structure, and by the upward flux of surface latent heating anomalies, which is carried out by convection (Fig. 4.1b). The in-phase relationship between anomalous surface easterlies and warm temperatures in the radiosonde data (Figs. 4.6b and 4.6d) provide support for this hypothesis. However, the warm temperatures extend only to 500 hPa in

observations, instead of extending throughout the troposphere in a first baroclinic mode structure as suggested by Emanuel (1987). These observations suggest that shallow convection may play a role in enhancing the lower tropospheric warm anomalies.

The coherent, in-phase relationship between heating (low OLR) and warm temperatures in the upper troposphere illustrated in Figs. 4.4a and 4.6b does not support a WISHE mode of instability. As discussed in the previous section, this relationship suggests a mechanism more consistent with wave–CISK theory.

4.5.1.3 Stratiform instability

The primary control on the organization of convection in stratiform instability theory, as formulated by Mapes (2000), is CIN. A reduction in CIN at the leading edge of a large-scale second baroclinic mode temperature wave allows deep convection to be initiated. Convection is then followed at lag by a second mode stratiform heating over cooling profile. The positive feedback between the second mode temperature wave and the second mode heat source provides the energy for wave amplification. At the trailing edge of the wave, the lower tropospheric cooling declines, and convection dissipates.

Fig. 4.9 illustrates the regressed temperature structure of the modeled eastward-propagating stratiform instability waves in Mapes (2000), centered on the longitude of maximum convective heating. A second baroclinic mode structure is apparent between 1000 and 200 hPa, which is qualitatively similar to the Kelvin wave observations presented in Fig. 4.4a. The fact that the stratiform instability model and observations both show strong second baroclinic mode temperature structures suggests that the stratiform heating component is important for the dynamics of these waves.

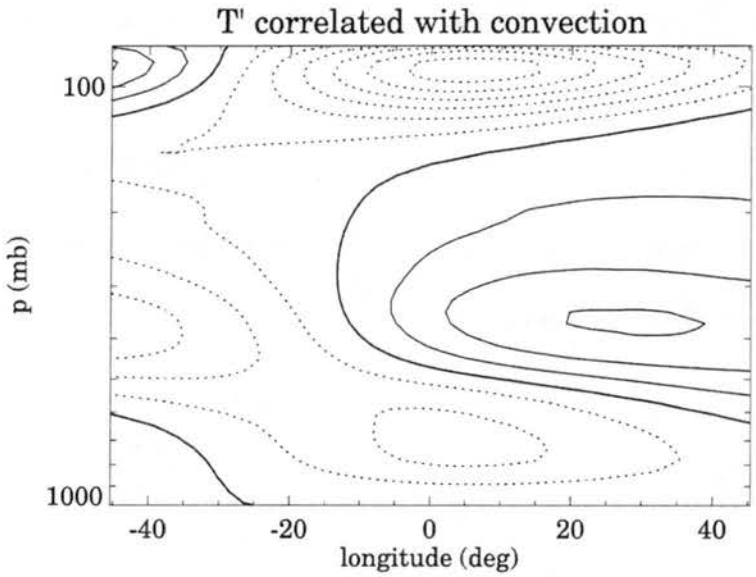


Figure 4.9: Structure of stratiform instability mode from Mapes (2000): longitude–height cross-section of regressed temperature (contour interval 0.25 K), based on a +1 standard deviation anomaly in convection at 0° longitude. Zero contour heavy, negative contours dashed.

Prior to the convective maximum in the modeled wave, a second mode warm over cold anomaly cools the lower troposphere, reducing CIN. The initial lower tropospheric cold anomaly reaches a given location approximately two days prior to the convective maximum (given an eastward phase speed of 23 m s^{-1}, with the edge of the cold anomaly located approximately 40° to the east of the convective maximum, as shown in Fig. 4.9), and increases in intensity until convection maximizes. Observations of Kelvin waves in the Pacific and other locations, however, show a lower tropospheric warming preceding the deep convection in the wave (Figs. 4.4a and 4.6b), and a cooling coincident with the deep convective maximum and thereafter. These observations suggest that a decrease in CIN may not be the driving factor in initiating convection in observed convectively coupled Kelvin waves.

CAPE maximizes in the modeled waves prior to the onset of convection, as also seen in observations (Fig. 4.6e). While convection is active, CAPE remains low, suggesting that the production of available energy by the large-scale vertical motion and moisture fields is offset by its consumption by convection (i.e., a QE balance). In nonconvective periods, positive CAPE anomalies are regenerated primarily by second vertical mode cold over warm anomalies. This evolution is partially supported by observations, which show that the increase in CAPE prior to deep convection is coincident with a warming and moistening at the surface and a cold anomaly aloft (Figs. 4.6b and 4.6c).

The phase relationship between heating and upper tropospheric temperature in the modeled wave in Fig. 4.9 is significantly different from observations, however. In the modeled wave, upper tropospheric warm anomalies lead convection by about 30°, whereas in observations (Fig. 4.6b), upper tropospheric temperature anomalies are in phase with convection. As discussed in Section 4.5.1.1, these observations suggest that latent heating is larger than adiabatic cooling in the upper troposphere in the rising branch of the wave.

Majda and Shefter (2001) also produce eastward-propagating coupled Kelvin-like waves in a linear analytical model in which stratiform instability provides the mechanism for wave growth. The temperature structures tilt westward with height, as in the Mapes (2000) model and in observations, but warm anomalies in the upper troposphere lead convection by approximately a quarter cycle, in contrast to observations. Surface convergence leads deep convection in the modeled waves by less than a quarter cycle, as observed. In contrast to the Mapes (2000) model and observations, however, CAPE

anomalies in the Majda and Shefter (2001) model are in phase with convection, due to the instantaneous CAPE (ICAPE) parameterization scheme.

4.5.2 Conclusions

None of the previously described instability theories (wave–CISK, WISHE, or stratiform instability) accurately predicts all of the features observed in convectively coupled Kelvin waves. Aspects of each theory, however, do appear to be relevant to the observed wave structure. The following discussion suggests an evolution of the coupled Kelvin wave that incorporates each of these theories. This discussion does not provide a definitive explanation of the dynamics involved in convectively coupled Kelvin waves, but instead is intended to provide an interpretation of the observations in the context of the three wave intensification theories.

Observations suggest the existence of a Kelvin wave-like circulation prior to coupled wave intensification. WKW00 present evidence of a fast, uncoupled eastward-propagating surface pressure signal preceding the development of a convectively coupled Kelvin wave in the Indian Ocean. SK02a show shallow surge-like features spreading equatorward from the extratropics in association with an upper tropospheric equatorward-propagating Rossby wavetrain in the Southern Hemisphere, which develop Kelvin-like characteristics when they reach the equator. These observations suggest that a dry, or uncoupled, Kelvin wave circulation might provide the initial forcing necessary for the development of the coupled wave.

Once a preexisting Kelvin wave circulation has been established in the equatorial region, enhanced surface fluxes may occur within the anomalous low-level easterly flow

to the east of the rising branch of the wave, such that shallow convection both moistens and warms the lower troposphere, via a WISHE-type mechanism. This interaction provides a positive correlation between lower tropospheric temperature and shallow convective heating, thus amplifying the lower tropospheric portion of the wave. However, it is important to note that the WISHE mechanism is only relevant in regions of basic state easterlies, such as the Pacific ITCZ, and is not supported by observations of Kelvin waves over the Indian Ocean or Africa. This suggests that WISHE-type interactions play only a secondary role in the evolution of moist Kelvin waves.

In the warm phase of the wave, deep convection is initially suppressed by the low CAPE, increased stability, and high CIN that result from the dry boundary layer and warm lower troposphere. CAPE increases throughout this period through the buildup of surface fluxes beneath the stable lower troposphere (Parker 2002) and the convergence of moisture forced by the convergent lower tropospheric winds. As the Kelvin wave circulation propagates eastward, the wave-induced lower tropospheric warm anomalies begin to subside, such that convection is able to increase in vertical extent, initially feeding on the high CAPE and boundary layer moisture remaining from the suppressed phase. Low-level convergence and deep upward motion in this phase of the wave then provide a continuous source of moisture and instability to fuel deep convection.

Within the large-scale envelope of upward motion, deep convection organizes into larger-scale cloud systems that generate regions of stratiform precipitation, consistent with the stratiform instability mechanism. The combination of the convective and stratiform heating profiles within these numerous mesoscale cloud systems produces a large-scale top-heavy heating distribution. A QE-like state is maintained, with small

but significant departures from exact thermodynamic balance evident in the upper (lower) tropospheric warm (cold) anomalies. The coexistence of these primarily second baroclinic mode temperature anomalies and the top-heavy heating profile provides a positive correlation between temperature and heating in the upper troposphere, in a manner consistent with both the wave–CISK and stratiform instability mechanisms. The westward tilt with height of the temperature anomalies results from a combination of the shallow convective heating and/or dry Kelvin wave-like structure in the lower troposphere to the east of the deep convection, and the top-heavy heating profile in the region of deep ascent in the wave. Since heating and warm temperature anomalies are in phase in the upper troposphere as well as the lower troposphere, the coupled wave grows in amplitude.

The observations and discussions presented in this paper are intended to motivate future modeling studies of convectively coupled equatorial waves. Successful simulations of these coupled modes will undoubtedly provide additional insights into the fundamental relationships between convection and the large-scale circulation in the tropics.

5 INTERACTIONS BETWEEN THE BOREAL SUMMER INTRASEASONAL OSCILLATION AND HIGHER-FREQUENCY TROPICAL WAVE ACTIVITY

5.1 Introduction

The boreal summer intraseasonal oscillation (ISO)[5] is a slowly northward- and eastward-propagating oscillation in cloudiness and circulation with a period of approximately 30–60 days (Yasunari 1979, 1980, 1981; Krishnamurti and Subahmanyam 1982; Knutson et al. 1986; Lau and Chan 1986; Knutson and Weickmann 1987; Madden and Julian 1994; Kemball-Cook and Wang 2001; Lawrence and Webster 2002). The primary convective signal of the ISO is localized to the Indian Ocean and western Pacific regions, while circulation anomalies extend throughout the tropics and into the extratropics. The zonal extent of deep tropical convection in the active phase of the ISO can be quite large, stretching from the Indian Ocean to the western Pacific.

Embedded within the slowly varying ISO cloudiness signal are multiple higher-frequency, smaller spatial scale convective events (Yasunari 1979; Nakazawa 1988; Mapes and Houze 1993; Hendon and Liebmann 1994; Dunkerton and Crum 1995). Observations suggest that the low-frequency ISO signal may represent a moving

[5] The ISO is also known as the Madden–Julian Oscillation, or MJO.

envelope of higher-frequency convective activity, rather than a slowly migrating band of enhanced mean cloudiness (Nakazawa 1988; Hendon and Liebmann 1994; Dunkerton and Crum 1995). High-frequency cloudiness events can project onto lower-frequency modes such as the ISO because tropical convection is a nonlinear or "conditional" process; the net precipitation and latent heating anomalies will be positive when averaged over the longer timescale of the ISO. Dunkerton and Crum (1995) and Matthews and Kiladis (1999) suggest that the higher-frequency convective activity within the ISO may also be responsible for forcing the large-scale, low-frequency circulation of the ISO itself. This allows for a potential feedback between the circulation forced by the higher-frequency convective events and the development and evolution of the events themselves.

The recent studies of Wheeler and Kiladis (1999, hereafter WK99) and Wheeler et al. (2000, hereafter WKW00) have demonstrated that a significant portion of submonthly (<30 day) convective variability in the tropics can be explained in terms of zonally-propagating convective disturbances which correspond to the linear equatorial wave modes predicted by Matsuno (1966). In the present study, the relationship between two of these wave types and the boreal summer ISO is examined. The motivation for this work began with a desire to understand how convectively coupled, equatorially trapped waves are affected by the slowly varying circulation fields of the ISO. The results, however, suggest that the waves themselves may not be independent from the lower-frequency ISO fields, but instead may provide some of the variability that comprises the ISO itself.

The two convectively coupled wave types to be examined in this study are mixed Rossby-gravity (MRG) waves and Kelvin waves. Mixed Rossby-gravity waves are

westward-propagating disturbances with zonal wavelengths of 6000–8000 km and phase speeds of 20–25 m s^{-1} (Liebmann and Hendon 1990; Hendon and Liebmann 1991; Dunkerton 1993; Dunkerton and Baldwin 1995; WKW00). MRG waves have been documented to evolve into off-equatorial tropical depression (TD)-type disturbances in the western Pacific (Lau and Lau 1992; Takayabu and Nitta 1993; Dunkerton and Baldwin 1995; Sobel and Bretherton 1999; Dickinson and Molinari 2002). Kelvin waves (WKW00; Straub and Kiladis 2002a, hereafter SK02a; Straub and Kiladis 2002b, hereafter SK02b) are eastward-propagating convective disturbances that are similar in scale (zonal wavelengths of 2000–4000 km) and phase speed (15 m s^{-1}) to the super cloud clusters discussed by Nakazawa (1988) and Takayabu and Murakami (1991). These two wave classes (MRG/TD and Kelvin) together represent about 25% of the convective variability in the Pacific during boreal summer (WKW00; SK02b).

This study uses a combination of statistical results and illustrations from a case study during July–September 1987 to demonstrate that the boreal summer ISO convective envelope often consists of an enhancement of westward-propagating MRG/TD variability within the envelope itself, and an enhancement of eastward-propagating Kelvin wave activity to its east.

5.2 Data and methodology

Two primary datasets are utilized in this study. The signals of the ISO and higher-frequency tropical waves are identified using NOAA outgoing longwave radiation (OLR) data (Liebmann and Smith 1996). OLR is used as a proxy for deep tropical convection, as in many previous studies (Matthews and Kiladis 1999; WK99; WKW00;

SK02a, b). The atmospheric circulation is represented by the National Center for Environmental Prediction/National Center for Atmospheric Research (NCEP/NCAR) reanalysis wind fields. Both the OLR and NCEP/NCAR reanalysis datasets are available on a global 2.5° grid, and extend from 1979–2000. The data have been averaged to daily temporal resolution from four times daily (reanalysis) or twice daily (OLR) resolution.

The OLR data are filtered in wavenumber–frequency space to extract signals associated with the ISO and convectively coupled waves, as described in WK99. The raw OLR data are passed through a set of wavenumber–frequency filters that enclose the climatological regions of enhanced spectral power corresponding to each disturbance type. A reverse transform back to physical space then results in a separate OLR dataset for each filtered region. The reader is directed to Fig. 6 of WK99 for an illustration of the approximate filtering regions for Kelvin waves, MRG waves, and the ISO.[6] In the present study, the Kelvin wave filter spans eastward-propagating periods of 2.5–17 days and zonal wavenumbers 1–14, and is bounded by the theoretical Kelvin wave dispersion curves for equivalent depths of 8 and 90 m. The MRG filter spans westward-propagating periods of 3–7.5 days and zonal wavenumbers 0–10, and is bounded by the 8 and 90 m MRG wave dispersion curves. The ISO filter spans eastward-propagating periods of 30–96 days and zonal wavenumbers 0–5. As in SK02a and SK02b, both the symmetric and antisymmetric OLR components with respect to the equator are allowed to pass through the wavenumber–frequency filter for all waves in this study. This allows for a

[6] Several changes have been made in this study to the wavenumber–frequency filtering regions in WK99. The lower boundary of the Kelvin wave region has been moved upward to a period of 17 days from 30 days, as in SK02a and SK02b. The wavenumber boundaries of the ISO and MRG filtering regions now include zonal wavenumber 0. This change allows for a representation of the zonally symmetric component of variability, representing standing oscillations, in the filtered data.

better representation of the off-equatorial OLR signal in convectively coupled Kelvin waves in the Pacific (SK02a, b), and allows the MRG waves to evolve from their typical antisymmetric OLR pattern in the central Pacific to asymmetric tropical depression (TD)-like convective patterns in the western Pacific. Illustrations of the typical horizontal structures of MRG waves and TD disturbances are presented in Section 5.3.

The statistical results presented in Section 5.3 are based on a linear regression technique, as described in Matthews and Kiladis (1999). The low-frequency signals in convection and circulation associated with the ISO are determined by regressing total OLR and reanalysis winds at all grid points against an index of the ISO for the 22 boreal summers (June–July–August, JJA) from 1979–2000. The ISO index is the daily value of the ISO-filtered OLR, averaged over a 5° x 5° box around the point of its maximum climatological variance during JJA. The box extends from 7.5°–12.5° N and 100°–105° E. Results are fairly insensitive to the choice of box location and size. The modulation of higher-frequency waves by the slowly varying ISO OLR signal is determined in a similar manner, by regressing the variance of the filtered OLR datasets (Kelvin, MRG/TD), as represented by the square of the daily value at each grid point, against the ISO index. This method requires a clear separation between the timescale of the ISO index and that of the tropical waves. Since the shortest period fluctuations in the ISO index are 30 days, and the tropical waves have cutoffs at periods well below this, the method is justified in the present case. It is not necessary to "window" the MRG/TD and Kelvin filtered OLR data to 30–96 day periods as in Matthews and Kiladis (1999), since the regression procedure automatically extracts fluctuations on these timescales associated with the filtered ISO OLR index.

All ISO regression results are scaled to a –1.5 standard deviation anomaly in the ISO OLR index on day 0, which corresponds to an OLR anomaly of approximately –20 W m^{-2}, averaged over the 5° x 5° base area. Signals are considered to be statistically significant at the 95% level or greater, as in WKW00. Other ISO indices, based on 200- or 850-hPa zonal wind or EOF-based OLR, have been tested and the results are consistent with those presented in Section 5.3. Composite fields have also been calculated, and the results are also similar to those presented in Section 5.3.

5.3 Statistical results

5.3.1 ISO convection and circulation anomalies

The regressed OLR (shading) and 850-hPa circulation anomalies (streamfunction contours, vector winds) during one cycle of the boreal summer ISO are shown in Fig. 5.1, for days –15, –5, +5, and +15. On day –15 (Fig. 5.1a), low OLR, representing enhanced convection, extends over a large portion of the equatorial Indian Ocean, while a band of suppressed convection stretches southeastward from India toward the Dateline in the Northern Hemisphere. The band of suppressed convection had moved northward and eastward prior to day –15 as the new ISO active convective phase intensified in the Indian Ocean. Associated with the suppressed convective phase on day –15 is an elongated 850-hPa anticyclonic circulation anomaly in the Northern Hemisphere. Easterly wind anomalies are collocated with a large portion of the suppressed convective region. This anticyclonic circulation anomaly represents a strengthening and westward

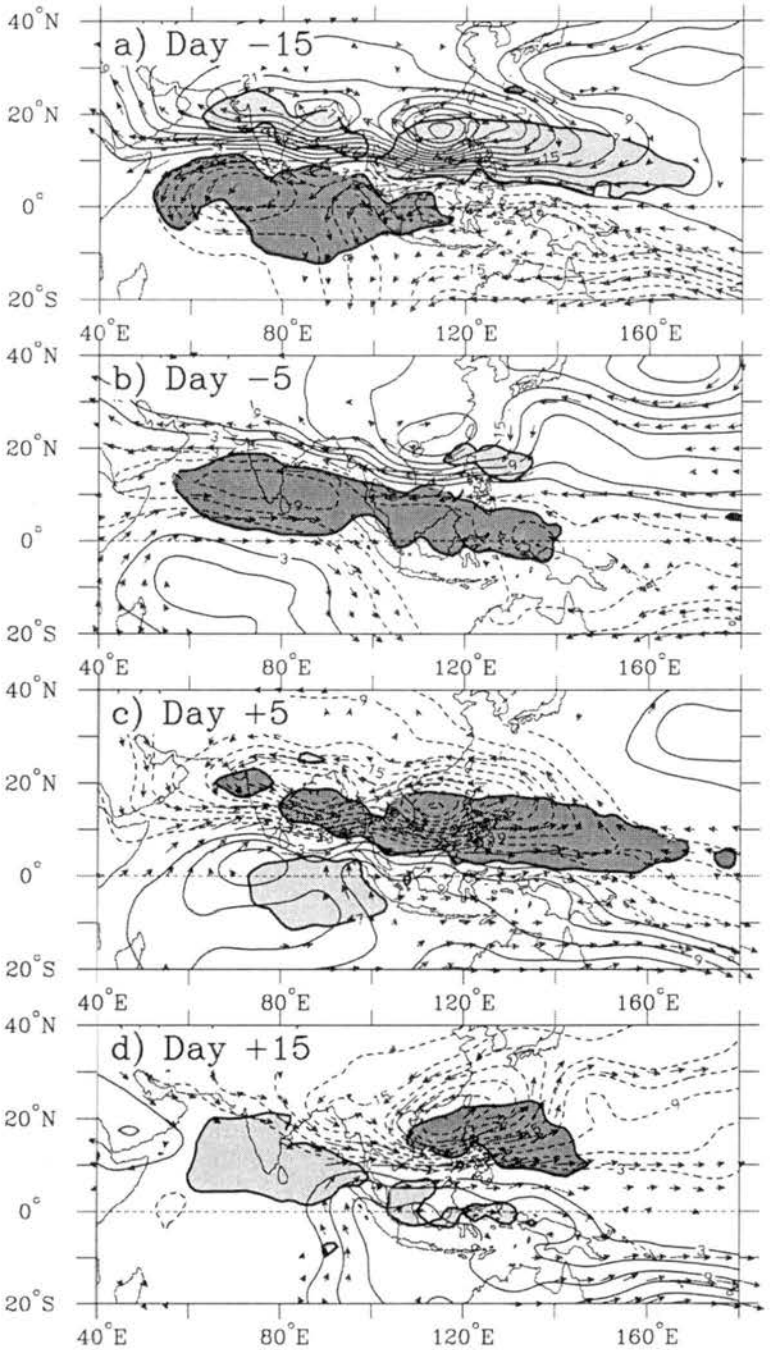


Figure 5.1: Regressed OLR (shading, dark negative, at ±7 W m^{-2}) and 850-hPa streamfunction (light contours, solid positive, by 3 x 10^5 m^2 s^{-1}, zero contour omitted) and wind vectors (plotted only where significant at the 95% level or greater; longest vectors 5 m s^{-1}) on (a) day −15, (b) day −5, (c) day +5, and (d) day +15, based on a −1.5 standard deviation anomaly in the ISO index on day 0.

shift of the climatological North Pacific subtropical high. A period displaying these convection and circulation features is often referred to as a break monsoon period (Krishnamurti and Subrahmanyam 1982).

The enhanced ISO convection moves northward and expands eastward by day –5 (Fig. 5.1b), while the suppressed phase dissipates to the north of the Philippines. Easterly anomalies remain present to the north of the enhanced convective region, but are now associated with the developing trough over southern India. As the enhanced convective region continues to move northward and eastward, the trough strengthens such that strong 850-hPa westerly anomalies are collocated with the convection on day +5 (Fig. 5.1c). This pattern represents an active monsoon period, with a strong monsoon trough and a weaker North Pacific subtropical high. Finally, by day +15, the enhanced phase of the ISO is located to the north of the Philippines, while the suppressed phase has also moved northward and is located over the northern Indian Ocean.

The temporal and spatial evolution of OLR and circulation in Fig. 5.1 is consistent with earlier studies such as Krishnamurti and Subrahmanyam (1982), Knutson and Weickmann (1987), and Lawrence and Webster (2002). The ISO convection and circulation fields are quite linear in their evolution, such that the maps on days –15 and +5 display opposite-signed anomalies, as do the maps on days –5 and +15. From these figures the period of the ISO convective anomalies can be estimated to be approximately 40 days, also consistent with previous studies.

5.3.2 Mixed Rossby-gravity waves/TD-type disturbances

Westward-propagating synoptic-scale disturbances in the western Pacific have been studied extensively by Reed and Recker (1971), Hendon and Liebmann (1991), Lau and Lau (1992), Takayabu and Nitta (1993), Sobel and Bretherton (1999), Dickinson and Molinari (2002), and many others. The broad spectrum of westward-propagating disturbances in this region is often categorized into three wave types: easterly waves, mixed Rossby-gravity waves, and tropical depression-type disturbances. The distinctions between these wave types are not necessarily clear, however, such that observed disturbances may display characteristics of more than one type, or represent a transition between types.

Previous studies agree that large-scale, westward-propagating disturbances often behave like theoretical MRG waves in the central Pacific (near the Dateline), with enhanced (suppressed) convection in the region of lower tropospheric off-equatorial convergence (divergence) associated with cross-equatorial flow. Observations of MRG waves coupled to convection show that they generally have zonal wavelengths on the order of 6000–8000 km and westward phase speeds of 20–25 m s^{-1} (Liebmann and Hendon 1990; Hendon and Liebmann 1991; Dunkerton and Baldwin 1995; WKW00). As these waves propagate westward into the western Pacific, however, they tend to lose their equatorial antisymmetry in convection and their symmetry in the meridional wind field, and evolve into off-equatorial vortical structures whose centers fill with convection (Takayabu and Nitta 1993; Dickinson and Molinari 2002). These disturbances are generally referred to as tropical depression (TD)-type disturbances, as they often serve as

the precursors to tropical cyclones in the western Pacific (Lau and Lau 1992; Takayabu and Nitta 1993; Sobel and Bretherton 1999; Dickinson and Molinari 2002).

In this study, MRG and TD-type disturbances are identified using the MRG OLR index of WKW00, which is based on the climatological OLR spectral peak along the MRG dispersion curves. Unlike WKW00, however, in the present study both the antisymmetric and symmetric components of OLR are allowed to pass through the MRG filter. With this change, the index is now able to represent both the antisymmetric MRG waves in the central Pacific and the off-equatorial TD-type disturbances in the western Pacific. To illustrate the difference between these two wave types, Fig. 5.2a shows the regressed OLR (shading) and 850-hPa circulation fields (streamfunction and vector winds) based on the MRG/TD index in the central Pacific, at 5°N, 175°E, on day 0. Note the antisymmetric OLR pattern, with low (high) OLR in the Northern (Southern) Hemisphere in the region of lower tropospheric convergence (divergence). The streamfunction anomalies are centered on the equator, as expected. The zonal wavelength is approximately 70°, and the circulation anomalies move westward at 20–25 m s^{-1}. The fields obtained using the MRG OLR index in Fig. 5.2a are very similar to those obtained by Liebmann and Hendon (1990) using 850-hPa meridional wind as a predictor, Hendon and Liebmann (1991) using 4–5 day filtered antisymmetric OLR fluctuations, and Takayabu and Nitta (1993) using 2.5–10 day filtered GMS infrared (IR) temperature perturbations.

Figure 5.2b shows a similar plot, but for the regressed OLR and circulation fields based on the MRG/TD index in the western Pacific, at 10°N, 135°E. The circulation anomalies are now centered off of the equator, and propagate northwestward. The OLR

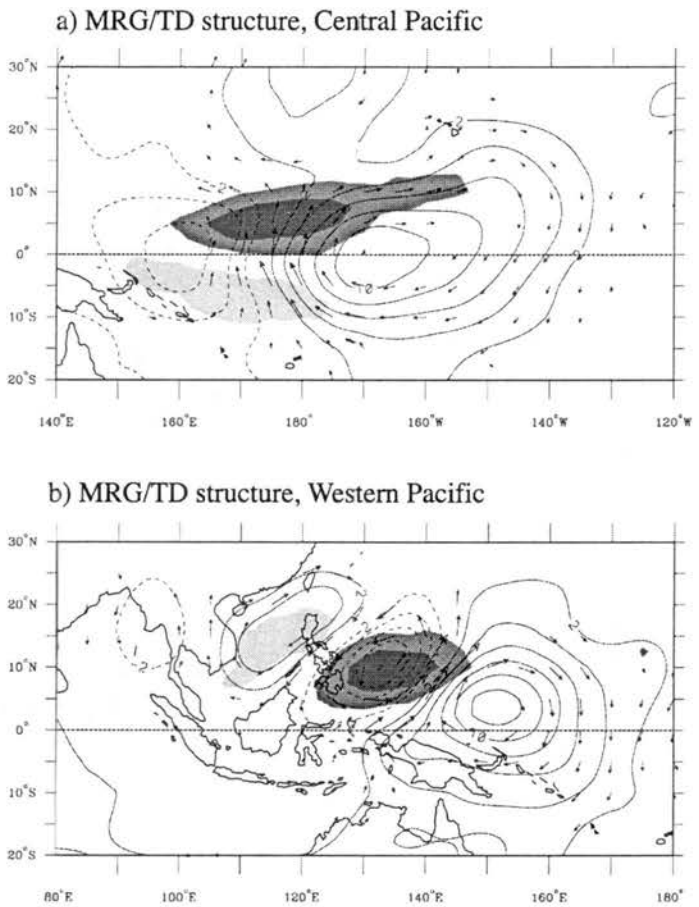


Figure 5.2: Regressed OLR (shading, dark negative, at ±6 and 15 W m^{-2}) and 850-hPa streamfunction (light contours, solid positive, by 2.0 x 10^5 m^2 s^{-1}, zero contour omitted) and wind vectors (plotted only where significant at the 95% level or greater; longest vectors 3 m s^{-1}) on day 0, based on a –20 W m^{-2} anomaly in the MRG/TD OLR index at (a) 5°N, 175°W, and (b) 10°N, 135°W.

anomalies are in phase with the circulation anomalies, with low (high) OLR associated with anomalous cyclonic (anticyclonic) 850-hPa circulations. The scale of the circulation and convection anomalies is smaller than in Fig. 5.2a, with a wavelength of approximately 35°, and the anomalies propagate westward much more slowly, at 5–10 m s^{-1}. These results are consistent with those obtained for TD-type disturbances by Lau and Lau (1992) and Sobel and Bretherton (1999) using 850-hPa vorticity as a predictor, and Takayabu and Nitta (1993) using 2.5–10 day filtered GMS IR data.

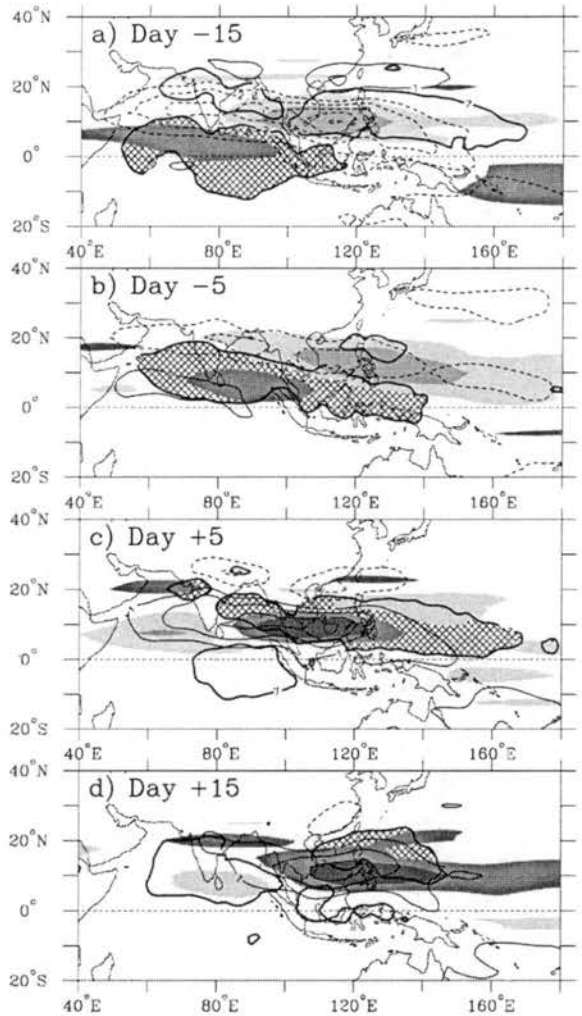


Figure 5.3: Regressed OLR (dark contours at ±7 W m^{-2}, hatching for negative anomalies), 850-hPa zonal wind (light contours, solid positive, by 1 m s^{-1}, zero contour omitted), and MRG/TD filtered OLR variance (shading, dark positive, at ±5 and 15 W^2 m^{-4}) on (a) day −15, (b) day −5, (c) day +5, and (d) day +15, based on the ISO OLR index.

Figure 5.3 shows the evolution of the MRG/TD wave activity field (as represented by the variance of the filtered MRG/TD dataset) associated with the low-frequency ISO convection and circulation fields, on days −15, −5, +5, and +15. The crosshatched areas represent the enhanced ISO convective anomalies (identical to the dark shading in Fig. 5.1), and the dark contours without shading represent the suppressed ISO convective anomalies. The dark (light) shading represents enhanced (suppressed)

MRG/TD activity. The solid (dashed) light contours represent 850-hPa westerly (easterly) anomalies.

On day –15 (Fig. 5.3a), weakly enhanced MRG/TD activity is collocated with the enhanced low-frequency ISO convection in the equatorial Indian Ocean. MRG/TD activity is strongly suppressed in the region of ISO suppressed convection, particularly in the South China Sea from 5°–15°N, in the region of 850-hPa easterly anomalies. As the enhanced ISO convection moves northward and eastward in time, the region of enhanced MRG/TD activity also moves northeastward, as can be seen on day –5 (Fig. 5.3b). The suppressed MRG/TD activity expands eastward along the northwest-southeast-tilted axis of suppressed ISO convection, remaining collocated with 850-hPa easterly anomalies. By day +5 (Fig. 5.3c), the regions of enhanced MRG/TD activity, ISO convection, and 850-hPa westerlies have all continued to move northeastward and intensify, while the suppressed MRG/TD activity, suppressed ISO convection, and easterly anomalies have largely dissipated. The MRG/TD activity spreads eastward by day +15 (Fig. 5.3d), along with the enhanced ISO convection and 850-hPa westerlies. The MRG/TD wave activity fields show a remarkably coherent relationship with the ISO convection and 850-hPa zonal wind fields.

Aiyyer and Molinari (2002) suggest that the convergent wind field of the ISO allows equatorial MRG waves to transition into smaller scale, off-equatorial TD disturbances, based on idealized shallow water model simulations. Observations do show a positive correlation between enhanced MRG/TD activity and 850-hPa ISO convergence anomalies (not shown); however, the spatial correlation appears to be stronger between enhanced MRG/TD activity and 850-hPa westerly anomalies.

There has been little theoretical work to date on the relationship between convectively coupled (moist) equatorial waves and the sign and magnitude of the background wind field. Zhang and Webster (1989) demonstrate that dry MRG waves are less meridionally trapped in westerlies than in easterlies, suggesting that westerly winds may be conducive to the formation of higher amplitude, more latitudinally extensive MRG waves. In addition, Zhang (1993) shows that extratropically forced MRG waves have larger amplitudes in basic state westerlies when the period of the forcing is greater than 4 days. Since the period of the observed convectively coupled MRG/TD waves in this study varies between 4 and 6 days from the central Pacific to the western Pacific, and the level of MRG/TD activity has been shown to vary strongly as a function of the 850-hPa zonal wind, it is possible that the amplitude of MRG/TD activity may simply be a function of the low-frequency "background" ISO winds. However, as will be shown in Section 5.4, the convection associated with the enhanced MRG/TD activity may comprise a substantial fraction of the low-frequency ISO signal, and as such, may itself be partially responsible for accelerating the westerlies and deepening the monsoon trough. A feedback mechanism may exist that allows the enhanced MRG/TD activity to provide the conditions necessary for the continued development of both the ISO and the wave activity itself.

5.3.3 Kelvin waves

Convectively coupled Kelvin waves in the Indian Ocean and western Pacific regions have been studied by WKW00, SK02a, and SK02b. SK02b identified convectively coupled Kelvin waves as the "super cloud clusters" studied by Nakazawa

(1988) and Takayabu and Murakami (1991). Convectively coupled Kelvin waves are convective disturbances of zonal scale 2000–4000 km and eastward phase speed 15–20 m s^{-1}, that are coupled to equatorially trapped, Kelvin-like dynamical fields in the tropical troposphere and stratosphere. Nakazawa (1988) and SK02b show that these eastward-propagating convective envelopes are often composed of smaller-scale, westward-propagating "cloud clusters."

The evolution of Kelvin wave activity with respect to the ISO is shown in Fig. 5.4, which illustrates the regressed Kelvin wave variance (shading), ISO OLR (hatching, as in Fig. 5.3) and 200-hPa circulation (streamfunction contours, vector winds). On day –15 (Fig. 5.4a), weakly enhanced Kelvin wave activity is collocated with the developing low-frequency ISO OLR anomaly in the equatorial Indian Ocean, in a similar manner to the MRG/TD activity illustrated in Fig. 5.3a. Thus, as the ISO convective anomaly intensifies in the Indian Ocean region on day –15, both eastward-propagating Kelvin waves and westward-propagating MRG/TD waves may be contributing to this lower-frequency convective anomaly. At the same time, suppressed Kelvin wave activity stretches across the Pacific in the Northern Hemisphere, far removed from the suppressed ISO OLR signal in the northern Indian Ocean and western Pacific.

As the ISO convective region moves northward and expands eastward by day –5 (Fig. 5.4b), the enhanced Kelvin wave activity moves rapidly eastward into the western and central Pacific. Enhanced Kelvin wave activity is no longer collocated with the enhanced ISO OLR signal, as is the MRG/TD activity in Fig. 5.3b. The enhanced Kelvin wave activity lies in a region of 200-hPa anomalous westerlies (and 850-hPa easterlies), to the north of a zonally elongated subtropical trough in the Southern Hemisphere. By

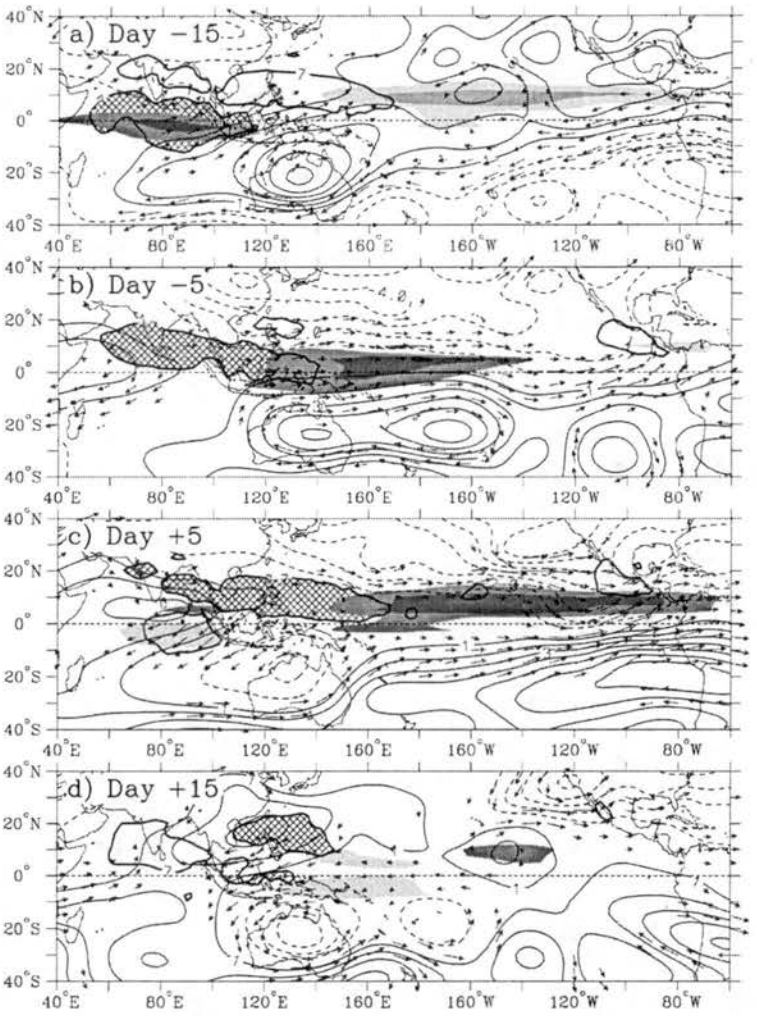


Figure 5.4: Regressed OLR (as in Fig. 3), 200-hPa streamfunction (light contours, solid positive, by 1.0 x 10^6 m^2 s^{-1}, zero contour omitted) and wind vectors (plotted only where significant at the 95% level or greater; longest vector 7 m s^{-1}), and Kelvin filtered OLR variance (shading, dark positive, at ±15 and 30 W^2 m^{-4}) on (a) day –15, (b) day –5, (c) day +5, and (d) day +15, based on the ISO OLR index.

day +5 (Fig. 5.4c), the enhanced Kelvin wave activity has expanded even farther eastward, stretching across the entire Pacific basin. Finally, by day +15 (Fig. 5.4d), as the enhanced ISO convection dissipates to the north of the Philippines, the enhanced Kelvin wave activity also decreases over the Pacific.

These results indicate that the low-frequency ISO OLR signal may initially consist of both MRG/TD and Kelvin wave activity in the Indian Ocean region, but that as

the ISO convection moves northward, it no longer represents an enhancement of Kelvin wave (or super cluster) activity. Hendon and Liebmann (1994) also found that ISO convective envelopes contained very little eastward-propagating super cluster variance. Instead, it is shown here that enhanced Kelvin wave activity is found well to the east of the ISO OLR convection, maximizing in the central Pacific. This relationship suggests that Kelvin waves may be initiated by the active convection within the ISO envelope, and then subsequently propagate eastward across the Pacific. Although dry Kelvin waves have theoretically been shown to be unaffected by vertical wind shear (Wang and Xie 1996), it is possible that convectively coupled Kelvin waves preferentially form (or are more readily sustained after formation) in the enhanced low-level basic state easterlies or weakened upper-level basic state easterlies in the Pacific that are associated with the large-scale dynamical response to ISO convection.

As an alternative hypothesis to explain the enhancement of Kelvin wave variance to the east of the ISO convective anomaly, SK02a show that the initiation of convectively coupled Kelvin waves in the central Pacific during boreal summer is associated with an equatorward-propagating Rossby wavetrain excited in the Southern Hemisphere subtropical jet. If the circulation fields associated with the low-frequency ISO convection cause low-frequency changes in the characteristics of wave activity in the jet, it is possible that these changes could subsequently cause low-frequency changes in tropical Kelvin wave activity. A related mechanism for the boreal winter ISO is proposed in Matthews and Kiladis (1999), in which ISO convection forces low-frequency changes in both the Northern Hemisphere Asian jet and the downstream basic state,

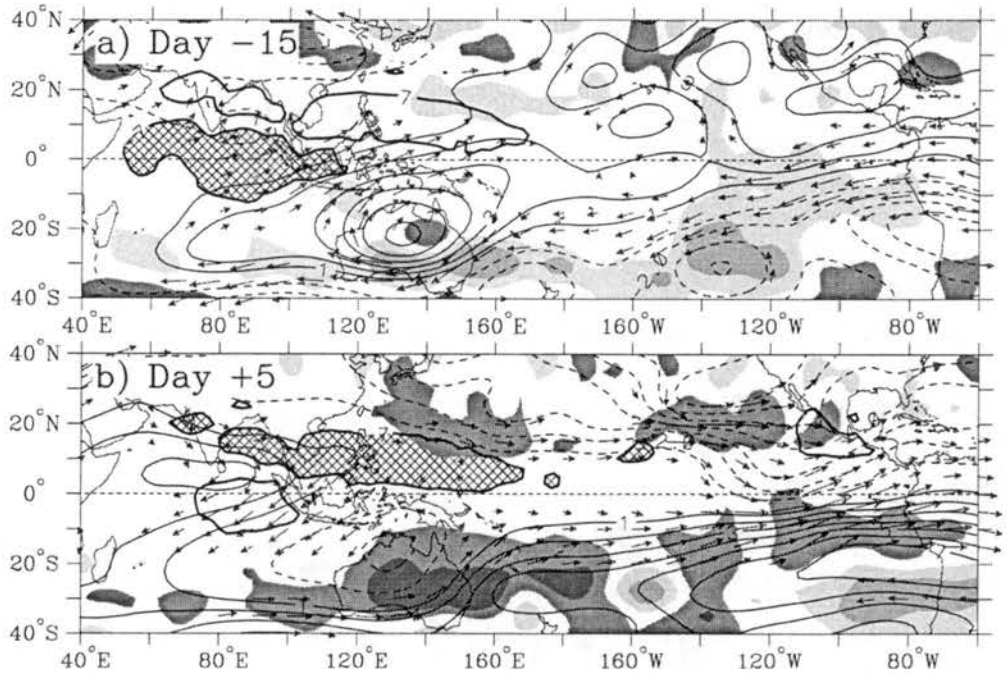


Figure 5.5: Regressed OLR, 200-hPa streamfunction, and wind vectors as in Fig. 5.4, and <30 day filtered meridional wind variance (shading, dark positive, at ±5 and 15 $m^2 s^{-2}$), on (a) day –15 and (b) day +5, based on the ISO OLR index.

which then affects the supply and evolution of equatorward-propagating Rossby waves in the eastern Pacific.

The Southern Hemisphere subtropical jet is located along approximately 30°S during JJA, and maximizes just to the east of Australia. Rossby waves excited in the jet often propagate northeastward over Australia, then eastward along approximately 20°S (Chang 1999; SK02a). Therefore, low-frequency changes in the circulation along 30°S represent fluctuations in the strength and location of the subtropical jet, and may be correlated with changes in wave activity within the jet. The variance of <30 day filtered 200-hPa meridional wind is used here as a measure of Rossby wave activity in the jet, as in SK02a.

On day –15 (Fig. 5.5a), a subtropical low pressure anomaly is located over Australia, which developed in association with the anomalous upper tropospheric inflow

to (i.e., weaker than normal outflow from) the suppressed convective region in the western Pacific. Easterly anomalies extend along 35°S from the central Indian Ocean to eastern Australia. Since the climatological subtropical jet core is located over eastern Australia, the easterly anomalies to the west of 140°E represent a weakening of the entrance region of the jet. Wave activity along the jet is weaker than normal, as evidenced by the negative anomalies in submonthly meridional wind variance over Australia and to its east. Kelvin wave activity in the Pacific is substantially diminished at this time, as shown in Fig. 5.4a.

As the suppressed ISO convective region dissipates and the enhanced convective region expands, the cyclonic circulation anomaly in the Southern Hemisphere expands eastward (see Fig. 5.4b), consistent with a rotational response to the strengthening equatorial westerlies forced by the upper tropospheric outflow from the ISO convection. At this time, the anomalous easterlies along 30°S to the east of 120°E weaken the climatological exit region of the subtropical jet, and wave activity begins to propagate northward and southward of the climatological jet location (not shown).

By day +5 (Fig. 5.5b), the entrance region of the subtropical jet is strengthened by the ISO-influenced westerly anomalies associated with the anticyclonic outflow from the enhanced ISO convection in the Northern Hemisphere. Anomalously high Rossby wave activity is found along the climatological jet axis at this time, extending along the anomalous southwesterly flow toward the tropics. Consistent with the analysis in SK02a, anomalous E-vectors point northeastward at this time (not shown), signifying the enhanced equatorward propagation of Rossby wave activity over Australia. These equatorward-propagating Rossby wave perturbations may then excite convectively

coupled Kelvin waves in the Pacific, as illustrated in SK02a, and produce the enhanced Kelvin wave variance signal seen in the tropics of the Northern Hemisphere in Fig. 5.4c.

The results presented in Sections 5.3.1 and 5.3.2 have been confirmed using several other methodologies. The MRG/TD results are consistent with regressions based on 850-hPa 30–70 day filtered zonal wind in the northern Indian Ocean region, and the Kelvin wave results are consistent with regressions based on the 200-hPa 30–70 day filtered zonal wind in both the Southern Hemisphere subtropical jet region and the equatorial Pacific. Both sets of results can also be duplicated through a calculation of composite fields during strong ISO events.

5.4 Case study: July–September 1987

The period of July–September 1987 provides an excellent real-time illustration of the statistical relationships presented in Section 5.3. An overview of tropical convection during this period is shown in Fig. 5.6, a Hovmöller diagram of total OLR (shading) and filtered OLR in the ISO, MRG/TD, and Kelvin bands (contours), averaged from 2.5°–15°N. A suppressed convective phase of the ISO during July is followed by an enhanced phase in August, as shown by the slowly eastward-propagating contours representing the filtered ISO OLR. As might be expected based on the OLR distribution, the Indian subcontinent experienced a severe drought during July 1987, while conditions improved during August (Krishnamurti et al. 1989).

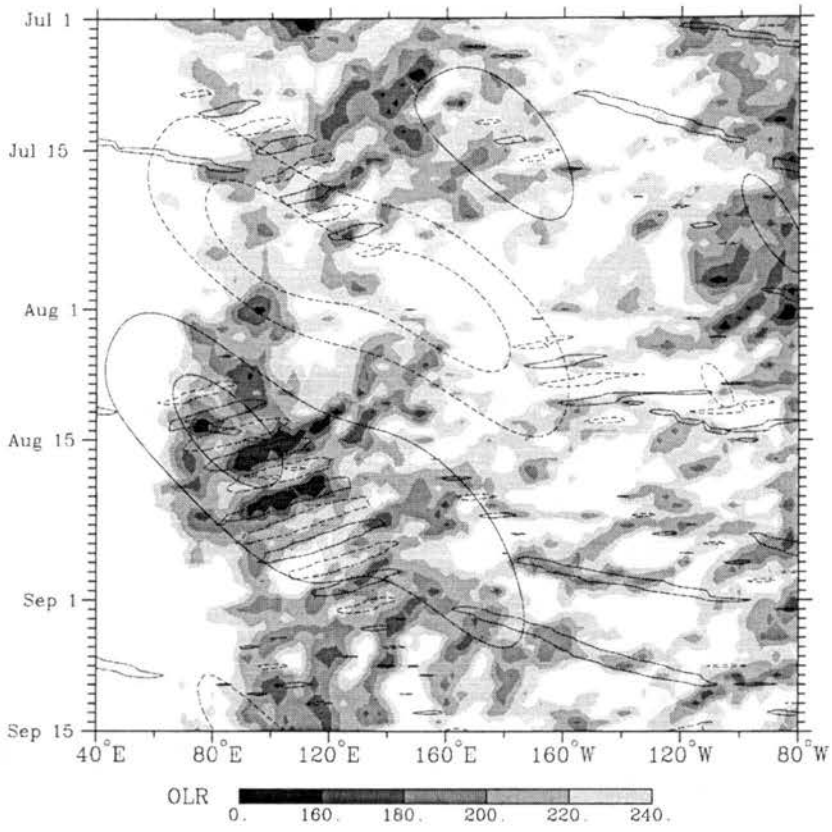


Figure 5.6: Time–longitude plot of total OLR (shading, as indicated), filtered ISO and MRG/TD OLR (contours, solid negative, contour interval 10 W m^{-2}, zero contour omitted), and filtered Kelvin wave OLR (contoured at –12 W m^{-2} only), averaged from 2.5°N–15°N, from 1 July to 15 September 1987.

5.4.1 Westward-propagating modes

It is clear from Fig. 5.6 that the eastward-propagating active ISO convective signal during August 1987 is composed of many shorter timescale, smaller spatial scale convective events, many of which propagate westward with time. For example, a strong MRG/TD wave packet comprises a substantial portion of the enhanced ISO convective phase. Horizontal maps of the convection and circulation fields during the enhanced ISO phase are shown in Fig. 5.7, which illustrates the total OLR (shading), 30–96 day filtered 850-hPa zonal wind (light contours) and wind vectors, and ISO filtered OLR (dark contour surrounds negative OLR anomalies less than –10 W m^{-2}), every 5 days from 13

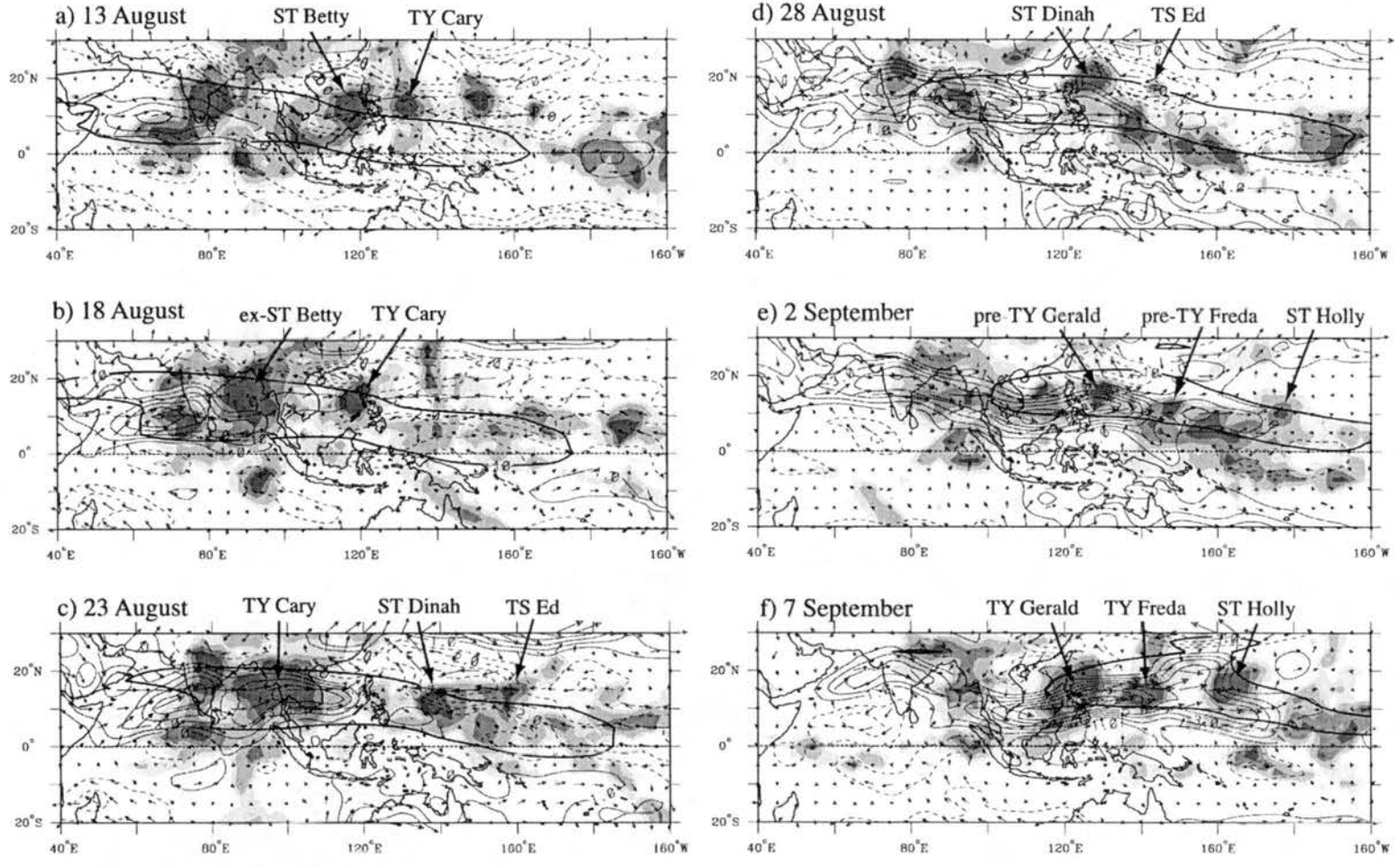


Figure 5.7: Total OLR (shading for values <160, 190, 220, and 240 W m^{-2}), ISO filtered OLR (dark contour at –10 W m^{-2}), 850-hPa 30–96 day filtered zonal wind (light contours, solid positive, by 1 m s^{-1}), and 850-hPa 30–96 day filtered wind vectors (longest vectors 4 m s^{-1}) for (a) 13 August, (b) 18 August, (c) 23 August, (d) 28 August, (e) 2 September, and (f) 7 September 1987. Locations of tropical storms provided by Colorado State University/Tropical Prediction Center.

August 1987 to 7 September 1987. Locations of named tropical storms are indicated. It will be shown in this section that these western Pacific tropical cyclones and their associated circulation anomalies are the precursors to the MRG/TD disturbances indicated in Fig. 5.6, and also provide much of the convective variability within the active ISO envelope.

On 13 August (Fig. 5.7a), the active ISO envelope of convection stretches in a northwest-southeast direction from the northwestern Indian Ocean to the equatorial region to the east of the Maritime Continent. The ISO filtered OLR on 13 August is quite similar to the regressed OLR on day –5 in Fig. 5.3b. A region of 30–96 day filtered 850-hPa westerly perturbations exists in the western Indian Ocean, just to the north of the equator, also as seen in the regressed fields on day –5 in Fig. 5.3b. A large region of deep convection is located over southeastern India, which appears to have developed in situ and does not represent a westward-propagating mode. In the western Pacific, two tropical cyclones, Betty and Cary, have formed on the northern edge of the ISO envelope. Betty is located within a well-developed, large-scale 850-hPa cyclonic circulation, while Cary is located on the northwestern side of an 850-hPa anticyclone (not shown). Five days later, on 18 August (Fig. 5.7b), the remnants of Supertyphoon (ST) Betty have crossed southeast Asia, remaining coherent as the convection and circulation propagate westward. Typhoon (TY) Cary continues to strengthen in the western Pacific. The OLR and <10 day filtered 850-hPa circulation anomalies associated with these disturbances on 18 August are shown in Fig. 5.8. A wavetrain of cyclonic and anticyclonic vortices arcs southeastward from ex-ST Betty, through TY Cary, toward the equator, in a similar manner to the MRG/TD regressed fields in Fig. 5.2b. The scale of the circulation

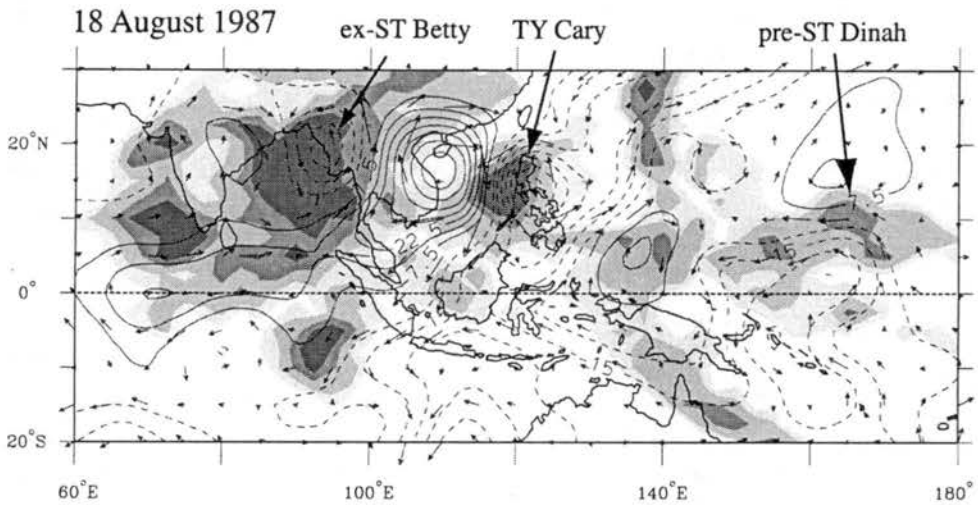


Figure 5.8: Total OLR (shading as in Fig. 7) and <10 day filtered 850-hPa winds (streamfunction contours, interval is 7.5 x 10^5 m^2 s^{-1}; longest wind vectors are 10 m s^{-1}) for 18 August 1987.

anomalies increases toward the east, and the circulations become more equatorially centered, suggesting that Betty and Cary may have formed in association with an MRG-to-TD-type transition. In addition, the region of low OLR at 10°N, 165°E in Fig. 5.8, located in the southeasterly flow of the MRG-like disturbance centered at 160°E, eventually develops into ST Dinah as it propagates northwestward. A similar evolution of MRG waves to TD disturbances during early July 1987 is illustrated by Dickinson and Molinari (2002).

Once ex-ST Betty reaches the southeast Asian landmass, it accelerates westward and projects onto the MRG/TD OLR band, as seen in Fig. 5.6 by the westward-propagating features enclosed by the MRG/TD filtered OLR contours. A similar evolution is observed for Typhoon (TY) Cary. On 23 August (Fig. 5.7c), TY Cary is still analyzed as a tropical cyclone, even though it is located over land, due to its coherence as a tropical storm-like structure. Saha et al. (1981) document numerous instances of

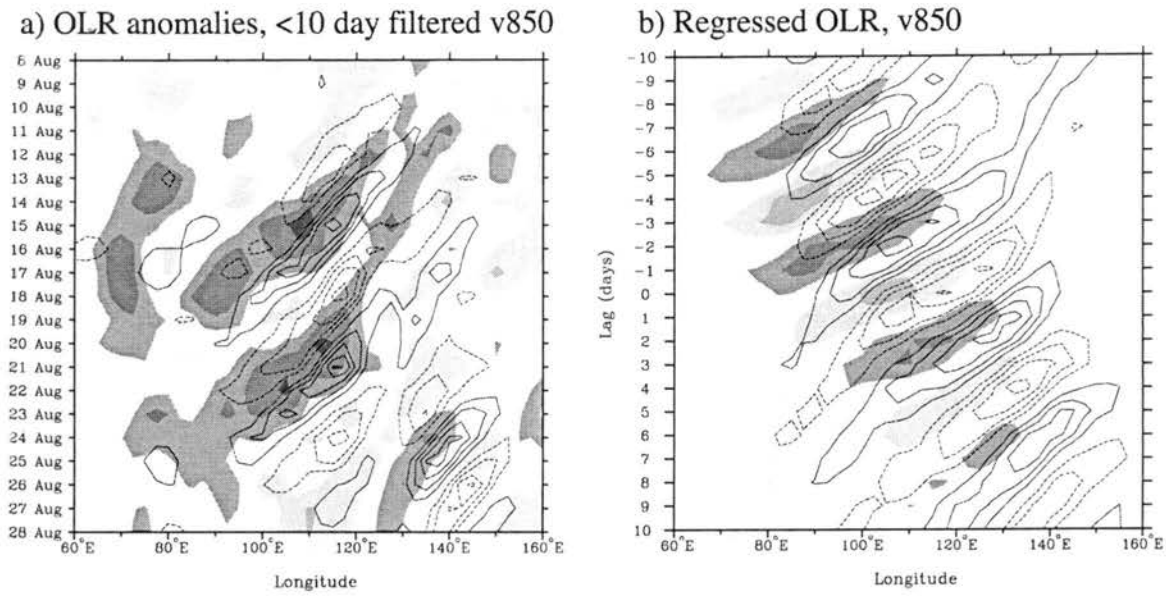


Figure 5.9: Time–longitude diagram of (a) OLR anomalies (shading, at ±20, 45, and 70 W m^{-2}) and <10 day filtered 850-hPa meridional wind (contours, by 2 m s^{-1}, solid positive, zero contour omitted), for 8–28 August 1987, and (b) regressed OLR (shading, by 5 W m^{-2}) and 850-hPa meridional wind (contours, by 0.25 m s^{-1}) from day –10 to day +10, based on a +20 W m^{-2} anomaly in MRG/TD filtered OLR at 10°N, 95°E on day 0. All fields are averaged from 5°–20°N.

western Pacific tropical cyclones propagating westward across southeast Asia, many regenerating into monsoon depressions in the Bay of Bengal.

The relationship between convection and the lower tropospheric circulation during the development and propagation of Betty, Cary, and Dinah is shown in Fig. 5.9a, which illustrates the evolution of the OLR anomaly field (shading, total OLR minus the mean and first three annual harmonics) and the <10 day filtered 850-hPa meridional wind (contours), averaged from 5°–20°N, from 8–28 August. Individual convective disturbances propagate westward, and are flanked by northerly (southerly) anomalies to their west (east), representing the wavetrain of lower tropospheric cyclonic and anticyclonic circulations that propagate westward with the OLR. An eastward dispersion

of energy can be seen in the wind field, which may account for the continued development of subsequent tropical cyclones to the east of their previous locations.

For comparison purposes, Fig. 5.9b shows the regressed OLR (shading) and 850-hPa meridional wind (contours) associated with a +20 W m^{-2} perturbation in the MRG/TD filtered OLR at the basepoint 10°N, 95°E, also averaged from 5°–20°N. In a similar manner to the case study data in Fig. 5.9a, the regressed OLR and meridional wind fields are in quadrature, with northerlies (southerlies) to the west (east) of the negative OLR anomalies. A similar eastward dispersion of energy is seen. The strong resemblance between the case study fields in Fig. 5.9a and the regressed fields in Fig. 5.9b suggests that the evolution of these westward-propagating modes may be predictable, and validates the use of the filtered fields in the statistical analysis in Section 5.3.

Returning to Fig. 5.7, the 30–96 day filtered 850-hPa westerlies accelerate throughout the period shown in Fig. 5.9, as the tropical storms and MRG/TD disturbances propagate westward. On 23 August (Fig. 5.7c), westerly anomalies extend to 120°E, and begin to develop near 140°E. Two more tropical cyclones, Dinah and Ed, have formed in the ISO active convective envelope by this time, to the south of a region of low-frequency easterlies along 10°–20°N. The convection and circulation anomalies on 23 August are quite similar to the regressed fields on day +5 in Fig. 5.3c. It is not surprising that tropical cyclones continue to develop in the large region of enhanced cyclonic zonal wind shear along 10°N in the western Pacific: climatologically, 42% of tropical disturbances in the western Pacific form in this type of monsoon shear line environment (Ritchie and Holland 1999). On 28 August (Fig. 5.7d), Dinah and Ed are still visible in

the northern edge of the active ISO envelope, and westerly anomalies extend into the western Pacific.

By 2 September (Fig. 5.7e), anomalous westerlies extend nearly to the Dateline (compare with the regressed fields on day −15 in Fig. 5.3d), and the low-frequency ISO OLR signal consists of 3 developing tropical storms: Freda, Gerald, and Holly, which again line up roughly along the shear line in the monsoon trough. On 7 September (Fig. 5.7f), these three tropical storms extend across the western Pacific from 120°E to 170°E, and are flanked to their south by strong westerly anomalies. The development of these storms does not appear to correspond to a continued eastward dispersion of disturbance energy; instead, these storms all form at approximately the same time in a manner consistent with the breakdown of a monsoon trough via barotropic instability (Ferreira and Schubert 1997).

The spatial and temporal development of multiple tropical cyclones and MRG/TD disturbances in the context of the low-frequency ISO convection and westerly wind anomalies during this case study is intriguing. The evolution of these fields suggests the possibility of a complex interaction between the development of high-frequency tropical disturbances, their net effect on the low-frequency convection and circulation, and the resulting effects of the low-frequency circulation back onto the development of the high-frequency disturbances. If the cyclonic circulation anomalies associated with the tropical cyclones and MRG/TD disturbances are consistently stronger than the anticyclonic anomalies, as might be expected due to the effects of latent heating, a net westerly (easterly) acceleration could be produced to the south (north) of the disturbances. This effect could be responsible for at least a part of the low-frequency westerly acceleration

observed to the south of the convective anomalies in the case study. As mentioned, these westerly anomalies may then provide an environment more conducive to the continued development of tropical storms.

In summary, the low-frequency ISO signal during August–September 1987 consists of seven tropical storms in the western Pacific, two of which continue to propagate westward and project onto MRG/TD disturbances over southeast Asia and India. An eastward dispersion of energy appears to provide the low-level cyclonic circulations necessary for the continued development of several tropical storms. An eastward propagation of low-frequency westerly anomalies may also influence the development of storms along the axis of the monsoon trough. As demonstrated statistically in Section 5.3.2, the low-frequency ISO signal is collocated with an enhancement of activity in the MRG/TD band and strong 850-hPa westerly anomalies.

5.4.2 Eastward-propagating modes

The statistical results presented in Section 5.3.3 suggest that Kelvin wave activity should be enhanced in the Pacific during the active convective phase of the ISO. As shown in Fig. 5.6, two Kelvin wave events propagate eastward across the Pacific at the end of the active ISO phase, during late August and early September 1987. Another Kelvin wave exists just prior to the first strong event in mid-August, but as its convective signal is centered near the equator, it does not appear in Fig. 5.6 due to the effects of averaging over Northern Hemisphere latitudes. No significant eastward-propagating convective events are observed during the suppressed phase of the ISO in July and early August.

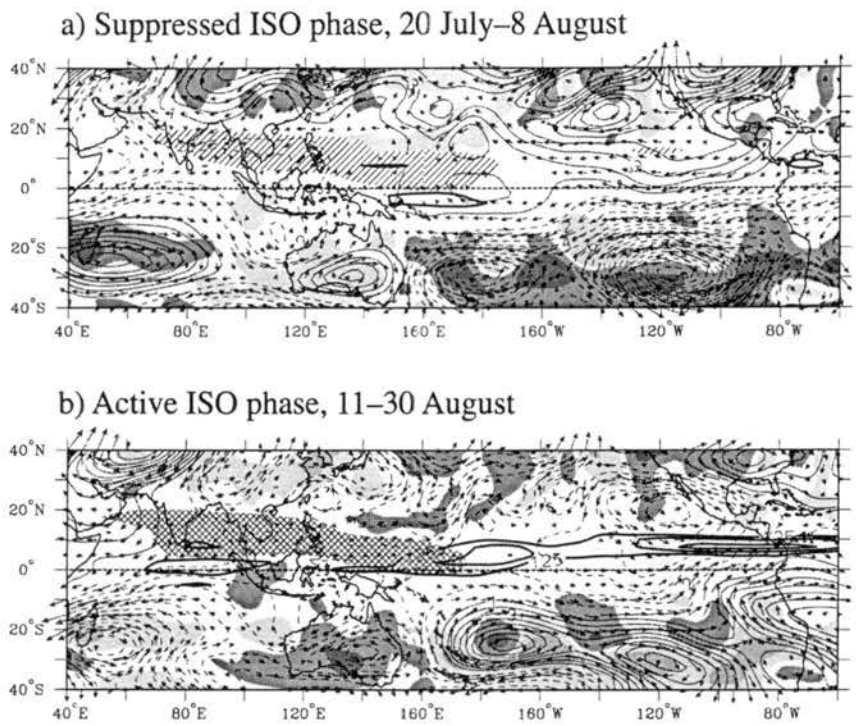


Figure 5.10: Averaged ISO filtered OLR (single hatching positive, cross-hatching negative, at ±10 W m^{-2}), Kelvin wave variance (dark contours, from 125 W m^{-2} by 50 W m^{-2}), 30–96 day filtered 200-hPa winds (streamfunction contours, interval 1.0 x 10^6 m^2 s^{-1}; vector winds, longest vectors are 10 m s^{-1}), and <30 day filtered 200-hPa meridional wind variance anomalies (shading, at ±10 and 50 m^2 s^{-2}) for (a) suppressed ISO, 20 July–8 August 1987, and (b) active ISO, 11–30 August 1987.

Figure 5.10 shows the averaged ISO filtered OLR (hatching), total Kelvin wave variance (dark contours), 30–96 day filtered 200-hPa winds (streamfunction contours and vector winds), and 200-hPa <30 day filtered meridional wind variance anomalies (shading) for the suppressed (Fig. 5.10a) and active (Fig. 5.10b) periods of the ISO during July–August 1987. The suppressed and active periods were each chosen to be 20 days in length, or one-half of the typical 40-day ISO cycle. The date range for each period was determined by matching the daily maps of ISO filtered OLR with the regressed fields in Fig. 5.4, such that the averaged period corresponds with the period between day –10 and day +10 in the regression. The suppressed period extends from 20 July to 8 August, and the active period extends from 11 August to 30 August. The 200-

hPa meridional wind variance anomalies were calculated by subtracting the 20-day average for each period from the 20 July–30 August average. Admittedly, the sample periods are quite short and are somewhat subjectively defined; however, Fig. 5.10 is intended only to illustrate that the statistical relationships presented in Fig. 5.4 hold even in an individual case study.

The suppressed ISO phase in Fig. 5.10a contains very little Kelvin wave variance compared to the active ISO phase in Fig. 5.10b. The 30–96 day filtered 200-hPa wind anomalies are almost exactly opposite in sign between the two periods, with an anomalous anticyclonic (cyclonic) circulation over Australia and an elongated cyclonic (anticyclonic) circulation extending across the Pacific during the active (suppressed) ISO phase. Rossby wave activity over Australia is enhanced (suppressed) during the active (suppressed) ISO period, and activity over the Pacific is located anomalously north (south) of its period mean. These relationships suggest that during the active phase of the ISO, wave activity propagates northeastward over Australia, and then eastward at a more northern latitude than in the suppressed ISO phase, providing the subtropical circulation anomalies shown to be associated with Kelvin wave initiation in SK02a. Specifically, daily maps of OLR and 200-hPa circulation show that on 18 August, a Rossby wavetrain propagates northeastward over Australia and is associated with the initiation of a Kelvin wave event in the central Pacific (not shown; however, the northwest-southeast tilted band of convection associated with the equatorward-propagating wavetrain can be seen to the northeast of Australia in Fig. 5.7b).

The results from the case study during July–September 1987 provide evidence that the statistical results presented in Section 5.3.3 can be seen even in individual events.

Kelvin waves were shown to be more frequent during the active phase of the ISO than during the suppressed phase. This change may have been due to low-frequency fluctuations in the subtropical jet, which change the propagation path of subtropical Rossby wave disturbances, or perhaps to an overall increase in the convective activity in the western Pacific, which would allow Kelvin waves to initiate in that region and subsequently propagate eastward.

5.5 Discussion and conclusions

The statistical results and case study illustrated in this paper suggest a complex relationship between the low-frequency ISO convection and circulation and its associated higher-frequency variability. The statistical results presented in Section 5.3 show that westward-propagating MRG/TD activity is enhanced within the low-frequency ISO convective envelope, while eastward-propagating Kelvin wave (super cluster) activity is enhanced well to the east of the active ISO convection, in the central Pacific. Results from a case study during July–September 1987 are consistent with the statistical results, and portray the ISO convective envelope as including both westward-propagating MRG/TD waves and multiple tropical cyclones in the western Pacific.

The results presented in this study suggest that it may be appropriate to consider the low-frequency ISO convection and circulation fields as "modulating" Kelvin wave activity in the central Pacific, since the convective signals in the two frequency bands do not geographically overlap to a significant degree. This type of one-way interaction would be plausible if Kelvin wave activity could be shown to be affected by low-frequency, ISO-induced changes in the tropical or extratropical circulation, without

comprising a portion of the ISO convective signal itself. Unfortunately, since the ISO is the dominant mode of intraseasonal variability in the tropics, it is difficult to extract a relationship between Kelvin wave variability and low-frequency wind anomalies alone, without including some aspect of ISO convection. The intraseasonal convection, circulation, and higher-frequency wave activity all appear to oscillate together in a coherent pattern.

The geographic separation between the low-frequency ISO signal and that of eastward-propagating Kelvin wave activity is consistent with the studies of Hendon and Liebmann (1994) and Dunkerton and Crum (1995), who show that eastward-propagating convective variability is not necessarily enhanced within or a unique feature of the ISO convective phase. However, our results are contrary to the study of Nakazawa (1988), who suggested that the low-frequency ISO convective signal itself consists largely of eastward-propagating super cluster variability. We do not claim that the ISO is entirely devoid of super cluster activity; rather, that super cluster activity is more strongly enhanced to the east of the ISO convection than within the envelope itself.

Maloney and Hartmann (2000) document an additional "remote" modulation of higher-frequency convective activity by the boreal summer ISO. They show that eastern Pacific tropical cyclones are more likely to form during periods of ISO-related, low-frequency, lower tropospheric westerly anomalies in the eastern Pacific. They argue that ISO convection in the western Pacific induces low-level westerly anomalies that extend across the equatorial Pacific, inducing an anomalous large-scale cyclonic circulation in the northeastern Pacific. This circulation anomaly then provides conditions conducive to tropical cyclone formation in the eastern Pacific. In this case, there is an assumed

independence between the low-frequency circulation fields in the eastern Pacific and the tropical storms themselves, which is most likely justified.

In the case of the interaction between MRG/TD disturbances in the western Pacific and the ISO, on the other hand, the assumption of independence is less justified, such that it might be unwise to think of the low-frequency ISO fields as strictly "modulating" the higher-frequency wave activity. The statistical results shown in Section 5.3.2 show that westward-propagating MRG/TD activity is enhanced within the ISO convective envelope, allowing MRG/TD convection to project onto the lower-frequency signal of the ISO. During August 1987, the ISO convective phase was shown to consist primarily of westward-propagating convective variability, including seven named tropical storms and a MRG/TD wave packet that developed in association with two of these storms. These results suggest that the low-frequency ISO signal may not be independent from its higher-frequency components, such that a separation between the "basic state" and the "anomalies" in the ISO may not necessarily be justified. This idea challenges the results presented in studies such as Liebmann et al. (1994), which suggest that the ISO "modulates" tropical cyclone activity in the western Pacific through low-frequency changes in the lower tropospheric circulation. The results of the present study suggest, instead, that the tropical cyclones and their associated MRG/TD-like disturbances may constitute an integral part of the slowly varying ISO convective field, and may be responsible for at least a portion of the low-frequency circulation changes associated with the ISO. Thus the ISO and higher-frequency disturbances such as tropical cyclones may not be independent, but intricately linked in a two-way interactive system.

6 CONCLUSIONS

The four manuscripts presented in Chapters 2–5 address several fundamental issues related to the observed structure, forcing, and intraseasonal modulation of convectively coupled Kelvin waves. The observations presented in these papers significantly extend the results published in previous studies through an analysis of radiosonde, global reanalysis, and in situ data in the context of both multi-year regressions and individual case studies. Future model simulations of convectively coupled Kelvin waves and their interactions with the large-scale environment will benefit from the detailed observations presented in this study.

The horizontal and vertical structures of convectively coupled Kelvin waves based on ECMWF reanalysis data were shown in Chapters 2 and 4 to be at least qualitatively consistent with the observed structures in both radiosonde data and an individual case study. This similarity suggests that the ECMWF reanalysis captures both the existence of convectively coupled Kelvin waves and the large-scale dynamical effects resulting from their embedded small-scale convective and stratiform precipitation processes. Further study of the reanalysis heating and cloud fields will be necessary to determine whether the dynamical fields are in fact arising in the model from processes similar to those seen in observations.

The in-phase relationship between convection and upper tropospheric warm anomalies in both the ECMWF reanalysis and radiosonde data, as shown in Chapter 4, suggests that strict quasi-equilibrium, as described by Emanuel et al. (1994), does not hold in convectively coupled Kelvin waves. The observed temperature and moisture structures do generally support a quasi-equilibrium balance, in that the observed anomalies are much smaller than might be expected in the absence of convective processes. The observed structure of convectively coupled Kelvin waves appears to combine aspects of several idealized theories, with an important role for stratiform precipitation. Observations suggest the existence of a more vertically complex dynamical structure than has yet been simulated in models.

The temperature structures of convectively coupled Kelvin waves in the NCEP/NCAR reanalysis do not match observations as closely as in the ECMWF reanalysis. For example, as illustrated in Fig. 7 of WKW00, which is derived from NCEP/NCAR reanalysis data, warm anomalies in the upper troposphere precede deep convection in a Kelvin wave by at least a quarter wavelength, in contrast to observations and ECMWF reanalysis data, which show warm anomalies to be collocated with deep convection. Preliminary comparisons between ECMWF and NCEP/NCAR reanalysis data and radiosonde data from multiple sites confirm the superiority of the ECMWF reanalysis fields in simulating the large-scale fields associated with convectively coupled Kelvin waves. A further analysis of the differences in wave structures between these two models is warranted, with the ultimate goal of determining the physical mechanisms involved in generating the model fields. The implications of these findings should also be valuable in evaluating the models' convective parameterization schemes.

The evolution of the extratropical Rossby wave fields associated with the initiation of a convectively coupled Kelvin wave are very similar between the ECMWF and NCEP/NCAR reanalyses, providing support for this mechanism in initiating convection in the tropics. The idea that extratropical vorticity perturbations might theoretically be capable of forcing equatorially trapped waves had been previously discussed by Mak (1969), Zhang (1993), and Hoskins and Yang (2000), but observations of such interactions were scarce. The results presented in Chapter 3 represent the first observations demonstrating the direct forcing of convectively coupled Kelvin waves from the extratropics. These observations are particularly significant since they demonstrate that extratropical-to-tropical forcing can occur even in regions of tropical easterlies.

The extratropical forcing mechanism proposed in Chapter 3 is consistent with the observed modulation of convectively coupled Kelvin wave activity by the boreal summer ISO, as discussed in Chapter 5. Low-frequency changes in the austral winter subtropical jet forced by the slowly-varying ISO convective fields cause changes in subtropical wave activity, which influence Kelvin wave activity through the associated changes in extratropical forcing of these waves.

The results presented in this study open up numerous opportunities for additional analysis of convectively coupled equatorial waves. Similar observational studies to these Kelvin wave analyses could be completed for other types of convectively coupled waves, such as mixed Rossby-gravity waves, n = 1 equatorial Rossby waves, and inertio-gravity waves, using both case studies and a regression-based approach. A particularly interesting topic might involve observations of mixed Rossby-gravity waves transitioning into tropical depression-type disturbances in the Pacific, as discussed in Chapter 5. In

addition, since the differences in the horizontal and vertical structures of mixed Rossby-gravity waves, tropical-depression-type disturbances, and easterly waves are not yet clearly understood, an observational study comparing these three wave types would also be worthwhile.

Satellite-based radar products from the Tropical Rainfall Measuring Mission (TRMM) project have the potential to provide an unprecedented view of the vertical structure of precipitation within convectively coupled equatorial waves. Specifically, the spatial distribution of convective and stratiform precipitation within these waves is of primary interest. These observations could provide additional insight into the accuracy of the convective parameterizations in the ECMWF and NCEP/NCAR reanalysis models, as well as augmenting our understanding of the observed wave structures.

Finally, simple modeling studies could assist in determining whether the observed convectively coupled wave structures are largely a linear response to the observed convective and stratiform heating profiles. A simple model such as described in Haertel and Johnson (2000) could be used to determine the linear response to shallow and deep convective heating profiles as well as second mode stratiform heating over cooling profiles, of the observed spatial scales. Once the response of the atmosphere to these simple heating profiles is understood, the profiles could be superimposed to mimic the observed spatial distribution of heating in Kelvin waves. As discussed in Chapter 2, observed Kelvin waves appear to consist of a shallow heat source to the east of deep heating, and a stratiform heat source to its west. These one-way (heating to dynamical response) simulations would represent a first step in understanding the more complex interactions at work in observed waves.

REFERENCES

Aiyyer, A. R., and J. Molinari, 2002: Evolution of mixed Rossby gravity waves in MJO type environments. *Proceedings of the 25th Conference on Hurricanes and Tropical Meteorology,* American Meteorological Society, 650–651.

Andrews, D. G., J. R. Holton, and C. B. Leovy, 1987: *Middle Atmospheric Dynamics.* International Geophysics Series, Vol. 40, Academic Press, 489 pp.

Arakawa, A., and W. H. Schubert, 1974: Interaction of a cumulus cloud ensemble with the large-scale environment, Part I. *J. Atmos. Sci.,* **31**, 674–701.

Chang, C.-P., and H. Lim, 1988: Kelvin wave-CISK: A possible mechanism for the 30–50 day oscillations. *J. Atmos. Sci.,* **45**, 1709–1720.

Chang, E. K. M., 1999: Characteristics of wave packets in the upper troposphere. Part II: Seasonal and hemispheric variations. *J. Atmos. Sci.,* **56**, 1729–1747.

Chao, W. C., 1995: A critique of wave-CISK as an explanation for the 40–50 day tropical intraseasonal oscillation. *J. Meteor. Soc. Japan,* **73**, 677–684.

Charney, J. G., 1969: A note on large-scale motions in the Tropics. *J. Atmos. Sci.,* **20**, 607–609.

Chu, P.-S., 1988: Extratropical forcing and the burst of equatorial westerlies in the western Pacific: A synoptic study. *J. Meteor. Soc. Japan,* **66**, 549–564.

Compo, G. P., G. N. Kiladis, and P. J. Webster, 1999: The horizontal and vertical structure of east Asian winter monsoon pressure surges. *Q. J. R. Meteorol. Soc.,* **125**, 29–54.

Crum, F. X., and T. J. Dunkerton, 1992: Analytic and numerical models of wave-CISK with conditional heating. *J. Atmos. Sci.,* **49**, 1693–1708.

Dickinson, M., and J. Molinari, 2002: Mixed Rossby-gravity waves and western Pacific tropical cyclogenesis. Part I: Synoptic evolution. *J. Atmos. Sci.* (in press).

Dunkerton, T. J., 1993: Observation of 3–6 day meridional wind oscillations over the tropical Pacific, 1973–1992: Vertical structure and interannual variability. *J. Atmos. Sci.,* **50**, 3292–3307.

Dunkerton, T. J., and M. P. Baldwin, 1995: Observation of 3–6-day meridional wind oscillations over the tropical Pacific, 1973–1992: Horizontal structure and propagation. *J. Atmos. Sci.,* **52**, 1585–1601.

Dunkerton, T. J., and F. X. Crum, 1995: Eastward propagating ~2- to 15-day equatorial convection and its relation to the tropical intraseasonal oscillation. *J. Geophys. Res.,* **100**, 25 781–25 790.

Emanuel, K. A., 1987: An air-sea interaction model of intraseasonal oscillations in the tropics. *J. Atmos. Sci.,* **44**, 2324–2340.

Emanuel, K. A., 1994: *Atmospheric Convection.* Oxford University Press, 580 pp.

Emanuel, K. A., J. D. Neelin, and C. S. Bretherton, 1994: On large-scale circulations in convecting atmospheres. *Q. J. R. Meteorol. Soc.,* **120**, 1111–1143.

Ferreira, R. N., and W. H. Schubert, 1997: Barotropic aspects of ITCZ breakdown. *J. Atmos. Sci.,* **54**, 261–285.

Gruber, A., 1974: The wavenumber-frequency spectra of satellite-measured brightness in the tropics. *J. Atmos. Sci.,* **31**, 1675–1680.

Haertel, P. T., and R. H. Johnson, 1998: Two-day disturbances in the equatorial western Pacific. *Quart. J. Roy. Meteor. Soc.,* **124**, 615–636.

Haertel, P. T., and R. H. Johnson, 2000: The linear dynamics of squall line mesohighs and wake lows. *J. Atmos. Sci.,* **57**, 93–107.

Hayashi, Y.-Y., 1970: A theory of large-scale equatorial waves generated by condensation heat and accelerating the zonal wind. *J. Meteor. Soc. Japan,* **48**, 140–160.

Hayashi, Y.-Y., and T. Nakazawa, 1989: Evidence of the eastward motion of superclusters at the equator. *Mon. Wea. Rev.,* **117**, 236–243.

Hendon, H. H., and B. Liebmann, 1991: The structure and annual variation of antisymmetric fluctuations of tropical convection and their association with Rossby-gravity waves. *J. Atmos. Sci.,* **48**, 2127–2140.

Hendon, H. H., and B. Liebmann, 1994: Organization of convection within the Madden-Julian Oscillation. *J. Geophys. Res.*, **99**, 8073–8083.

Holton, J. R., 1972: Waves in the equatorial stratosphere generated by tropospheric heat sources. *J. Atmos. Sci.*, **29**, 368–375.

Hoskins, B. J., I. N. James, and G. H. White, 1983: The shape, propagation and mean-flow interaction of large-scale weather systems. *J. Atmos. Sci.*, **40**, 1595–1612.

Hoskins, B. J., and G.-Y. Yang, 2000: The equatorial response to higher-latitude forcing. *J. Atmos. Sci.*, **57**, 1197–1213.

Houze, R. A. Jr., 1993: *Cloud Dynamics.* Academic Press, 573 pp.

Houze, R. A., 1997: Stratiform precipitation in regions of convection: A meteorological paradox? *Bull. Amer. Meteor. Soc.*, **78**, 2179–2196.

Hsu, H.-H., B. J. Hoskins, and F.-F. Jin, 1990: The 1985/86 intraseasonal oscillation and the role of the extratropics. *J. Atmos. Sci.*, **47**, 823–839.

Kemball-Cook, S., and B. Wang, 2001: Equatorial waves and air-sea interaction in the boreal summer intraseasonal oscillation. *J. Climate,* **14**, 2923–2942.

Kessler, W. S., and M. J. McPhaden, 1995: Oceanic equatorial waves and the 1991–93 El Nino. *J. Climate,* **8**, 1757–1774.

Kiladis, G. N., 1998: Observations of Rossby waves linked to convection over the eastern tropical Pacific. *J. Atmos. Sci.*, **55**, 321–339.

Kiladis, G. N., and K. M. Weickmann, 1992a: Circulation anomalies associated with tropical convection during northern winter. *Mon. Wea. Rev.*, **120**, 1900–1923.

Kiladis, G. N., and K. M. Weickmann, 1992b: Extratropical forcing of tropical Pacific convection during northern winter. *Mon. Wea. Rev.*, **120**, 1924–1938.

Kiladis, G. N., and K. M. Weickmann, 1997: Horizontal structure and seasonality of large-scale circulations associated with submonthly tropical convection. *Mon. Wea. Rev.*, **125**, 1997–2013.

Kiladis, G. N., and M. Wheeler, 1995: Horizontal and vertical structure of observed tropospheric equatorial Rossby waves. *J. Geophys. Res.*, **100**, 22 981–22 997.

Knutson, T. R., and K. M. Weickmann, 1987: 30–60 day atmospheric oscillations: Composite life cycles of convection and circulation anomalies. *Mon. Wea. Rev.*, **115**, 1407–1436.

Knutson, T. R., K. M. Weickmann, and J. E. Kutzbach, 1986: Global-scale intraseasonal oscillations of outgoing longwave radiation and 250 mb zonal wind during Northern Hemisphere summer. *Mon. Wea. Rev.*, **114**, 605–623.

Krishnamurti, T. N., H. S. Bedi, and M. Subramaniam, 1989: The summer monsoon of 1987. *J. Climate*, **2**, 321–340.

Krishnamurti, T. N., and D. Subrahmanyam, 1982: The 30–50 day mode at 850 mb during MONEX. *J. Atmos. Sci.*, **39**, 2088–2095.

Lamb, V. R., 1973: The response of the tropical atmosphere to middle latitude forcing. Ph.D. thesis, University of California, Los Angeles, 151 pp.

Lau, K.-H., and N.-C. Lau, 1992: The energetics and propagation dynamics of tropical summertime synoptic-scale disturbances. *Mon. Wea. Rev.*, **120**, 2523–2539.

Lau, K.-M., 1982: Equatorial response to northeasterly cold surges as inferred from satellite cloud imagery. *Mon. Wea. Rev.*, **110**, 1306–1313.

Lau, K.-M., and P. H Chan, 1986: Aspects of the 40–50 day oscillation during the northern summer as inferred from outgoing longwave radiation. *Mon. Wea. Rev.*, **114**, 1354–1367.

Lau, K.-M, and L. Peng, 1987: Origin of low-frequency (intraseasonal) oscillations in the tropical atmosphere. Part I: Basic theory. *J. Atmos. Sci.*, **44**, 950–972.

Lau, K.-M., T. Nakazawa, and C. H. Sui, 1991: Observations of cloud cluster hierarchies over the tropical western Pacific. *J. Geophys. Res.*, **96**, 3197–3208.

Lawrence, D. M., and P. J. Webster, 2002: The boreal summer intraseasonal oscillation: Relationship between northward and eastward movement of convection. Accepted to *J. Atmos. Sci.*

Liebmann, B., and D. L. Hartmann, 1984: An observational study of tropical-midlatitude interaction on intraseasonal time scales during winter. *J. Atmos. Sci.*, **41**, 3333–3350.

Liebmann, B., and H. H. Hendon, 1990: Synoptic-scale disturbances near the equator. *J. Atmos. Sci.,* **47**, 1463–1479.

Liebmann, B., H. H. Hendon, and J. D. Glick, 1994: The relationship between tropical cyclones of the western Pacific and Indian Oceans and the Madden-Julian Oscillation. *J. Meteor. Soc. Japan,* **72**, 401–411.

Liebmann, B., G. N. Kiladis, J. A. Marengo, T. Ambrizzi, and J. D. Glick, 1999: Submonthly convective variability over South America and the South Atlantic Convergence Zone. *J. Climate,* **12**, 1877–1891.

Liebmann, B., and C. A. Smith, 1996: Description of a complete (interpolated) outgoing longwave radiation dataset. *Bull Amer. Meteor. Soc.,* **77**, 1275–1277.

Lim, H., and C.-P. Chang, 1981: A theory for midlatitude forcing of tropical motions during winter monsoons. *J. Atmos. Sci.,* **38**, 2377–2392.

Lim, H., T.-K. Lim, and C.-P. Chang, 1990: Reexamination of wave-CISK theory: Existence and properties of nonlinear wave-CISK modes. *J. Atmos. Sci.,* **47**, 3078–3091.

Lin, X., and R. H. Johnson, 1996: Kinematic and thermodynamic characteristics of the flow over the western Pacific warm pool during TOGA COARE. *J. Atmos. Sci.,* **53**, 695–715.

Lindzen, R. S., 1974: Wave-CISK in the tropics. *J. Atmos. Sci.,* **31**, 156–179.

Livezey, R. E., and W. Y. Chen, 1983: Statistical field significance and its determination by Monte Carlo techniques. *Mon. Wea. Rev.*, **111**, 46–59.

Love, G., 1985a: Cross-equatorial influence of winter hemisphere subtropical cold surges. *Mon. Wea. Rev.*, **113**, 1487–1498.

Love, G., 1985b: Cross-equatorial interactions during tropical cyclogenesis. *Mon. Wea. Rev.*, **113**, 1499–1509.

Madden, R. A., and P. R. Julian, 1971: Detection of a 40–50 day tropical oscillation in the zonal wind in the tropical Pacific. *J. Atmos. Sci.*, **28**, 702–708.

Madden, R. A., and P. R. Julian, 1994: Observations of the 40–50-day tropical oscillation—A review. *Mon. Wea. Rev.*, **122**, 814–837.

Magaña, V., and M. Yanai, 1995: Mixed Rossby-gravity waves triggered by lateral forcing. *J. Atmos. Sci.*, **52**, 1473–1486.

Majda, A. J., and M. G. Shefter, 2001: Models for stratiform instability and convectively coupled waves. *J. Atmos. Sci.*, **58**, 1567–1584.

Mak, M.-K., 1969: Laterally driven stochastic motions in the tropics. *J. Atmos. Sci.*, **26**, 41–64.

Maloney, E. D., and D. L. Hartmann, 2000: Modulation of eastern north Pacific hurricanes by the Madden-Julian Oscillation. *J. Climate*, **13**, 1451–1460.

Mapes, B. E., 1993: Gregarious tropical convection. *J. Atmos. Sci.*, **50**, 2026–2037.

Mapes, B. E., 1998: The large-scale part of tropical mesoscale convective system circulations: A linear vertical spectral band model. *J. Meteor. Soc. Japan,* **76**, 29–54.

Mapes, B. E., 2000: Convective inhibition, subgrid-scale triggering energy, and stratiform instability in a toy tropical wave model. *J. Atmos. Sci.,* **57**, 1515–1535.

Mapes, B. E., and R. A. Houze, 1993: Cloud clusters and superclusters over the oceanic warm pool. *Mon. Wea. Rev.,* **121**, 1398–1415.

Matsuno, T., 1966: Quasi-geostrophic motions in the equatorial area. *J. Meteor. Soc. Japan,* **44**, 25–43.

Matthews, A. J., and G. N. Kiladis, 1999: The tropical-extratropical interaction between high-frequency transients and the Madden-Julian Oscillation. *Mon. Wea. Rev.*, **127**, 661–677.

Matthews, A. J., and G. N. Kiladis, 2000: A model of Rossby waves linked to submonthly convection over the eastern tropical Pacific. *J. Atmos. Sci.,* **57**, 3785–3798.

Matthews, A. J., and J. Lander, 1999: Physical and numerical contributions to the structure of Kelvin wave-CISK modes in a spectral transform model. *J. Atmos. Sci.,* **56**, 4050–4058.

Meehl, G. A., G. N. Kiladis, K. M. Weickmann, M. Wheeler, D. S. Gutzler, and G. P. Compo, 1996: Modulation of equatorial subseasonal convective episodes by tropical-extratropical interaction in the Indian and Pacific Ocean regions. *J. Geophys. Res.,* **101**, 15,033–15,049.

Milliff, R. F., and R. A. Madden, 1996: The existence and vertical structure of fast, eastward-moving disturbances in the equatorial troposphere. *J. Atmos. Sci.,* **53**, 586–597.

Nakazawa, T., 1988: Tropical super clusters within intraseasonal variations over the western Pacific. *J. Meteor. Soc. Japan,* **66**, 823–839.

Neelin, J. D., I. M. Held, and K. H. Cook, 1987: Evaporation-wind feedback and low-frequency variablity in the tropical atmosphere. *J. Atmos. Sci.,* **44**, 2341–2348.

Parker, D. J., 2002: The response of CAPE and CIN to tropospheric thermal variations. *Q. J. R. Meteorol. Soc.,* **128**, 119–130.

Reed, R. J., and E. E. Recker, 1971: Structure and properties of synoptic-scale wave disturbances in the equatorial western Pacific. *J. Atmos. Sci.,* **28**, 1117–1133.

Rickenbach, T. M., and S. A. Rutledge, 1998: Convection in TOGA COARE: Horizontal scale, morphology, and rainfall production. *J. Atmos. Sci.,* **55**, 2715–2729.

Ritchie, E. A., and G. J. Holland, 1999: Large-scale patterns associated with tropical cyclogenesis in the western Pacific. *Mon. Wea. Rev.,* **127**, 2027–2043.

Saha, K., F. Sanders, and J. Shukla, 1981: Westward propagating predecessors of monsoon depressions. *Mon. Wea. Rev.*, **109**, 330–343.

Salby, M. L., and R. R. Garcia, 1987: Transient response to localized episodic heating in the tropics. Part I: Excitation and short-time near-field behavior. *J. Atmos. Sci.*, **44**, 458–498.

Serra, Y. L., and R. A. Houze Jr., 2002: Observations of variability on synoptic time scales in the east Pacific ITCZ. *J. Atmos. Sci.*, **59**, 1723–1743.

Sikdar, D. N., J. A. Young, and V. E. Suomi, 1972: Time-spectral characteristics of large-scale cloud systems in the tropical Pacific. *J. Atmos. Sci.*, **29**, 229–239.

Sobel, A. H., and C. S. Bretherton, 1999: Development of synoptic-scale disturbances over the summertime tropical northwest Pacific. *J. Atmos. Sci.*, **56**, 3106–3127.

Steiner, M., R. A. Houze Jr., and S. E. Yuter, 1995: Climatological characterization of three-dimensional storm structure from operational radar and rain gauge data. *J. Appl. Meteor.*, **34**, 1978–2007.

Stevens, B., D. A. Randall, X. Lin, and M. T. Montgomery, 1997: Comments on 'On large-scale circulations in convecting atmospheres' by Kerry A. Emanuel, J. David Neelin and Christopher S. Bretherton. *Q. J. R. Meteorol. Soc.*, **123**, 1771–1778.

Straub, K. H., and G. N. Kiladis, 2002a: Extratropical forcing of convectively coupled Kelvin waves during austral winter. Submitted to *J. Atmos. Sci.*, March 2002.

Straub, K. H., and G. N. Kiladis, 2002b: Observations of a convectively coupled Kelvin wave in the eastern Pacific ITCZ. *J. Atmos. Sci.,* **59**, 30–53.

Takayabu, Y. N., 1994: Large-scale cloud disturbances associated with equatorial waves. Part I: Spectral features of the cloud disturbances. *J. Meteor. Soc. Japan,* **72**, 433–448.

Takayabu, Y. N., K.-M. Lau, and C.-H. Sui, 1996: Observation of a quasi-2-day wave during TOGA COARE. *Mon. Wea. Rev.,* **124**, 1892–1913.

Takayabu, Y. N., and M. Murakami, 1991: The structure of super cloud clusters observed in 1–20 June 1986 and their relationship to easterly waves. *J. Meteor. Soc. Japan,* **69**, 105–125.

Takayabu, Y. N., and T. Nitta, 1993: 3–5 day-period disturbances coupled with convection over the tropical Pacific Ocean. *J. Meteor. Soc. Japan,* **71**, 221–246.

Thorncroft, C. D., B. J. Hoskins, and M. E. McIntyre, 1993: Two paradigms of baroclinic-wave life-cycle behaviour. *Quart. J. Roy. Meteor. Soc.,* **119**, 17–55.

Trenberth, K. E., 1997: The definition of El Niño. *Bull. Amer. Meteor. Soc.,* **78**, 2771–2777.

Wang, B., and X. Xie, 1996: Low-frequency equatorial waves in vertically sheared zonal flow. Part I: Stable waves. *J. Atmos. Sci.,* **53**, 449–467.

Webster, P. J., and J. R. Holton, 1982: Cross-equatorial response to middle-latitude forcing in a zonally varying basic state. *J. Atmos. Sci.,* **39**, 722–733.

Wheeler, M., and G. N. Kiladis, 1999: Convectively coupled equatorial waves: Analysis of clouds and temperature in the wavenumber-frequency domain. *J. Atmos. Sci.*, **56**, 374–399.

Wheeler, M., G. N. Kiladis, and P. J. Webster, 2000: Large-scale dynamical fields associated with convectively coupled equatorial waves. *J. Atmos. Sci.*, **57**, 613–640.

Williams, E. R., 1988: The electrification of thunderstorms. *Sci. Amer.*, **269**, 88–99.

Williams, M., 1981: Interhemispheric interaction during Winter MONEX. *Proc. Int. Conf. on Early Results of FGGE and Large-Scale Aspects of Its Monsoon Experiments,* WMO, **10**, 12–16.

Wu, X., and M. A. LeMone, 1999: Fine structure of cloud patterns within the intraseasonal oscillation during TOGA COARE. *Mon. Wea. Rev.*, **127**, 2503–2513.

Yanai, M., B. Chen, and W.-W. Tung, 2000: The Madden-Julian Oscillation observed during the TOGA COARE IOP: Global view. *J. Atmos. Sci.*, **57**, 2374–2396.

Yasunari, T., 1979: Cloudiness fluctuations associated with the Northern Hemisphere summer monsoon. *J. Meteor. Soc. Japan,* **57**, 227–242.

Yasunari, T., 1980: A quasi-stationary appearance of 30 to 40 day period in the cloudiness fluctuations during the summer monsoon over India. *J. Meteor. Soc. Japan,* **58**, 225–229.

Yasunari, T. 1981: Structure of an Indian summer monsoon system with around 40-day period. *J. Meteor. Soc. Japan,* **59**, 336–354.

Young, G. S., D. V. Ledvina, and C. W. Fairall, 1992: Influence of precipitating convection on the surface energy budget observed during a Tropical Ocean Global Atmosphere pilot cruise in the tropical western Pacific Ocean. *J. Geophys. Res.,* **97**, C6, 9595–9603.

Yuter, S. E., and R. A. Houze Jr., 1997: Measurements of raindrop size distributions over the Pacific warm pool and implications for *Z-R* relations. *J. Appl. Meteor.,* **36**, 847–867.

Yuter, S. E., and R. A. Houze Jr., 2000: The 1997 Pan American Climate Studies Tropical Eastern Pacific Process Study. Part I: ITCZ region. *Bull. Amer. Meteor. Soc.,* **81**, 451–482.

Zangvil, A., 1975: Temporal and spatial behavior of large-scale disturbances in tropical cloudiness deduced from satellite brightness data. *Mon. Wea. Rev.,* **103**, 904–920.

Zangvil, A., and M. Yanai, 1980: Upper tropospheric waves in the tropics. Part I: Dynamical analysis in the wavenumber-frequency domain. *J. Atmos. Sci.,* **37**, 283–298.

Zangvil, A., and M. Yanai, 1981: Upper tropospheric waves in the tropics. Part II: Association with clouds in the wavenumber-frequency domain. *J. Atmos. Sci.,* **38**, 939–953.

Zhang, C., 1993: Laterally forced equatorial perturbations in a linear model. Part II: Mobile forcing. *J. Atmos. Sci.*, **50**, 807–821.

Zhang, C., and P. J. Webster, 1989: Effects of zonal flows on equatorially trapped waves. *J. Atmos. Sci.*, **46**, 3632–3652.

Zipser, E. J., 1977: Mesoscale and convective-scale downdrafts as distinct components of squall-line structure. *Mon. Wea. Rev.*, **105**, 1568–1589.

Zipser, E. J., 1994: Deep cumulonimbus cloud systems in the Tropics with and without lightning. *Mon. Wea. Rev.*, **122**, 1837–1851.